ONSET OF TURBULENCE IN PLANE POISEUILLE FLOW

by

CHAITANYA SURYAKANT PARANJAPE

October, 2019

A thesis presented to the
Graduate School
of the
Institute of Science and Technology Austria, Klosterneuburg, Austria
in partial fulfillment of the requirements
for the degree of
Doctor of Philosophy

The thesis of CHAITANYA SURYAKANT PARANJAPE, titled *ONSET OF TURBULENCE IN PLANE POISEUILLE FLOW*, is approved by:

Supervisor: Björn Hof, IST Austria, Klosterneuburg, Austria

Signature: ______________________

Committee Member: Chris Wojtan, IST Austria, Klosterneuburg, Austria

Signature: ______________________

Committee Member: Marc Avila, University of Bremen, Center of Applied Space Technology and Microgravity (ZARM), Bremen 28359, Germany

Signature: ______________________

Defense Chair: Robert Seiringer, IST Austria, Klosterneuburg, Austria

Signature: ______________________

signed page is on file

IST Austria Thesis, ISSN: 2663-337X

I hereby declare that this thesis is my own work and that it does not contain other people's work without this being so stated; this thesis does not contain my previous work without this being stated, and the bibliography contains all the literature that I used in writing the dissertation.

I declare that this is a true copy of my thesis, including any final revisions, as approved by my thesis committee, and that this thesis has not been submitted for a higher degree to any other university or institution.

I certify that any republication of materials presented in this thesis has been approved by the relevant publishers and co-authors.

Signature: ______________________

CHAITANYA SURYAKANT PARANJAPE
October, 2019
signed page is on file

To

Aaji, Aatya and Jui

Abstract

In many shear flows like pipe flow, plane Couette flow, plane Poiseuille flow, etc. turbulence emerges subcritically. Here, when subjected to strong enough perturbations, the flow becomes turbulent in spite of the laminar base flow being linearly stable. The nature of this instability has puzzled the scientific community for decades. At onset, turbulence appears in localized patches and flows are spatio-temporally intermittent. In pipe flow the localized turbulent structures are referred to as puffs and in planar flows like plane Couette and channel flow, patches arise in the form of localized oblique bands. In this thesis, we study the onset of turbulence in channel flow in direct numerical simulations from a dynamical system theory perspective, as well as by performing experiments in a large aspect ratio channel.

The aim of the experimental work is to determine the critical Reynolds number where turbulence first becomes sustained. Recently, the onset of turbulence has been described in analogy to absorbing state phase transition (i.e. directed percolation). In particular, it has been shown that the critical point can be estimated from the competition between spreading and decay processes. Here, by performing experiments, we identify the mechanisms underlying turbulence proliferation in channel flow and find the critical Reynolds number, above which turbulence becomes sustained. Above the critical point, the continuous growth at the tip of the stripes outweighs the stochastic shedding of turbulent patches at the tail and the stripes expand. For growing stripes, the probability to decay decreases while the probability of stripe splitting increases. Consequently, and unlike for the puffs in pipe flow, neither of these two processes is time-independent i.e. memoryless. Coupling between stripe expansion and creation of new stripes via splitting leads to a significantly lower critical point ($Re_c = 670 +/- 10$) than most earlier studies suggest.

While the above approach sheds light on how turbulence first becomes sustained, it provides no insight into the origin of the stripes themselves. In the numerical part of the thesis we investigate how turbulent stripes form from invariant solutions of the Navier-Stokes equations. The origin of these turbulent stripes can be identified by applying concepts from the dynamical system theory. In doing so, we identify the exact coherent structures underlying stripes and their bifurcations and how they give rise to the turbulent attractor in phase space. We first report a family of localized nonlinear traveling wave solutions of the Navier-Stokes equations in channel flow. These solutions show structural similarities with turbulent stripes in experiments like obliqueness, quasi-streamwise streaks and vortices, etc. A parametric study of these traveling wave solution is performed, with parameters like Reynolds number, stripe tilt angle and domain size, including the stability of the solutions. These solutions emerge through saddle-node bifurcations and form a phase space skeleton for the turbulent stripes observed in the experiments. The lower branches of these TW solutions at different tilt angles undergo Hopf bifurcation and new solutions branches of relative periodic orbits emerge. These RPO solutions do not belong to the same family and therefore the routes to chaos for different angles are different.

In shear flows, turbulence at onset is transient in nature. Consequently,turbulence can not be tracked to lower Reynolds numbers, where the dynamics may simplify. Before this happens, turbulence becomes short-lived and laminarizes. In the last part of the thesis, we show that using numerical simulations we can continue turbulent stripes in channel flow past the ’relaminarization barrier’ all the way to their origin. Here, turbulent stripe dynamics simplifies and the fluctuations are no longer stochastic and the stripe settles down to a relative periodic orbit. This relative periodic orbit originates from the aforementioned traveling wave solutions. Starting from the relative periodic orbit, a small increase in speed i.e. Reynolds number gives rise to chaos and the attractor dimension sharply increases in contrast to the classical transition scenario where the instabilities affect the flow globally and give rise to much more gradual route to turbulence.

Acknowledgments

The work presented here could not have been carried out without the support and help of many people. Here, I take an opportunity to express my gratitude towards some of them.

First and foremost, I would like to thank Prof. Björn Hof. I am forever indebted to him for his continuous support during the entire period of my Ph.D. His scientific advice and insightful discussions made this thesis a success. There are many things one can learn from him, which will prove helpful in one's academic career. I think a friendly and harmonious working environment is necessary to work peacefully. Björn is successfully maintaining such a work environment in his group. Apart from the scientific aspects, this is one of the most important qualities of him, which I appreciate. I consider myself lucky to be a part of his research group.

Dr. Yohann Duguet of LIMSI, France, my 'unofficial co-supervisor', deserves a special mention here. The numerical part of this work would not have been successful without his support. I will always cherish the long Skype discussions with him, from which I benefited remarkably. I can not thank Yohann more for being a friend and a mentor.

One of the best things that happened to me during my stay at IST Austria is a wonderful friendship with Dr. Mukund Vasudevan. We worked together as collaborators on the experiments presented here. I will miss the stimulating and funny discussions on a wide range of topics, from science to philosophy and from classical music to literature to politics.

I am grateful to my friend Philipp Maier, a former group technician. Without his invaluable support, the channel experiments would not have been possible.

I thank my collaborator Dr. Nazmi Burak Budanur, and my officemate Dr. Jose Lopez Alonso, for splendid scientific discussions about nonlinear dynamics and numerical techniques. I also thank Dr. Baofang Song for providing the code to simulate channel flow.

I am thankful to the thesis committee members Prof. Chris Wojtan and Prof. Marc Avila for their support and

I would like to thank my other colleagues in the group - Dr. George Choueiri, Michael Riedl, Nishchal Agrawal, Davide Scarselli, Dr. Atul Varshney, Dr. Balachandra Suri, Dr. Lukasz Klotz, Mike Hennessey-Wesen - for their support and friendship. They made this entire period far more enjoyable than it would have been otherwise.

Roshan, Keerthi, Madhu, Aniket, Anushree, Sanju - you were always there for me. Our friendship is one of the best byproducts of my Ph.D.

My family is the most crucial supporting pillar of my life. I can not thank enough my parents Uttara and Suryakant Paranjape for there constant support and unconditional love. I am short of words when it comes to express my feelings towards them. But I am sure that they will understand what I want to say even when I don't say a word. They mastered this art many many years ago. My wife, Apurva, was always there with me. She tolerated my erratic timetables, weird working hours, and hardly complained about it. There is so much to learn from her. And one of the things I learned over these years is the meaning of love and patience. My brother Pradyumna deserves a special acknowledgment. I can not thank him officially as our “Bro Code” forbids the formal expression of gratitude towards each other. Though, I will just accept that I owe, to a large extent, my interest in physics to him.

I finally thank my other family members and friends for being a part of my life.

About the Author

Chaitanya S. Paranjape completed his bachelors in Mechanical engineering from University of Pune, India and completed his masters in Mechanical engineering from Indian Institute of Technology Madras, India. He joined IST Austria in September 2013 and after the rotations joined the group of Nonlinear Dynamics and Turbulence headed by Prof. Björn Hof. His research is focused on transition to turbulence in plane Poiseuille flow. He studied the transition phenomenon by performing experiments as well as applying concepts in dynamical systems to the transition problem.

List of Publications

1. C. Paranjape, Y. Duguet, V. Mukund, N.B. Budanur, B. Song and B. Hof, **The deterministic origin of shear flow turbulence**,*In Preparation*
2. C. Paranjape, Y. Duguet and B.Hof, **Solitary stripe solutions of plane channel flow**, *Submitted*
3. V. Mukund, C. Paranjape, P. Sitte, B. Hof **The onset of turbulence in channel flow**, *Under review*

Table of Contents

List of Tables

List of Figures

List of Abbreviations

PPf Plane Poiseuille flow

HPf Hagen-Poiseuille flow (Pipe flow)

PCf Plane Couette flow

TCf Taylor Couette flow

ECS Exact Coherent Structures/solutions

EQ Equilibrium

TW Traveling wave

RPO Relative periodic orbit

PO Periodic orbit

LBTW Lower Branch Traveling wave

UBTW Upper Branch Traveling wave

LBRPO Lower Branch Relative periodic orbit

UBRPO Upper Branch Relative periodic orbit

MFU Minimal Flow Unit

DP Directed percolation

Re Reynolds number

Re_{SN} Reynolds number at the saddle node bifurcation point

Re_H Reynolds number at Hopf bifurcation

1 Transition to turbulence

1.1 Introduction

Most flows occurring in nature and engineering applications are turbulent. A wide range of flows such as geophysical flows like atmospheric flows and ocean currents, river streams, flow around aeroplane wings, and flow inside heat-exchanger components and pipelines exhibit turbulence. Despite the widespread occurrence of turbulence, our understanding of this phenomenon is limited. Unlike laminar flow, where fluid particles move smoothly in an orderly fashion in layers, turbulence is characterized by eddying multi-scale chaotic motion. Even though the differential equations which govern the fluid motion - the Navier-Stokes equations - have been established in the first half of the 19th century, we can not generally predict at what flow rate the laminar motion becomes turbulent. The nonlinear nature of the governing equations makes long term prediction of turbulent flow difficult.

For incompressible flows, the governing equations take the following form.

$$\frac{\partial \boldsymbol{u}}{\partial t} + (\boldsymbol{u} \cdot \nabla)\boldsymbol{u} = -\frac{\nabla p}{\rho} + \nu \nabla^2 \boldsymbol{u} + \boldsymbol{f} \tag{1.1}$$

where, $\boldsymbol{u}(\boldsymbol{x}, t)$ is the velocity as a function of space $\boldsymbol{x}$ and time t. $p(\boldsymbol{x}, t)$ is the pressure, ρ is the density of the fluid and ν is the kinematic viscosity of the fluid. Finally, $\boldsymbol{f}(\boldsymbol{x}, t)$ is an external forcing term. The continuity equation for the incompressible flow is

$$\nabla \cdot \boldsymbol{u} = 0 \tag{1.2}$$

The laminar solutions of these equations can be determined for some simple geometries like pipe flow. However, in experiments at larger speeds, experimental data deviate from the laminar solution. This mismatch was explained by a seminal work by physicist Osborne Reynolds in 1883 [Sengupta and Poinsot, 2010]. He studied the fluid flow through a circular, straight pipe and identified three regimes of the flow. At low flow rates, the fluid motion behaves in an orderly fashion - a laminar regime. At high flow rates, the flow is turbulent exhibiting multi-scale behaviour. The third regime identified is an intermediate regime where the laminar regime coexists with the intermittent turbulent patches. Additionally, he observed that fluid flow is parametrized by a parameter - now known as Reynolds number - which is a combination of flow velocity, the characteristic length-scale of the flow domain, and kinematic viscosity of the fluid [Reynolds, 1883a; Reynolds, 1883b]. The interesting philosophical question is to understand how these distinct regimes can be explained with the same set of governing equations viz. Navier Stokes equations [Eckert, 2007]. Scientists have been approaching this problem in different ways. Some of the approaches have been discussed in the following.

1.1.1 Stability of shear flows

In the first half of the 20th century, many studies were concerned with the stability analysis of the laminar base flows in different flow geometries [Lumley and Yaglom, 2001]. Here, generally, a disturbance is superposed on the laminar base flow, which is a trivial solution of Navier-Stokes equations, and its evolution is studied analytically. Typically for this purpose, the governing equations are linearized, and so the disturbance must be of a small amplitude [Drazin and Reid, 2004]. Eventually, as the disturbance grows, the linear assumption fails, and nonlinear effects start dominating. Therefore, the linear stability analysis only holds for the initial phase where the disturbances are small enough. In the cases where flows become unstable to infinitesimal perturbations, this methodology correctly predicts the transition point and the mode of the instability like in Taylor-Couette flow and Rayleigh-Bénard convection [Schmid and Henningson, 2012].

Concerning channel flow, the linear stability problem for incompressible parallel flows with viscous fluids was formulated by Orr and Sommerfeld in the first decade of the 20th century [Orr, 1907; Sommerfeld, 1908]. Several attempts were made to determine the linear stability limit in Reynolds number Re in PPf [Heisenberg, 1924; Lin, 1945b; Lin, 1945a], where, Re is defined by centerline velocity, half channel gap,

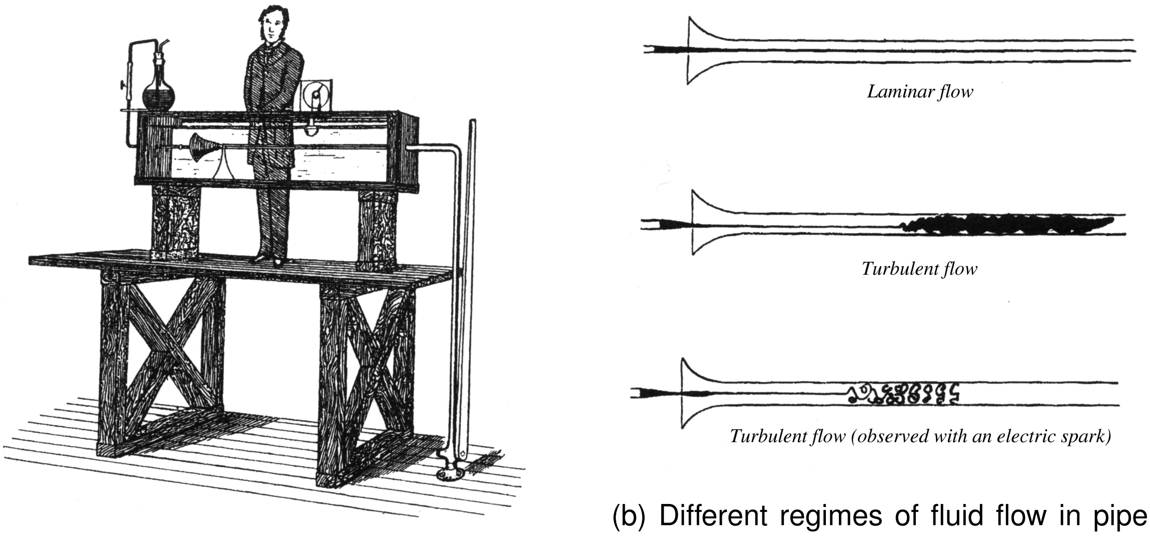

(a) Reynolds's apparatus

(b) Different regimes of fluid flow in pipe, identified by Reynolds

Figure 1.1: Pipe experiments by Reynolds

and kinematic viscosity. However, the accurate estimation of the critical Re for linear stability was finally determined numerically by Orszag [Orszag, 1971]. The linear stability limit for the PPf is found to be $Re = 5772.22$. Below this Re, if the laminar base flow is subjected to infinitesimally small perturbations, the perturbations decay, and the flow remains laminar.

However, turbulence in channel flow typically sets in well below this critical point where the flow becomes linearly unstable and, therefore, linear stability analysis fails to predict a value of Re at which turbulence first occurs in channel. Additionally, the structures observed at the onset of this subcritical transition do not agree with the unstable modes predicted by the linear stability analysis. Pipe flow is even believed to be linearly stable for all Re [Meseguer and Trefethen, 2003]. Nevertheless turbulence already occurs in the form of localized patches called puffs at Re 1800 and becomes sustained for $Re > 2040$ [Avila *et al.*, 2011] and then in the form of slug at higher $Re \approx 2100$ [Wygnanski and Champagne, 1973; Barkley *et al.*, 2015]. Similarly for plane Couette flow (PCf), the base laminar profile is linearly stable for all Re [Drazin and Reid, 2004], but the turbulence becomes sustained at $Re > 325$ [Dauchot and Daviaud, 1995; Bottin *et al.*, 1998a]. In the case of PPf, the early experiments in channel flow showed the occurrence of turbulence at Re 1000, which is much smaller than the linear stability limit [Davies *et al.*, 1928; Narayanan and Narayana, 1967; Patel

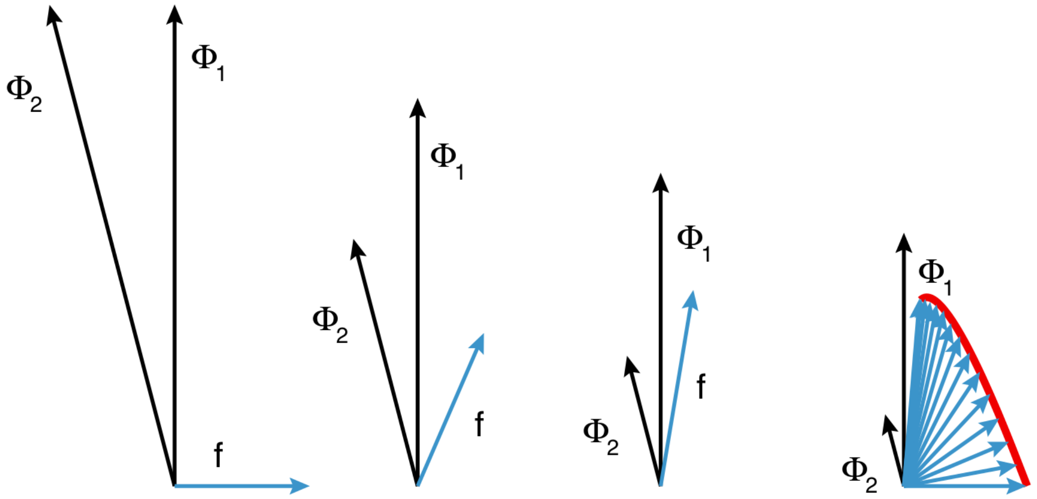

Figure 1.2: ϕ_1 and ϕ_2 are the monotonically decaying nonnormal eigenvector, and f is the resultant. The figure demonstrates how the resultant vector grows transiently before an ultimate decay due to the non-normality of the eigenfunctions. (Figure credit: Schmid Ann.Rev.Fluid. 2007 [Schmid, 2007])

and Head, 1969; Carlson *et al.*, 1982; Nishioka and Asai, 1985; Alavyoon *et al.*, 1986].

Linear stability theory only provides limited insight into the existence of sustained turbulence even when the base laminar flow is linearly stable, i.e., when all the eigenmodes are stable. In other words, the mechanism for the growth of a finite disturbance is different from the unstable eigenmode of the base laminar flow. However, as will be discussed later, linear stability analysis can also be used to determine the stability of non-trivial i.e., non-laminar invariant solutions of the Navier-Stokes equations.

1.1.2 Nonmodal stability analysis

In the last 30 years, the nonmodal analysis has attracted the attention of the fluid dynamics community. Traditional linear stability analysis looks at the evolution of disturbances as $t \to \infty$, whereas the nonmodal stability analysis looks into the evolution of the disturbances in a finite time window [Schmid, 2007].

The operator of the Orr-Sommerfeld equations has non-normal eigenfunctions [Trefethen *et al.*, 1993; Grossmann, 2000]. Because of this nonnormality, the perturbations on the base flow transiently grow in energy, before finally decaying at $t \to \infty$ [Trefethen *et al.*, 1993]. This concept has been illustrated in Figure 1.2 from a review by Schmid

[Schmid, 2007]. Here, ϕ_1 and ϕ_2 are two non-normal eigenvectors and f is their resultant. Both the eigenvectors monotonically diminish in magnitude. However, because of the non-normality between ϕ_1 and ϕ_2, the resultant f grows transiently before decaying eventually at $t \to \infty$. This temporary growth is called transient growth or algebraic growth. Figure 1.3 shows energy growth curves in plane Poiseuille flow at different Re based on the computation of transient growth in PPf by Reddy and Henningson [Reddy and Henningson, 1993]. To further illustrate the difference between the linear stability and the transient growth, let us consider the transient growth in channel flow in the linearly stable ($Re < 5772$) and in the linearly unstable ($Re > 5772$) regime. Interestingly, as shown in Figure 1.3, for a small value of t, i.e., in the transient regime, the disturbance grows transiently in a similar fashion in the linearly stable and linearly unstable regime and is independent of the stability properties of the laminar base flow. However, the stability properties are revealed only at larger values of t, where, for the linearly stable case, the perturbations decay as $t \to \infty$, and for the linearly unstable case, the energy grows infinitely with $t \to \infty$.

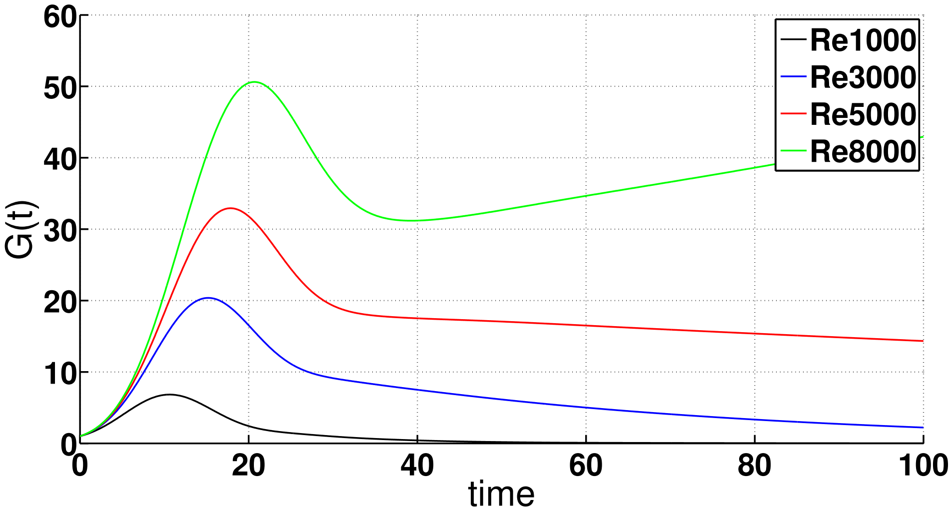

Figure 1.3: Transient growth of small perturbations in plane Poiseuille flow at different Re. For each Re, the curves are normalized with the energy of the initial perturbations. A small perturbation over the base flow grows algebraically before exponentially decaying for linearly stable base laminar flow regime at $Re < 5772$. For linearly unstable regime the energy keeps growing as $t \to \infty$

In a nutshell, the nonmodal analysis shows that the energy of the perturbations grow transiently even when the base flow is linearly stable. However, it can not explain the nonlinear evolution of the perturbations, which makes the flow turbulent. After the initial growth, the perturbation levels always go to zero if the flow is linearly stable. In reality, however, the nonlinear effects become prominent if the amplitudes are sufficiently large.

1.1.3 Dynamical system theory

In recent years another viewpoint towards the phenomenon of turbulence has become popular. In this approach, the transition to turbulence is studied from the perspective of the dynamical system theory.

The fluid flow is governed by a set of partial differential equations- the Navier-Stokes equations. Expanding the velocity field $\boldsymbol{u}$ as a projection on a complete set of orthonormal function basis transforms these partial differential equations into a set of ordinary differential equations, where the velocity vector $\boldsymbol{u}$ is replaced by a vector of the spectral expansion coefficients $\hat{\boldsymbol{u}}$. The system takes the form of

$$\frac{d\hat{\boldsymbol{u}}}{dt} = f(\hat{\boldsymbol{u}}, P) \tag{1.3}$$

where P is a parameter.

Here, turbulence is viewed as a trajectory traveling in an infinite-dimensional state-space with the Navier-Stokes equations acting as the evolution equations. This idea dates back to Hopf [Hopf, 1948]. Each point on the trajectory represents a complete 3D velocity field of the entire domain, which fulfills the boundary conditions. Because of the viscous dissipation, microscopic scales can be neglected, and the infinite-dimensional state-space can be approximated with finite but very high dimensional state-space.

Landau suggested that the turbulence is, in some sense, a quasiperiodic motion resulting from an infinite cascade of bifurcating incommensurable frequencies as Re increases [Landau, 1944]. In this picture, each bifurcation adds new temporal frequency and then results in a continuous spectrum of frequencies- which is a signature feature of turbulent flow. Later, Ruelle and Takens [Ruelle and Takens, 1971] showed that very few instabilities are sufficient to generate chaotic dynamics. Experiments in Taylor Couette flow with only the inner cylinder rotating showed the agreement with the picture suggested by Ruelle and Takens [Gollub and Swinney, 1975]. Here, the laminar base flow becomes linearly unstable as Re increases, and flow renders in the form of rolls called Taylor's vortices. These rolls further become unstable and become wavy and then sharply become aperiodic, i.e., the flow becomes chaotic. A similar scenario is observed in Rayleigh-Benard convection [Maurer and Libchaber, 1979].

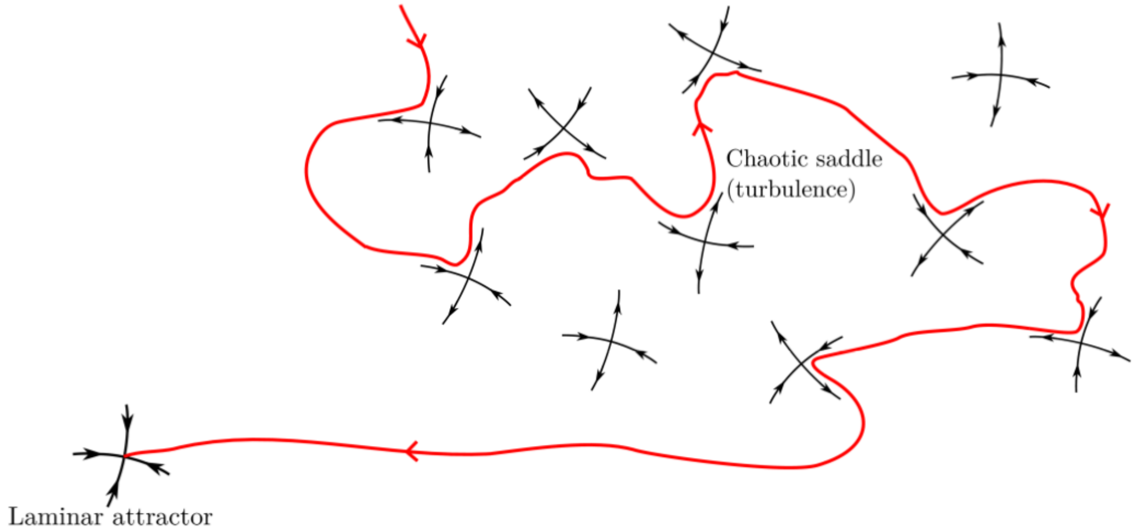

Figure 1.4: Turbulence is thought as a trajectory in the state space traveling through a jungle of invariant solutions guided by the entanglement of their stable and unstable manifolds and homoclinic and heteroclinic connections between these solutions. This schematic representation has been adapted from [Kreilos, 2014]

However, in many linearly stable shear flows like pipe flow and plane Poiseuille flow, turbulence does not arise from the laminar state. Instead, it is believed to originate from unstable invariant solutions of the Navier-Stokes equations, disconnected from the base laminar flow. Also, at the onset, turbulence is in the form of localized patches surrounded by the laminar flow. The situation is more complicated than the flows where the sequence of instabilities start from the base laminar flow itself, as here, the laminar base flow is a global attractor, and turbulence is observed to be transient at onset [Hof *et al.*, 2006] [Bottin *et al.*, 1998b].

The transient nature of turbulence near onset can be though as trajectories in chaotic saddles. These chaotic sets result from the existence of different invariant solutions of the evolution equations (in the case of hydrodynamics- the Navier-Stokes equations) like equilibrium/traveling waves, periodic orbits/relative periodic orbits, tori, etc. and the entanglement of their stable and unstable manifolds. The turbulent trajectories are organized around the agglomeration of these invariant solutions and spend a considerable amount of time in the neighbourhoods of these solutions. The temporal and spatial turbulent dynamics can be described as a weighted sum over the set of these invariant solutions [Cvitanović, 1988]. The transient nature of turbulence near onset suggests that the turbulence structures are not organized around a chaotic attractor but around a chaotic saddle [Eckhardt *et al.*, 2007; Schneider *et al.*, 2010a]. When these trajectories leave the chaotic saddle, they converge to the global attractor - the laminar fixed point - which results in a relaminarization in the physical flow domain (Figure 1.4).

It can be inferred that there exists a boundary in the phase space which separates the chaotic saddle/attractor from the laminar fixed point. The laminar-turbulent boundary separates the initial conditions such that the trajectories starting from the initial conditions on one side of the boundary visit the chaotic saddle/attractor and the trajectories starting from the initial conditions from the other side directly go to the laminar fixed point. This boundary is a hypersurface in the phase space - called the 'edge of chaos' [Itano and Toh, 2001; Skufca *et al.*, 2006] - formed by the stable manifolds of the invariant saddle structures -the 'edge states'. Often, these 'edge states' are equilibrium points (EQ), periodic orbits (PO), traveling waves (TW), relative periodic orbits (RPO), higher dimensional objects like 2-Tori, or even chaotic saddles. It is to be noted that RPOs are POs, and TWs are EQs in the appropriate moving frame of reference. By definition, the edge states are unstable, with only one unstable eigenvalue. The hypersurface, i.e., the edge of chaos, therefore, has codimension 1. The stable manifold of the edge states i.e., the edge of chaos, can have a very complicated geometry, as is evident from the Re vs. amplitude plane in pipe experiments by Darbyshire and Mullin [Darbyshire and Mullin, 1995]. The convoluted nature of the laminar-turbulent boundary can be understood from Re vs amplitude vs lifetimes shown in Figure 1.5 taken from a review paper by Eckhardt et al. [Eckhardt *et al.*, 2007].

With numerical techniques like bisection methods [Skufca *et al.*, 2006], it is possible to follow the edge of chaos for a longer time. The trajectories that lie on the edge of chaos eventually converge to the 'relative attractors' on the edge of chaos or the 'edge states'. The edge states feature structural similarities with the turbulent flows like streamwise streaks and vortices. They are approached by turbulent trajectories

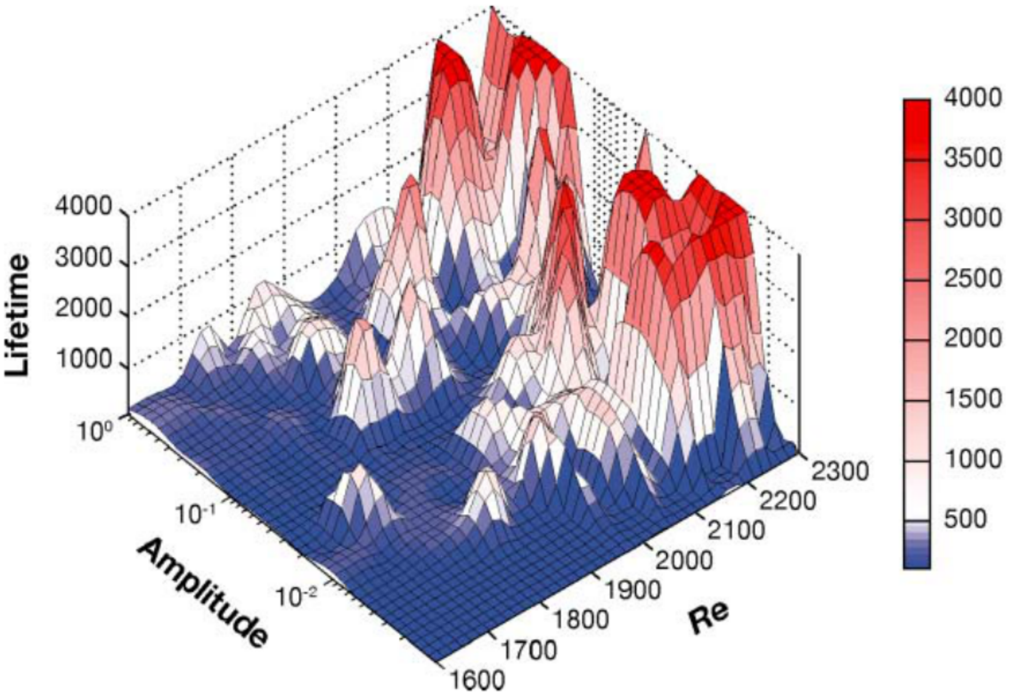

Figure 1.5: Numerical experiments from pipe flow show the amplitude of a fixed initial condition and the corresponding lifetimes of the trajectories at various Re. If the lifetime is higher than certain T_0, then the initial condition is considered lying on the turbulent side of the laminar-turbulent boundary (from [Eckhardt *et al.*, 2007])

transiently. The stable and unstable manifolds of the edge states nudge the turbulent trajectories. The origin of these invariant solutions can be determined by tracing them in the parameter space.

A variety of these invariant solutions or edge states have been computed throughout the last few decades. The first three dimensional invariant solutions of Navier-Stokes equations were found by Nagata in 1990 [Nagata, 1990] in plane Couette flow (PCf), which were the equilibrium solutions. Subsequently, many other equilibria, traveling wave, and periodic/relative periodic orbit solutions were computed in PCf in the doubly periodic domains [Viswanath, 2007; Gibson *et al.*, 2009; Kawahara and Kida, 2001; Kreilos and Eckhardt, 2012]. The heteroclinic connections between the invariant solutions in PCf have been demonstrated [Gibson *et al.*, 2008; Halcrow *et al.*, 2009], which in turn helps in understanding the structure of the chaotic saddle in the phase space. In the pipe flow and plane Poiseuille flow, there are no equilibrium solutions because of non-zero advection in the downstream direction. Traveling wave solutions [Faisst and Eckhardt, 2003; Wedin and Kerswell, 2004] and relative periodic orbits [Duguet *et al.*, 2008] in pipe flow were computed initially in the small periodic domains. Similarly, in the case of plane Poiseuille flow (PPf), traveling wave solutions [Waleffe, 2001; Waleffe, 2003; Nagata and Deguchi, 2013] periodic solutions [Toh and Itano, 2003] and doubly localized relative periodic orbits [Zammert and Eckhardt, 2014b] were computed.

An essential feature of a subcritical shear flow turbulence at onset is the spatio-temporal intermittent nature of turbulence. Here, the localized turbulent patches are surrounded by laminar flow. In pipes, these patches appear in the form of turbulent puffs [Wygnanski and Champagne, 1973], and in PCf and PPf, the turbulence occurs in the form of oblique turbulent bands surrounded by laminar flow [Prigent *et al.*, 2003; Barkley and Tuckerman, 2005; Duguet and Schlatter, 2013; Xiong *et al.*, 2015]. The origins of spatio-temporally intermittent turbulence in the transitional regime can be studied from a dynamical systems perspective by identifying the localized solutions of Navier-Stokes equations in these flow geometries. In PCf, the spanwise localized and the streamwise periodic solutions were computed by [Schneider *et al.*, 2010b; Gibson and Brand, 2014]. Moreover, doubly localized solutions in PCf were also computed by Brand et al. [Brand and Gibson, 2014]. In pipe flow geometry, localized edge states were computed [Willis and Kerswell, 2009; Mellibovsky *et al.*, 2009; Duguet *et al.*, 2010b]. Avila et al. computed the first streamwise localized relative periodic orbit solutions for pipe flow[Avila *et al.*, 2013].

Typically these solutions are unstable with one or more unstable eigenvalues. Here a small perturbation to these solutions will lead to the evolution of trajectories away from the solutions. Being unstable, they can not be directly realized in experiments. These solutions are computed in numerical flow domains using sophisticated techniques. However, there is experimental evidence in pipe flow where the turbulent puffs approach the invariant solutions (traveling waves) intermittently [Hof *et al.*, 2004].

It is observed that these solutions emerge through saddle-node bifurcations and are not connected with the laminar flow. They come in pairs and form two solution branches in the parameter space. The solution branches are named upper branch and lower branch, where, the lower branch, in terms of the energy of perturbations, is in between the upper branch and the laminar fixed point. The lower branch solutions are approximated by edge tracking using bisection methods, which are then further converged using root-finding algorithms such as the Newton method. These solution branches play an important role in understanding the route to chaos. Bifurcation sequences to chaos, starting from invariant solutions have been demonstrated for several flow cases e.g. PCf [Kreilos and Eckhardt, 2012], pipe flow [Avila *et al.*, 2013] and PPf [Zammert and Eckhardt, 2015]. In all these cases, it was observed that the upper branch of the invariant solutions become successively unstable by undergoing a sequence of bifurcations, and eventually, the dynamics become chaotic. All these studies also describe the transition of a chaotic attractor to a chaotic saddle that can occur by the process of boundary crisis or internal crisis. In the boundary crisis, the chaotic attractor collides with an unstable invariant set or a stable manifold of that invariant set, making the chaotic attractor leaky. In the interior crisis, the chaotic attractor becomes non-attracting by colliding with an already coexisting non-attracting chaotic set or its stable manifold [Lai and Tél, 2011].

1.1.4 Turbulence at the onset

As explained earlier, turbulence at onset is composed of localized patches. In a pipe, the puffs first occur at around $Re \sim 2000$ and are advected at velocity about the mean velocity [Wygnanski and Champagne, 1973]. As shown in the subsequent studies, puffs have a finite lifetime, and the probability of the puff surviving for time $> t$ shows exponential distribution, which is a signature of a memoryless process [Peixinho and Mullin, 2006; Hof *et al.*, 2006]. Corresponding lifetimes (i.e. the slopes of the distributions) show superexponential behaviour with Re [Hof *et al.*, 2008].

At slightly larger Re (≈ 2100), puffs are observed to split and grow into more puffs, which results in increased turbulent fraction. This puff splitting is also a memoryless process and the lifetimes of splitting, i.e., the characteristic time for the splitting show a super-exponential decrease with Re [Avila *et al.*, 2011]. Therefore in a very long pipe, if the splitting time is less than the decay time, the turbulence will proliferate and sustain eventually. On the other hand, if the characteristic decay time is less than that of splitting time, turbulence eventually vanishes. Therefore spreading of turbulence is a competition between decay and splitting of the puffs (see Figure 1.6). When the characteristic splitting and decay times are balanced, turbulence becomes sustained in a very long pipe at $Re_c \approx 2040$.

In planar shear flow like PPf and PCf, the turbulence at the onset is in the form of oblique localized bands. In PCf, just like pipe flow, the base laminar flow is linearly stable for all Re. However, the flow becomes turbulent despite that. The critical Re at which turbulence becomes sustained is estimated in experiments by Bottin and Chaté [Bottin and Chaté, 1998]. By examining if the turbulence is sustained beyond a certain large time, the critical value of $Re_c = 323\pm$ is determined. This value of Re_c is also confirmed in simulations in large domains by Duguet et al. [Duguet *et al.*, 2010a].

Similary, in PPf, the laminar base flow is linearly stable until $Re = 5772$ [Ruelle and Takens, 1971]. But the experiments show that the flow becomes turbulent even at $Re = 1000$ [Narayanan and Narayana, 1967; Narayanan, 1968; Narayanan and Ramjee, 1969; Patel and Head, 1969]. The flow visualizations by Carlson et al. showed that turbulence at onset appears in the form of localized spots surrounded by the laminar flow [Carlson *et al.*, 1982; Alavyoon *et al.*, 1986]. These structures were called turbu-

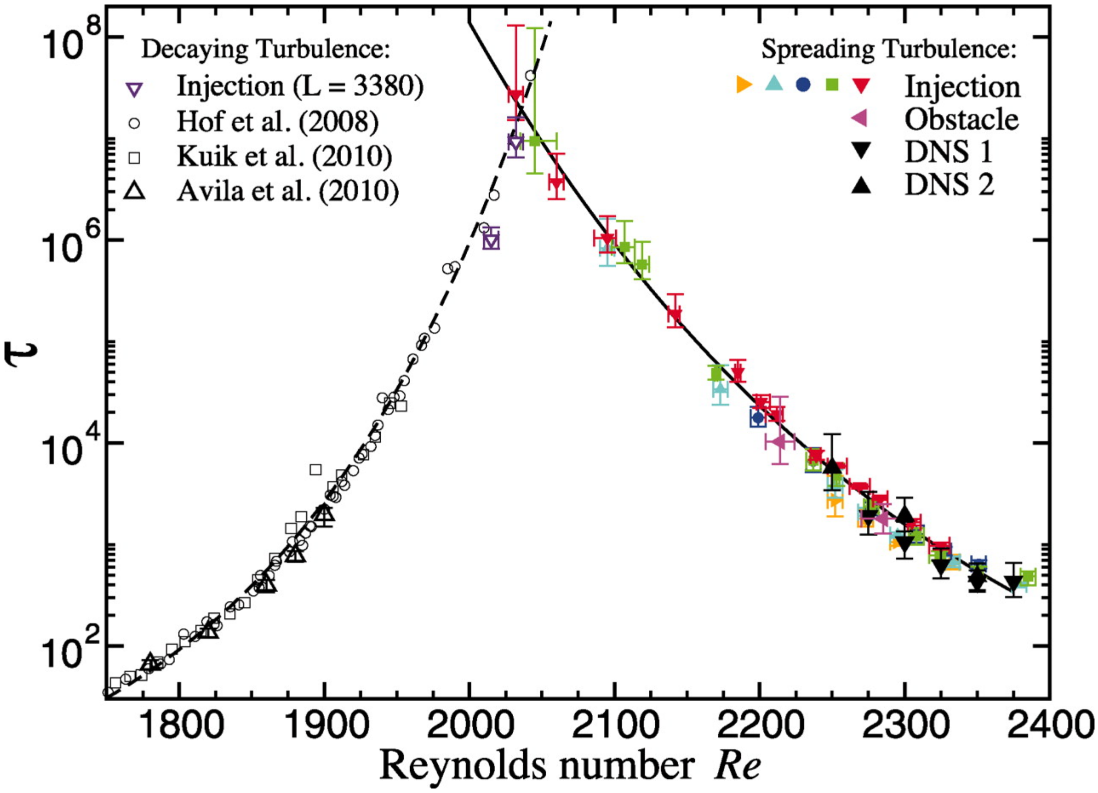

Figure 1.6: The onset of sustained turbulence in pipe flow as a competition between puff decay and puff splitting. The fits are super-exponential fits which intersect at $Re \approx 2040$ which is a critical Re below which the turbulence is not sustained in thermodynamic limit [Avila *et al.*, 2011]

lent spots. However, experiments by Hashimoto et al. [Hashimoto *et al.*, 2009] and numerical simulations by Tsukahara et al. [Tsukahara *et al.*, 2005] show that at these Re, near the onset, turbulence is in the form of extended bands or stripes oblique to the mean flow direction. The recent numerical simulations in relatively extended domains show that these turbulent stripes can exist below $Re\ 700$ [Xiong *et al.*, 2015; Tao *et al.*, 2018]

An important distinction between these turbulent structures in planar flows and in pipe flow is that the puffs in pipe flow do not grow in size as they advect downstream and the proliferation of turbulence is solely due to competition between decay and splitting, whereas in PPf and PCf the turbulent stripes grow in the oblique direction as they move downstream.

1.2 Problems addressed in the thesis

In this study, the focus is mainly on the transition to turbulence in plane Poiseuille flow (PPf), which is also known as channel flow. Compared to many other shear flows like flow around aeroplanes, atmospheric flows, PPf is less complicated, and the analytical solution for the base laminar case is available. Due to its simple geometry, this flow is easier to simulate numerically than many other complicated shear flows. Therefore it is one of the favored candidates for studying the transition to turbulence.

In the present study, the transition in the channel flow is approached from various perspectives.

1. **Experiments** : At the onset, the turbulence is spatio-temporally intermittent and is in the form of oblique stripes surrounded by the base laminar flow. In the experiments, we studied the behaviour of these turbulent structures such as the mean growth rate, the orientation, different regimes of the proliferation of turbulence in channel flow and the relevant mechanisms of the growth of turbulence near onset. The critical Re_c above which turbulence is sustained is also estimated. This Re_c is much lower than the previously reported values.

2. **Dynamical system theory approach** : To understand the dynamical systems framework of turbulence in PPf, various invariant solutions of the PPf are computed. These solutions in the periodic domains with necessary constraints show structural similarities with the turbulent stripes which characterize the onset of turbulence in PPf. To our knowledge, these are the first invariant oblique stripe solutions computed in PPf.

3. **Deterministic origin of turbulent stripes** : The connection between the turbulent stripes and the simple invariant solutions in parameter space is shown. Also the aspects of the origin of the turbulent dynamics starting from these invariant solutions are discussed.

1.3 Organization of the thesis

The thesis is organized in 6 chapter. Following is the description of the material discussed in each of the chapters.

- **Chapter 2** covers the numerical methods and techniques used in this thesis. It summarizes the governing equations, various algorithms used for simulating the flow in plane Poiseuille geometry. It also describes a method to compute the invariant solutions and an algorithm used to converge these invariant solutions and an algorithm to study the stability properties of these solutions.
- **Chapter 3** covers the experimental work carried out in the channel flow. It summarizes the experimental set-up, methodologies, techniques used for analyzing the data and the results from the channel experiments.
- **Chapter 4** includes the computation of the invariant stripe solutions in PPf and their bifurcations. It also covers the bifurcation diagrams for the various parameters like stripe angles, domain size and different routes to chaos.
- **Chapter 5** contains the results regarding the deterministic origin of the turbulent stripes in PPf.
- **Chapter 6** is a summary of the thesis with outlooks.

2 Numerical techniques

In this chapter, the governing equations of plane Poiseuille flow (PPf), a numerical procedure -the tilted domain- employed to simulate the turbulent stripes, the algorithms used for the simulations of PPf and the tools to obtain the non-trivial invariant solutions of the incompressible Navier Stokes equations are discussed.

2.1 Plane Poiseuille flow

Plane Poiseuille flow (PPf)is a pressure-driven shear flow between two infinitely extended parallel plates (figure 2.1). These plates do not have any relative motion between them. The resulting laminar velocity profile is parabolic with its maximum velocity at the center plane of the channel. The parabolic velocity profile when normalized with the centerline velocity U_{cl} and half channel height h. can be written as

$$\begin{aligned} \boldsymbol{U}(y) &= (1-y^2) \\ -1 \leq y &\leq 1 \end{aligned} \tag{2.1}$$

Here y is the wall normal direction.

2.2 Governing equations

In this study, we only consider the incompressible flows of the Newtonian fluids. The fluid motion in PPf is described by the Navier-Stokes equations with the continuity equation. The momentum equations are as follows.

$$\frac{\partial \boldsymbol{u}_{tot}}{\partial t} + (\boldsymbol{u}_{tot} \cdot \nabla)\boldsymbol{u}_{tot} = -\nabla p_{tot} + \frac{1}{Re}\nabla^2 \boldsymbol{u}_{tot} + \boldsymbol{f} \tag{2.2}$$

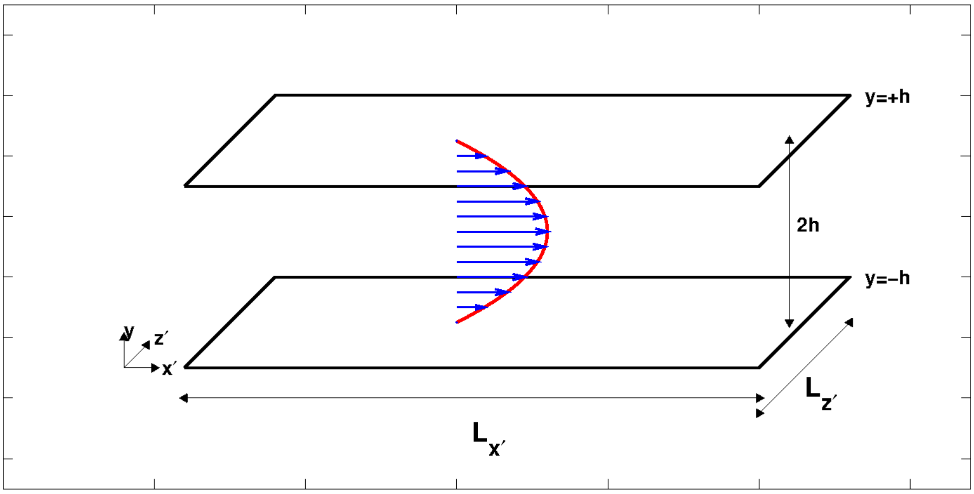

Figure 2.1: Illustration of plane Poiseuille flow. The coordinate system is chosen in such a way that the mean flow or streamwise direction is along direction x', the z' axis represents the spanwise direction and y the wall-normal direction. The flow is induced as a result of the negative pressure gradient from left to right. At the walls, a no-slip boundary condition is imposed. The resulting base laminar velocity profile is parabolic with a maximum velocity at the center-plane $y = 0$.

The continuity equation for incompressible flows is

$$\nabla \cdot \boldsymbol{u}_{tot} = 0 \tag{2.3}$$

Here, $\boldsymbol{u}_{tot}(x', y, z', t) = U_{lam} + \boldsymbol{u}$ is the velocity field, p is the pressure, $\boldsymbol{f}$ is the body force and the Reynolds number Re of a corresponding laminar flow at the same flow rate is defined as $Re = U_{cl}h/\nu$ where U_{cl} is the maximum velocity of the parabolic laminar profile, h is the half gap between the two parallel plates and ν is the kinematic viscosity. No-slip boundary conditions are imposed at the walls.

$$\boldsymbol{u}_{tot}(x', \pm 1, z') = 0 \tag{2.4}$$

where x' is the streamwise direction, z' is the spanwise direction, and y is the wall-normal direction.

In the equations above, velocities are normalized with U_{cl}, lengths with the half channel gap h. Time is normalized by h/U_{cl} and the pressure terms by $\rho {U_{cl}}^2$.

2.3 Tilted domain

The dynamics at the onset of turbulence in PPf is dominated by the localized turbulent stripes oblique to the mean flow direction, which are surrounded by laminar flow. In the numerical simulations, to capture a turbulent stripe, the domain should be large enough in the spanwise and the streamwise direction so that the stripe does not self-interact via the periodic boundary conditions which in turn makes the simulations computationally expensive. This issue is eliminated by tilting the domain with respect to the streamwise direction. This trick was used by Barkley et al. to simulate turbulent bands in PCf [Barkley and Tuckerman, 2005] and also in the simulations of PPf by Tuckermann et al. [Tuckerman *et al.*, 2014].

Figure 2.2a illustrates the concept of the tilted domain. Let x' and z' be the real/physical streamwise and spanwise directions, respectively. We introduce coordinates x and z, which are tilted with respect to x' and z' by an angle θ. The numerical domain is oriented along with the tilted coordinates x and z. For the appropriate angles $(20^\circ < \theta < 70^\circ)$ the stripes will automatically align with the x direction (see Figure 2.2) so that the stripe connects onto itself. In a similar size non-tilted domain, the stripe does not connect to itself but continues via periodic boundary, and the self-interaction causes the stripe to decay.

The unit vectors in the new x and z directions $\hat{\boldsymbol{e}}_x$ and $\hat{\boldsymbol{e}}_z$ respectively have the following relation with the unit vectors in the physical streamwise and the physical spanwise directions $\boldsymbol{e}_{x'}$ and $\boldsymbol{e}_{z'}$ respectively.

$$\hat{\boldsymbol{e}}_{x'} = \cos\theta \hat{\boldsymbol{e}}_x + \sin\theta \hat{\boldsymbol{e}}_z \tag{2.5}$$

$$\hat{\boldsymbol{e}}_{z'} = -\sin\theta \hat{\boldsymbol{e}}_x + \cos\theta \hat{\boldsymbol{e}}_z \tag{2.6}$$

where θ is the tilt angle i.e., the angle between the shorter side of the rectangular box and the physical streamwise direction.

Let $\boldsymbol{U}_b$ represent the bulk velocity in the “physical” streamwise direction x'. The components of the bulk velocity along the new x and z directions of the tilted rectangular box are

$$\boldsymbol{U}_b^x = U_b \cos\theta \tag{2.7}$$

$$\boldsymbol{U}_b^z = U_b \sin\theta \tag{2.8}$$

At the moderate values Re, e.g. $Re = 660$, after starting the simulations from a random initial condition, the dynamics settle to a turbulent stripe localized in the longer direction of the rectangular domain and extended in the shorter direction. In the large aspect ratio experiments and simulations, turbulent stripes are observed in the same Re regime. It features the quasi-streamwise streaks and vortices similar to the turbulent stripe from the experiments or the simulations of non-tilted large domains. Figure 2.2a shows the turbulent stripe in the large domain at $Re = 660$ and Figure 2.2b shows the turbulent stripe at the same Re in the domain tilted at an angle $\theta = 45^\circ$ with respect to the streamwise direction. The turbulent stripe in extended direction attaches itself due to the periodic boundary conditions. This fact forces the turbulent stripe to have the same orientation as the tilted domain with respect to the streamwise direction.

As will be explained in the later chapters, this trick allows us to investigate stripes in a small domain, at a much lower computational cost.

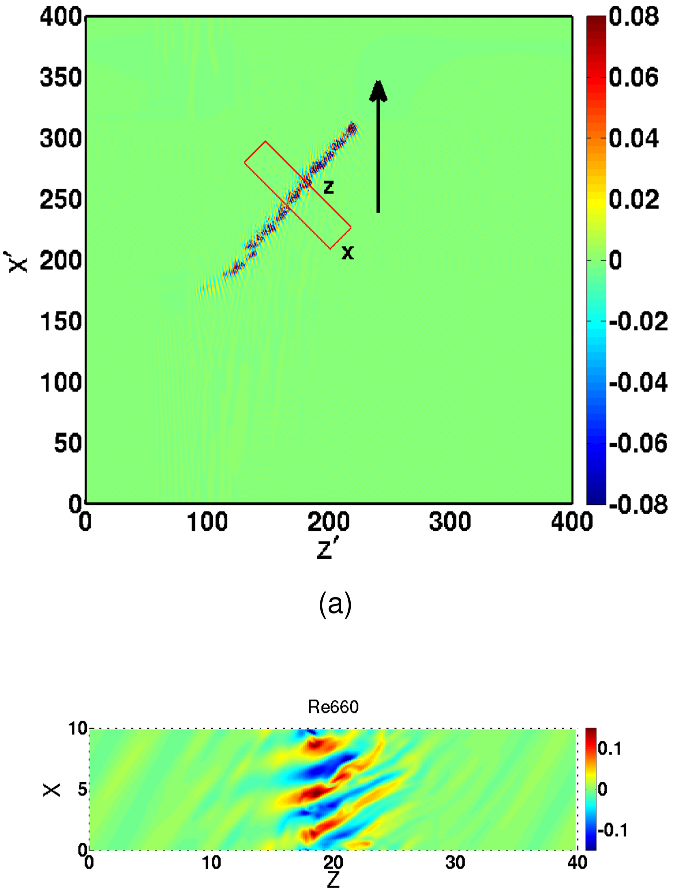

(a)

(b)

Figure 2.2: Concept of the tilted domain. (a)The isolated turbulent stripe at $Re = 660$ showing wall-normal fluctuations. The arrow shows the direction of the mean flow. The stripe appears to be tilted with respect to the streamwise direction at an angle $\theta = 45°$. The tilted rectangular box in red colour, embedded with the appropriate boundary conditions captures the dynamics of the stripe at the selected tilt angle $\theta = 45°$ (b)The turbulent stripe at $Re = 660$ in the tilted domain.

2.4 Numerical methods

In the present study, fluid flows are simulated using direct numerical simulations (DNS), which involve solving the Navier Stokes equations by fully resolving all the relevant scales. The simulations have been performed using two codes. The first code is based on *openpipeflow* code by Ashley P. Willis [Willis, 2017] and which has been adapted by Baofang Song to simulate the PPf in a regular domain. Further modifications were done by the author to simulate the PPf in the tilted domain (here onwards referred to as Code-1). The second code used in this thesis is *Channelflow* code (hereafter referred as Code-2) developed by John Gibson [Gibson, 2014] [Gibson *et al.*, 2008]

Both these codes solve the incompressible Navier-Stokes equations for the fluctuating component of the velocity. The velocity is decomposed as $\boldsymbol{u}_{tot} = \boldsymbol{U} + \boldsymbol{u}$, where $\boldsymbol{U} = (1 - y^2)\cos\theta\hat{\boldsymbol{e}}_x + (1 - y^2)\sin\theta\hat{\boldsymbol{e}}_z$ is the base flow with the components in the x and z direction of the periodic rectangular domain $\hat{\boldsymbol{e}}_x$ and $\hat{\boldsymbol{e}}_z$ respectively. $\theta \in [0, 2\pi]$ is the angle at which the rectangular domain is tilted with respect to the physical streamwise direction.The Navier-Stokes equations for the primitive variables $(\boldsymbol{u}, p)$ take the form

$$\begin{gathered}\frac{\partial \boldsymbol{u}}{\partial t} + (\boldsymbol{u}\cdot\nabla)\boldsymbol{u} + (\boldsymbol{u}\cdot\nabla)\boldsymbol{U} + (\boldsymbol{U}\cdot\nabla)\boldsymbol{u} = -\nabla p_{tot} + \frac{1}{Re}\nabla^2\boldsymbol{U} + \frac{1}{Re}\nabla^2\boldsymbol{u} \\ \nabla\cdot\boldsymbol{u} = 0\end{gathered} \tag{2.9}$$

The no-slip boundary conditions are imposed at the walls of the channel at $(y = \pm 1)$. The periodic boundary conditions are imposed in the homogeneous directions i.e., x and z.

$$\begin{aligned}\boldsymbol{u}(x, \pm 1, z) &= 0 \\ \boldsymbol{u}(x, y, z) &= \boldsymbol{u}(x + L_x, y, z) \\ \boldsymbol{u}(x, y, z) &= \boldsymbol{u}(x, y, z + L_z)\end{aligned} \tag{2.10}$$

As discussed previously, the PPf is a pressure-driven shear flow. Therefore the pressure is not constant in the flow direction. The pressure can be decomposed into a linear and a periodic fluctuating component. Let $P_x(t)x$ and $P_z(t)z$ be the linear in x and linear in z and $p(x, y, z, t)$ be the fluctuating component of the pressure.

$$p_{tot} = p(x, y, x, t) + P_x(t)x + P_z(t)z \tag{2.11}$$

and

$$\nabla p_{tot} = \nabla p(x, y, x, t) + P_x(t)\boldsymbol{e_x} + P_z(t)\boldsymbol{e_z} \tag{2.12}$$

When the constant mass flux condition is imposed, the flow rate averaged over the surfaces normal to the vectors $\boldsymbol{e_x}$ and $\boldsymbol{e_z}$ should remain constant. As discussed in Section 2.5, this is achieved by adjusting the terms $P_x(t)x$ and $P_z(t)z$ such that the mass flux remains constant. The next two sections discuss the spatial discretization and the time-stepping algorithms used to simulate the PPf.

2.5 Code-1

This code solves the Navier-Stokes equations in the Cartesian coordinate system with two periodic directions(x and z) and one inhomogeneous wall-normal direction (y).

2.5.1 Formulation

Equation (2.9) can be written as

$$\begin{aligned} \frac{\partial \boldsymbol{u}}{\partial t} + N(\boldsymbol{u}) &= -\nabla p_{tot} + \frac{1}{Re} L(\boldsymbol{u}) \\ \nabla \cdot \boldsymbol{u} &= 0 \\ \boldsymbol{u}(x, \pm 1, z, t) &= 0 \end{aligned} \tag{2.13}$$

The pressure and velocity are coupled in the Navier Stokes equations. This coupling is tackled by taking the divergence of the Navier Stokes equations (2.13). The resulting equation for the pressure is a Poisson equation called a pressure Poisson equation (PPE).

$$\nabla^2 p_{tot} = -\nabla \cdot N(\boldsymbol{u}) \tag{2.14}$$

In (2.13), the divergence of the linear terms is zero because of the incompressibility condition. At the boundaries, the Neumann condition is defined by

$$\frac{dp_{tot}}{dy} = \boldsymbol{e_y} \cdot \left(-\frac{\partial \boldsymbol{u}}{\partial t} - N(\boldsymbol{u}) + \frac{1}{Re} L(\boldsymbol{u}) \right) \qquad \text{at} \qquad y = \pm 1 \tag{2.15}$$

Now, as explained in section 2.4, the pressure term is decomposed into a fluctuating part and a linear part. Therefore the pressure term can be expanded as follows

$$p_{tot}(x, y, z, t) = \sum_{k=-K}^{K} \sum_{m=-M}^{M} \hat{p}_{k,m}(y, t) e^{i(\alpha k_x x + \beta m_z z)} + P_x(t)x + P_z(t)z \tag{2.16}$$

where k and m are Fourier modes in x and z direction respectively, $\alpha = 2\pi/L_x$, $\beta = 2\pi/L_z$ and L_x ,L_z are the lengths of the domain in x and z directions respectively. Because of the imposed constant mass flux condition, the pressure gradient is time-dependent. In other words, the constant mass flux is maintained across the surfaces normal to x and z (i.e., across the tilted domain sides) by adjusting the pressure term at every time step.

2.5.2 Spatial discretization

This spectral code consists of ***Fourier*×*Fourier*** modes in the two periodic directions and ***Finite difference*** with 9-point stencil in the wall normal direction. All lengths are normalized with h. Therefore y varies as $y = \pm 1$. The wall normal direction the grid points are defined as Gauss-Lobatto points i.e. $y_j = \cos(\frac{j\pi}{N-1})$ where $j \in [0, N-1]$. The fluctuating component of the velocity is expanded as follows

$$\boldsymbol{u}(x, y, z, t) = \sum_{k=-K}^{K} \sum_{m=-M}^{M} \hat{\boldsymbol{u}}_{k,m}(y, t) e^{i(\alpha k_x x + \beta m_z z)} \tag{2.17}$$

By substituting (2.17) in (2.13), we project the equations in Fourier space which results in a system of ordinary differential equations, with 3 equations for each (k,m) pair. The nonlinear terms are evaluated using convolution which results in “aliasing” of the Fourier modes. To make the convolution terms free of aliasing, we use the $3/2$ dealiasing rule [Canuto, 1988].

2.5.3 Algorithm

The linear terms are integrated implicitly. However, to reduce the computation cost, nonlinear terms are integrated using explicit methods. Here, the time integration is performed using a second-order backward differentiation for linear terms and the Adam-Bashforth method for the nonlinear terms.

$$\frac{3\hat{\boldsymbol{u}}^{n+1}-4\hat{\boldsymbol{u}}^{n}+\hat{\boldsymbol{u}}^{n-1}}{2\triangle t}+2N(\hat{\boldsymbol{u}}^{n})-N(\hat{\boldsymbol{u}}^{n-1})=-\nabla p^{n+1}+\frac{1}{Re}L(\hat{\boldsymbol{u}}^{n+1}) \tag{2.18}$$

In the beginning with the given initial condition $\hat{\boldsymbol{u}}^0$ we set $\hat{\boldsymbol{u}}^{-1} = \hat{\boldsymbol{u}}^0$ to kick-start the integration algorithm.

1. The pressure Poisson equation in discretized form is as follows.

$$\begin{aligned} \nabla^2\tilde{p}^{n+1} &= \nabla\cdot(-2N(\hat{\boldsymbol{u}}^{n})+N(\hat{\boldsymbol{u}}^{n-1})) \\ \frac{dp}{dy} &= 0 \qquad\qquad \text{at} \qquad y=\pm 1 \end{aligned} \tag{2.19}$$

   At the boundary, the pressure gradient in the wall-normal direction vanishes because of the no-slip boundary conditions and the incompressibility condition. The above equation is solved by taking the inverse of the operator using LU decomposition. The resulting pressure term is a predictor pressure step $\tilde{p}^{n+1}$ which is then used to compute the predictor velocity field.

2. The predictor velocity $\hat{\boldsymbol{u}}^*$ is obtained using the no-slip boundary conditions and the predictor pressure.

$$\begin{aligned} &\frac{3\hat{\boldsymbol{u}}^{*}-4\hat{\boldsymbol{u}}^{n}+\hat{\boldsymbol{u}}^{n-1}}{2\triangle t}+2N(\hat{\boldsymbol{u}}^{n})-N(\hat{\boldsymbol{u}}^{n-1}) \\ &\quad=-\nabla(\tilde{p}^{n+1}+P_x x+P_z z)+\frac{1}{Re}L(\hat{\boldsymbol{u}}^{*}) \end{aligned} \tag{2.20}$$

   No-slip boundary conditions are maintained at the walls as $\boldsymbol{u}^* = 0$ at $y = \pm 1$.

   The pressure terms P_x and P_z are solved by imposing the constant mass flux condition in the periodic directions as

$$\begin{aligned} \int_0^{L_x}\int_{-1}^{1} u_x^* dydx &= C1 \\ \int_0^{L_z}\int_{-1}^{1} u_z^* dydz &= C2 \end{aligned} \tag{2.21}$$

Due to the Fourier representation of the velocity $\boldsymbol{u}^*$ the modes with $k \neq 0$ and $m \neq 0$ do not contribute to the mass flux. Therefore the pressure gradients P_x and P_z which depend only on time, act on $(k, m) = (0, 0)$. Therefore,

$$\begin{aligned} \int_0^{L_x} \int_{-1}^{1} u_x^* dy dx = L_x \int_{-1}^{1} \hat{u}^*_{x(0,0)} dy = C1 \\ \int_0^{L_z} \int_{-1}^{1} u_z^* dy dz = L_z \int_{-1}^{1} \hat{u}^*_{z(0,0)} dy = C2 \end{aligned} \tag{2.22}$$

Next $\hat{u}^*_{x(0,0)}$ and $\hat{u}^*_{z(0,0)}$ are solved using (2.20) and (2.22). $u_{\widehat{y_{(k,m)}}}{}^*$ and the remaining modes of $\hat{u_x}^*$ and $\hat{u_z}^*$ can be obtained by solving (2.20) alone.

3. In the corrector step, the pressure $\tilde{p}^{n+1}$ is corrected in order to satisfy the incompressibility condition. In the predictor step, the condition $\nabla \cdot \boldsymbol{u}^* = 0$ is not imposed, leaving the predictor velocity field $\boldsymbol{u}^*$ not divergence-free. In the corrector step the pressure $\tilde{p}^{n+1}$ is corrected for the incompressibility condition. Now, consider the following equation.

$$\begin{aligned} \frac{3\boldsymbol{u}^{n+1} - 3\boldsymbol{u}^*}{2\triangle t} &= -\nabla(p^{n+1} - \tilde{p}^{n+1}) \\ \nabla \cdot \boldsymbol{u}^{n+1} &= 0 \\ \boldsymbol{u}^{n+1} &= \boldsymbol{u}^* = 0 \qquad \text{at } y = \pm 1 \end{aligned} \tag{2.23}$$

Defining $\varrho = \frac{2\triangle t}{3}(p^{n+1} - \tilde{p}^{n+1})$, we have

$$\begin{aligned} \nabla^2 \varrho &= -\nabla \cdot (\boldsymbol{u}^{n+1} - \boldsymbol{u}^*) \qquad \text{i.e. } \nabla^2 \varrho = -\nabla \cdot \boldsymbol{u}^* \\ \frac{\partial \varrho}{\partial y} &= 0 \qquad \text{at } y = \pm 1 \end{aligned} \tag{2.24}$$

Using LU decomposition, ϱ is determined. Then the pressure and the velocity can be corrected as

$$\begin{aligned} p^{n+1} &= \tilde{p}^{n+1} + \frac{3}{2\triangle t} \varrho \\ \boldsymbol{u}^{n+1} &= \boldsymbol{u}^* - \nabla \varrho \end{aligned} \tag{2.25}$$

This code is parallelized with MPI. For further details of the MPI-implementation refer to the documentation on *openpipeflow* website. A precursor to the Code-1 can be found in the Ph.D. dissertation by Baofang Song, as a routine to simulate pipe flow [Song, 2014].

2.6 Code-2

This code has been developed by John F. Gibson [Gibson, 2014]. It is written as a set of C++ classes, designed to simulate the wall-bounded incompressible flows (plane Poiseuille and plane Couette) in a 3D rectangular periodic domain. This code also uses spectral discretization viz. ***Fourier*** × ***Chebyshev*** × ***Fourier***, with the Fourier discretization in the two periodic directions and the Chebyshev polynomials in the inhomogeneous i.e. wall-normal direction.

2.6.1 Formulation

The code solves the Navier-Stokes equations

$$\begin{aligned} \frac{\partial \boldsymbol{u}_{tot}}{\partial t} + (\nabla \times \boldsymbol{u_{tot}}) \times \boldsymbol{u}_{tot} &= -\nabla q + \frac{1}{Re}\nabla^2 \boldsymbol{u}_{tot} \\ \nabla \cdot \boldsymbol{u}_{tot} &= 0 \\ \boldsymbol{u}_{tot}(x, \pm 1, z) &= 0 \end{aligned} \tag{2.26}$$

where $q = p + \frac{1}{2}|\boldsymbol{u}_{tot}|^2$ is a dynamic pressure. As explained in section 2.4 the velocity is decomposed as the laminar base flow and a fluctuating component

$$\boldsymbol{u}_{tot} = \boldsymbol{U} + \boldsymbol{u} \tag{2.27}$$

where $\boldsymbol{U} = U_x(y)\hat{\boldsymbol{e}}_x + U_z(y)\hat{\boldsymbol{e}}_z$

The pressure term is also decomposed as described in equation (2.12). After the decomposition, equation (2.26) takes the form

$$\begin{aligned} \frac{\partial \boldsymbol{u}}{\partial t} + \nabla\left(p + \frac{1}{2}\boldsymbol{u}\cdot\boldsymbol{u}\right) = \frac{1}{Re}\nabla^2\boldsymbol{u} - \left((\boldsymbol{u}\times\nabla)\times\boldsymbol{u} + U_x\frac{\partial \boldsymbol{u}}{\partial x} + U_z\frac{\partial \boldsymbol{u}}{\partial z} + v\frac{\partial U_x}{\partial y}\hat{\boldsymbol{e}}_x + v\frac{\partial U_z}{\partial y}\hat{\boldsymbol{e}}_z\right) \\ + \left(\frac{1}{Re}\frac{\partial^2 U_x}{\partial}y^2 + P_x(t)\right)\hat{\boldsymbol{e}}_x + \left(\frac{1}{Re}\frac{\partial^2 U_z}{\partial}y^2 + P_z(t)\right)\hat{\boldsymbol{e}}_z \end{aligned} \tag{2.28}$$

These equations can be written as

$$\frac{\partial \boldsymbol{u}}{\partial t} + \nabla q = L(\boldsymbol{u}) - N(\boldsymbol{u}) + C(t) \tag{2.29}$$

The term $C(t)$ is a time dependent forcing term which is adjusted at every timestep to maintain constant mass flux across the mean flow directions.

2.6.2 Spatial discretization

The velocity is expanded in the following form.

$$\boldsymbol{u}(x,y,z,t) = \sum_{k_x=-N_x/2+1}^{N_x/2} \sum_{n=0}^{N_y} \sum_{k_z=-N_z/2+1}^{N_z} \hat{\boldsymbol{u}}_{k_x,n_y,k_z}(y,t)\hat{T}_n(y,t)e^{2\pi i(k_x x/L_x + k_z z/L_z)} \tag{2.30}$$

where N_x and N_z are the number of Fourier modes in the periodic directions. N_x and N_z are even. N_y is the number of Chebyshev modes in the wall normal direction. L_x and L_z are the lengths of the domain in x and z directions respectively. The grid points in the wall normal direction are defined as Gauss-Lobatto points such that $y_j = \cos(\frac{j\pi}{N-1})$ where $j \in [0, N-1]$. The n^{th} Chebyshev polynomial is $T_n(y,t) = \cos(n\cos^{-1}(y))$ where $y \in [-1,1]$.

The code is designed to maintain either a constant mass flux or a constant pressure gradient. In this study, we have used the constant mass flux constraint which in turn maintains constant Re based on the centerline velocity U_{cl}.

2.6.3 Algorithm

The equations are integrated in time by using a 3rd order Adam-Bashforth backward differentiation method with the linear terms treated with a third-order backward difference and the nonlinear terms with the 3rd order Adam-Bashforth method. The discretization is as follows.

$$\begin{aligned} \frac{1}{\triangle t}\left(\frac{11}{6}\boldsymbol{u}^{n+1} - 3\boldsymbol{u}_n + \frac{3}{2}\boldsymbol{u}^{n-1} - \frac{1}{3}\boldsymbol{u}^{n-2}\right) &= 3N(\boldsymbol{u}_n) - 3N(\boldsymbol{u}_{n-1}) \\ &+ N(\boldsymbol{u}_{n-2}) + L(\boldsymbol{u}_{n+1}) \end{aligned} \tag{2.31}$$

The algorithm uses a variable time-step. The constraint is a CFL condition which is defined as

$$C = \frac{u \triangle t}{\triangle x} \tag{2.32}$$

where u is a magnitude of velocity, $\triangle t$ is a timestep and $\triangle x$ is a spatial resolution. Therefore the time-step is chosen such that the $C < 0.55$. For more details of the time integration see documentation on ***channelflow*** and chapter 4 of [Peyret, 2010].

2.7 Bisection

In a variety of shear flows like PPf, PCf, HPf turbulence exists subcritically i.e., despite the laminar base flow being linearly stable. It suggests that there are two distinct regimes in the phase space (a) a fixed point that corresponds to the laminar base flow and (b) a chaotic attractor/saddle that corresponds to the turbulent flow [Skufca *et al.*, 2006; Faisst and Eckhardt, 2004].

These laminar and the turbulent states are separated by a hypersurface or a separatrix in phase space [Skufca *et al.*, 2006; Schneider *et al.*, 2008]. A trajectory starting from an initial condition in phase space ends up either on the laminar or the chaotic/turbulent set depending upon which side of the separatrix the initial condition lies. However, the initial conditions which lie *on* the separatrix neither go to the laminar fixed point nor to the turbulent/chaotic set but remain *on* the separatrix and eventually converge to the relative attractor on it. These trajectories on the separatrix are called the 'edge,' and the relative attractor to which these 'edge' trajectories converge is called the 'edge state' [Duguet *et al.*, 2009].

These relative attractors are either can be chaotic in nature or the exact invariant solutions (ECS) of the Navier-Stokes equations. These ECS can be equilibria (EQ), traveling waves (TW), periodic orbits (PO) or relative periodic orbits (RPO). It should be noted that in a co-moving frame, TWs are EQs and RPOs are POs. These solutions are important in order to study the turbulence from the dynamical system theory perspective.

To find an edge state the method used is described in Schneider et al. [Schneider and Eckhardt, 2009]. Let $\boldsymbol{u_0}(\boldsymbol{x})$ be an initial condition of any trajectory that visits the turbulent attractor. Clearly the initial condition lies on a *turbulent* side of the separatrix. Now consider a scalar $\lambda \in (0, 1)$ which is used to scale the initial condition as $\lambda \boldsymbol{u_0}(\boldsymbol{x})$

Let $\boldsymbol{u_L}(\boldsymbol{x}) = \lambda_L \boldsymbol{u_0}(\boldsymbol{x})$ be an initial condition such that the trajectory starting from it goes to the laminar fixed point and $\boldsymbol{u_T}(\boldsymbol{x}) = \lambda_T \boldsymbol{u_0}(\boldsymbol{x})$ be the initial condition such that the trajectory staring from it goes to the turbulent attractor. Now bisecting between λ_L and λ_T for n iterations, we find an initial condition which is very close to the edge of chaos. Then $\boldsymbol{u}_0^*(\boldsymbol{x}) = \lambda^* \boldsymbol{u_0}(\boldsymbol{x})$ is the initial condition such that a trajectory starting from that initial condition visits the relative attractor on the edge called as edge state $\boldsymbol{u}^*$. In

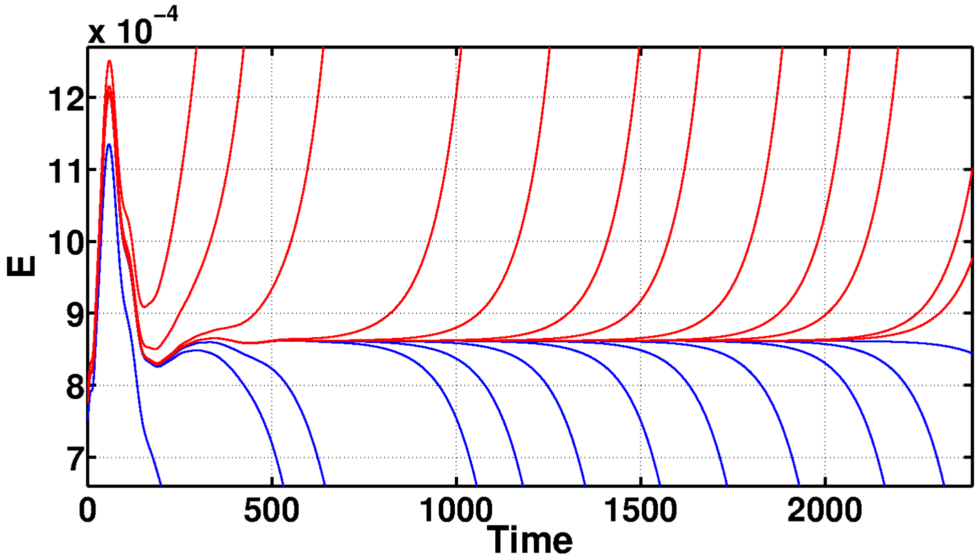

Figure 2.3: The edge tracking at $Re = 720$ at a tilt angle $\theta = 35°$. The trajectories in red are the turbulent trajectories which go to the chaotic set and the trajectories in blue go to the laminar fixed point. The flat plateau between these blue and red trajectories represents the edge state. As the bisection method brings the initial condition closer and closer to the edge of chaos, the time the trajectories spend near the edge state also increases. In the case demonstrated here, the edge state was found to be a traveling wave.

practice, the initial condition on the edge of chaos is determined with a finite numerical error, usually $|\lambda_L - \lambda_T| \approx 10^{-10}$. This provides an approximate invariant solution which is converged further using the Newton-Krylov algorithm [Viswanath, 2007] as explained in Section 2.8. The stability of these invariant solutions is quantified using Arnoldi iterations as described in Section 2.9

2.8 Newton-Krylov method

In PPf, the invariant solutions of the Navier-Stokes equations are traveling waves and relative periodic orbits. These solutions are approximated using the bisection methods and then further converged using a root-finding algorithm called the Newton-Krylov method. The corresponding routine from the channelflow code - based on the Newton-Krylov-Hookstep algorithm by D. Viswanath [Viswanath, 2007] - is used for converging the solutions.

Let ϕ^{τ} be the evolution operator after time τ, and σ be a spatial shift operator such that $(\sigma \boldsymbol{u})(\boldsymbol{x}) = \boldsymbol{u}(\boldsymbol{x} + \boldsymbol{\Delta x})$, where $\boldsymbol{\Delta x}$ is a two-dimensional vector. Then for traveling wave solutions, we look for $G(\boldsymbol{u}, \sigma, \tau) = |\phi^{\tau}(\boldsymbol{X}) - \sigma\boldsymbol{X}|^2 = 0$ for any arbitrary τ and given $\boldsymbol{\Delta} x$. For relative periodic orbit, we have $G(\boldsymbol{u}, \sigma, T) = |\phi^{T}(\boldsymbol{X}) - \sigma\boldsymbol{X}|^2 = 0$ for a fixed time period T and given $\boldsymbol{\Delta} x$.

Now let $\boldsymbol{X} = [\boldsymbol{u}, \sigma, T]$ be a vector which is an initial guess for the relative periodic orbit. Let $\boldsymbol{X}^* = [\boldsymbol{u}^*, \sigma^*, T^*]$ be a solution such that $G(\boldsymbol{X}^*) = 0$. Let $\boldsymbol{X}^* = \boldsymbol{X}_N + d\boldsymbol{X}_N$, where N represents the n^{th} Newton step.

$$G(\boldsymbol{X}^*) = G(\boldsymbol{X}_N + d\boldsymbol{X}_N) \qquad \textbf{i.e.}$$

$$0 = G(\boldsymbol{X}_N) + J(\boldsymbol{X}_N)d\boldsymbol{X}_N + O(|d\boldsymbol{X}_N|^2) \tag{2.33}$$

where J is the Jacobian with

$$J_{i,j} = \frac{\partial G_i}{\partial x_j} \tag{2.34}$$

Dropping the higher-order terms, the Newton equation to be solved is

$$J(\boldsymbol{X}_N)d\boldsymbol{X}_N = -G(\boldsymbol{X}_N) \tag{2.35}$$

We want to find a correction dX_N such that above equation is satisfied. In practice dX_N is determined such that $|J(\boldsymbol{X}_N)d\boldsymbol{X}_N + G(\boldsymbol{X}_N)| < \epsilon$ where $\epsilon < 10^{-13}$.

Equation (2.35) is of the form

$$\boldsymbol{A}\boldsymbol{x} = \boldsymbol{b} \tag{2.36}$$

Let $\boldsymbol{A}$ be a matrix with $\boldsymbol{A} \in \mathbb{R}^{m\times m}$,$\boldsymbol{x} \in \mathbb{R}^{m\times 1}$and $\boldsymbol{b} \in \mathbb{R}^{m\times 1}$.

This problem is then solved by implementing the GMRES-Krylov subspace algorithm [Saad and Schultz, 1986] [Knoll and Keyes, 2004] with the hookstep suggested by D. Viswanath.

The **G**eneralized **M**inimal **RES**idual or GMRES method solves a least square problem at each step. At every p^{th} step, the solution $\boldsymbol{x}^* = \boldsymbol{A}^{-1}\boldsymbol{b}$ is approximated by a vector $\boldsymbol{x}_p \in \mathbb{K}_p$. $\mathbb{K}_p$ is a p^{th} order Krylov space. The residual $\parallel \boldsymbol{r}_p \parallel_2 = \parallel \boldsymbol{A}\boldsymbol{x}_p - \boldsymbol{b} - \parallel_2$ is minimized in each iteration. The corresponding Krylov matrix is given by $\boldsymbol{K}_p = [\boldsymbol{b}, \boldsymbol{A}\boldsymbol{b}, \boldsymbol{A}^2\boldsymbol{b}...\boldsymbol{A}^{p-1}\boldsymbol{b}] \in \mathbb{R}^{m\times p}$. Now, the orthonormal basis $\boldsymbol{Q}_p \in \mathbb{R}^{m\times p}$ of $\boldsymbol{K}_p$ is formed by Arnoldi iterations. The vector $\boldsymbol{x}_p$ can be written as $\boldsymbol{x}_p = \boldsymbol{Q}_p\boldsymbol{y}_p$ where $\boldsymbol{y}_p \in \mathbb{R}^p$. The Arnoldi iteration also computes an upper Hessenberg matrix $\hat{\boldsymbol{H}}_p$ such that $\boldsymbol{A}\boldsymbol{Q}_p = \boldsymbol{Q}_{p+1}\hat{\boldsymbol{H}}_p$. Because of the orthogonality of the matrix $\boldsymbol{Q}_p$, we have

$$\parallel \boldsymbol{r}_p \parallel_2 = \parallel \boldsymbol{A}\boldsymbol{x}_p - \boldsymbol{b} \parallel_2 \qquad = \parallel \boldsymbol{A}\boldsymbol{Q}_p\boldsymbol{y}_p - \boldsymbol{b} \parallel_2 = \parallel \boldsymbol{Q}_{p+1}\hat{\boldsymbol{H}}_p\boldsymbol{y}_p - \boldsymbol{b} \parallel_2 \tag{2.37}$$

Multiplication by $\boldsymbol{Q}_{p+1}^T$ does not change the norm as $\boldsymbol{Q}_{p+1}^T$ is a unitary matrix.

$$\parallel \boldsymbol{r}_p \parallel_2 = \parallel \hat{\boldsymbol{H}}_p\boldsymbol{y}_p - \boldsymbol{Q}_{p+1}^T\boldsymbol{b} \parallel_2 = \parallel \hat{\boldsymbol{H}}_p\boldsymbol{y}_p - \beta\boldsymbol{e}_1 \parallel_2 \tag{2.38}$$

This least-squares problem is then solved by QR factorization. At the end of the GMRES iterations a Newton step $d\boldsymbol{X}_N$ is determined. Then the Newton-iteration is continued further till $|J(\boldsymbol{X}_N)d\boldsymbol{X}_N + G(\boldsymbol{X}_N)| < \epsilon$ where $\epsilon < 10^{-13}$. If the Newton step $d\boldsymbol{X}_N$ does not reduce the residual, a smaller step -a hookstep - $d\boldsymbol{X}_h$ is obtained by minimizing $\parallel J(\boldsymbol{X}_N)d\boldsymbol{X}_h + G(\boldsymbol{X}_N) \parallel_2$ such that $\parallel d\boldsymbol{X}_h \parallel_2{}^2 < \delta^2$. The δ is a radius of a trust region. It is determined by comparing the reduction in residual obtained by considering step $d\boldsymbol{X}_h$ to the reduction in residual predicted by the linearized model $G(\boldsymbol{X}_N) + J(\boldsymbol{X}_N)d\boldsymbol{X}_h$. The region δ is increased in steps such that the reduction is large and marginally accurate.

Continuation of the solutions in the parametric space is performed using the quadratic extrapolation. Here, the guess for the solution in the parameter space is obtained from quadratic extrapolation based on three converged solutions in the parametric space. The guess is then further converged using the Newton-Krylov- Hookstep algorithm.

2.9 Computation of the Eigenvalues

The linear stability of the exact coherent solutions is determined by identifying the eigenvalues of these invariant solutions. The eigenvalues are computed by iterative methods.

Let $\boldsymbol{A}$ be a matrix with $\boldsymbol{A} \in \mathbb{C}^{m\times m}$. The n^{th} Krylov-subspace for $\boldsymbol{A}$ is

$$\boldsymbol{K}_n = \left[\boldsymbol{p}, \boldsymbol{A}\boldsymbol{p}, \boldsymbol{A}^2\boldsymbol{p}\boldsymbol{A}^{n-1}\boldsymbol{p}\right] \in \mathbb{C}^{m\times n} \tag{2.39}$$

where, $\boldsymbol{p} \in \mathbb{C}^{m\times 1}$ be an initial vector.

An approximate eigenpair $(\lambda, \tilde{\boldsymbol{v}})$ is sought through orthogonal projection of subspace $\boldsymbol{K}$ by imposing a condition

$$\langle A\tilde{\boldsymbol{v}} - \lambda\tilde{\boldsymbol{v}}, q\rangle = 0 \tag{2.40}$$

where $\boldsymbol{Q}_n = \{q_1, q_2, ..., q_n\}$ is an orthonormal basis of Krylov subspace $\boldsymbol{K}$ and $\tilde{\boldsymbol{v}} \in \boldsymbol{K}$. Let $\tilde{\boldsymbol{v}} = \boldsymbol{Q}_n\boldsymbol{y}$. Therefore, now the Equation 2.40 becomes

$$\langle A\boldsymbol{Q}_n\boldsymbol{y} - \lambda\boldsymbol{Q}_n\boldsymbol{y}, q_k\rangle = 0, \qquad k = 1, .., n \tag{2.41}$$

This means, $\boldsymbol{Q}_n^* A\boldsymbol{Q}_n\boldsymbol{y} = \lambda\boldsymbol{y}$. Therefore, the eigenvalues λ_k of $\boldsymbol{H}_n = \boldsymbol{Q}_n^* A\boldsymbol{Q}_n$ where $k = 1, ...n$, are computed. The eigenvalues are called as Ritz eigenvalues and the vectors $\boldsymbol{Q}_n\boldsymbol{y}$ are corresponding Ritz eigenvectors.

The Arnoldi algorithm computes the orthonormal basis $\boldsymbol{Q}$ of Krylov subspace $\boldsymbol{K}$ of $\boldsymbol{A}$ and transforms the matrix $\boldsymbol{K}$ into $|bmH$ upper Hessenberg matrix. It reduces the complexity of the problem because of the zeros in the lower triangle of the matrix. Then the eigenvalues of $|bmH$ are computed with QR- algorithm.

Consider an evolution operator $\boldsymbol{F}^t$ such that $\boldsymbol{F}^T(\boldsymbol{u}(t)) = \boldsymbol{u}(t+T)$. Then, for an equilibrium we have $\boldsymbol{F}^T(\boldsymbol{u}^*) = \boldsymbol{u}^*$. Now the stability of the equilibrium solution $\boldsymbol{u}^*$ can be determined by investigating how a small perturbation $d\boldsymbol{u}$ on $\boldsymbol{u}^*$ develops. The eigenvalues of the operator $\boldsymbol{S}$ where, $\boldsymbol{S}(\boldsymbol{u}^*)d\boldsymbol{u} = \boldsymbol{F}^T(\boldsymbol{u}^* + d\boldsymbol{u}) - \boldsymbol{F}^T(\boldsymbol{u}^*)$, demonstrate the stability of the invariant solution $\boldsymbol{u}^*$.

2.10 Observables

In order to understand the temporal evolution of the turbulent structures, we need to monitor the temporal evolution of a few scalars related to the flow. Unlike in the experiments, in the simulations, we can define a variety of scalars with a global measure. The perturbation kinetic energy averaged over the entire domain is one such quantity.

The perturbation kinetic energy is defined as E by $E(t) =< e(x,y,z,t) >$ where $e(x,y,z,t) = |\boldsymbol{u}(x,y,z,t)|^2$ is the local (pointwise) kinetic energy and $< \cdot >$ represents the spatial averaging. E can be re-expressed as

$$E(t) = \frac{1}{L_x L_y L_z}\int_{-1}^{1}\left(\int_0^{L_z}\int_0^{L_x} |\boldsymbol{u}|^2 dxdz\right)dy. \tag{2.42}$$

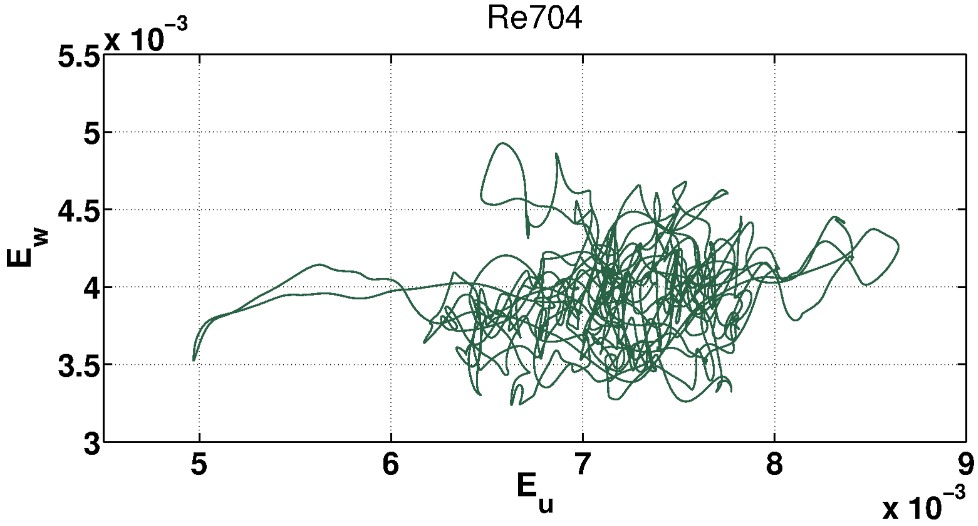

Figure 2.4: A trajectory of turbulent dynamics at $Re = 704$ in a domain tilted at $\theta = 45^o$. The portrait of a very high dimensional state space on two dimensions is achieved by computing the scalars E_u and E_w along with the temporal evolution of the trajectory

In the case of the tilted domain, any velocity field $\boldsymbol{u}$ decomposes into three components u, v and w, where u is the component parallel to the shorter side of the domain, the component w, parallel to the longer side, and v is the wall-normal velocity component. It is possible to define the kinetic energy by each component, such as

$$E_u(t) = \frac{1}{L_x L_y L_z} \int_{-1}^{1} \left(\int_0^{L_z} \int_0^{L_x} u^2 dx dz \right) dy. \tag{2.43}$$

$$E_v(t) = \frac{1}{L_x L_y L_z} \int_{-1}^{1} \left(\int_0^{L_z} \int_0^{L_x} v^2 dx dz \right) dy. \tag{2.44}$$

$$E_w(t) = \frac{1}{L_x L_y L_z} \int_{-1}^{1} \left(\int_0^{L_z} \int_0^{L_x} w^2 dx dz \right) dy. \tag{2.45}$$

Here it is noted that $E = E_u + E_v + E_w$. These scalar observables are used to analyze the three-dimensional phase portraits and to visually identify the type of asymptotic temporal dynamics obtained for a particular value of Re. As depicted in figure 2.4, these observables, when plotted on 2-D or 3-D plots, help us in visualizing the state space of the dynamics.

Another observable is $e_i(z)$ which is perturbation energy of i^{th} component of the fluctuation velocity field averaged over x and y as a function of z.

$$e_i(z) = \frac{1}{L_x L_y} \int_{-1}^{1} \left(\int_0^{L_x} {u_i}^2 dx \right) dy. \tag{2.46}$$

$$\tag{2.47}$$

3 Experiments in channel flow

Being one of the canonical wall-bounded shear flows, a significant amount of experimental as well as theoretical studies have been dedicated to channel flow or plane Poiseuille flow (PPf). A linear stability analysis gives the value of Re below which the laminar base flow of PPf is linearly stable for infinitesimal disturbances. Nishioka et al. [Nishioka *et al.*, 1975] experimentally verified the linear stability of channel flow. They also noted that below the critical $Re_{LS} = 5772$ [Orszag, 1971], the subcritical transition to turbulence happens when the intensity of the disturbance exceeds some critical threshold value, which increases with decreasing Re. However, even in the earlier experiments, it is observed that PPf has sustained turbulence at much lower Re than the one predicted by the linear stability analysis [Davies *et al.*, 1928].

Clearly, the critical Re at the onset of turbulence is not the one predicted by the linear stability analysis where the base laminar flow turns to turbulence pertaining to infinitesimal perturbations, but the critical point is Re above which turbulence sustains following an appropriate initial condition. Visualizations of the flow also make it clear that the structural components of subcritical turbulence are different from the shape of the unstable modes predicted by the linear stability analysis, unlike for convection rolls. Narayanan [Narayanan, 1968] performed experiments in reverse transition where Re of turbulent flow is reduced by widening the channel and reported the critical value as $Re \approx 2100$. In the experiments to measure skin-friction, Patel, and Head [Patel and Head, 1969] reported $Re \approx 975$ as a lower critical value for the transition. In a numerical study of three-dimensional finite-amplitude disturbances to the PPf, Orszag, et al. [Orszag and Patera, 1980] stated the critical $Re \approx 1000$.

The first flow visualizations in a channel with water seeded with particles is due to Carlson et al.[Carlson *et al.*, 1982]. It was observed that the turbulence was in the form of localized patches surrounded by the laminar flow. Here, the turbulent patches are called “spots”. This study again claims the critical $Re \approx 1000$. Later experimental studies also reported the critical value of Re around 1000 [Alavyoon *et al.*, 1986; Lemoult *et al.*, 2012; Lemoult *et al.*, 2013; Lemoult *et al.*, 2014]

In most of the earlier experiments, the studies were carried out in relatively shorter channels, because of which turbulent structures leave the channels in a relatively shorter time. Due to this, observing the evolution of the turbulent structures over large timescales becomes difficult. In longer and wider channels, the “spots” created by perturbing the flow further evolve into localized stripes surrounded by the laminar flow oblique to the mean flow direction. This was confirmed in the experiments by Hashimoto et al. [Hashimoto *et al.*, 2009] and in the various numerical studies [Tsukahara *et al.*, 2010; Aida *et al.*, 2011; Xiong *et al.*, 2015; Tao *et al.*, 2018; Shimizu and Manneville, 2018]

The numerical studies [Xiong *et al.*, 2015] show that the stripes can exist at Re as low as 660. However, the authors also noted that the stripes eventually interact with each other because of the periodic boundary conditions imposed on the numerical domain and eventually decay until a value of 1000 is reached. Recent experiments by Sano and Tamai [Sano and Tamai, 2016] suggested that the critical point above which these stripes can sustain indefinitely, to be $Re_c = 830$ and claimed that the transition to turbulence in PPf falls under $2 + 1$ dimensional directed percolation (DP) universality class. Directed percolation has been suggested as an appropriate framework for other planar shear flows [Shi *et al.*, 2013; Chantry *et al.*, 2017]. In directed percolation type transition [Hof *et al.*, 2006; Hof *et al.*, 2008; Avila *et al.*, 2010], the turbulence remains transient, and laminar flow is the only attractor, i.e., the unique absorbing phase. In a numerical study by Tao et al. [Tao *et al.*, 2018], it was proposed that the transition scenario is more complicated than DP and has two stages. Near $Re \sim 700$, it reports, the individual stripes elongate indefinitely and can not contaminate the other planar dimension, and therefore the overall turbulence remains sparse and turbulent fraction depends on the initial conditions. A more recent numerical study [Shimizu and Manneville, 2018] advocates a different two-step process. Here, the stripes are sustained for $Re > 700$ but take the form of ’concrete coherent structures’ and the ’non-trivial chaotic flow’ only arises at a masked DP transition at $Re = 976$.

With this background, we aim to determine the critical point of PPf robustly. The main challenge, in determining the critical Re for sustained turbulence in the wall-bounded shear flows like pipe flow and channel flow, is the long timescales involved in the growth and the decay processes. The advection of turbulent structures with the mean flow severely restricts the observation times. Therefore, performing experiments in PPf is not without difficulties. To study localized structures around the onset of turbulence, it is necessary to have a large aspect ratio channel in terms of length (L_x/L_y) and breadth (L_z/L_y). Also, these structures advect in the streamwise as well as spanwise direction. Therefore unlike pipe experiments, where the observation time can be increased by just increasing the length of the pipe in the axial direction, here the channel must be extended in the streamwise as well as the spanwise direction. In the present study, the critical point is determined by performing experiments in a channel with a large aspect ratio. Other properties of stripe turbulence near the onset of turbulence, like the angle of the stripes, advection velocity, etc. are also studied. We also propose the mechanisms which are responsible for the proliferation of turbulence near onset.

3.1 Experimental setup

The setup consists of a channel test section formed by two flat plates separated by a narrow gap. The bottom plate is a 10 mm thick aluminium plate. The top plate is made of 10 mm thick transparent float glass. Both plates are 2000 mm in length. The bottom plate is 365 mm wide, and just near the entrance, the width of the plate reduces to 290 mm, whereas, the top plate is 290 mm wide. A narrow gap of 1 mm is maintained between these two plates with the help of two 1 mm stainless steel spacers. These spacers run parallel to each other along the channel. The spacers are fixed to the bottom plate with small screws. Rubber strings with circular cross-section are placed adjacent to the inner walls of the spacers act as gaskets and make the channel leak-proof. The distance between the side walls is carefully maintained at 245 mm. The glass plate is placed on the spacers that are sandwiched between the bottom aluminium plate and the transparent top plate. The top plate is held to the aluminium plate with the help of 54 L-clamps. The dimensions of the channel are- $(L_x, L_y, L_z) =$

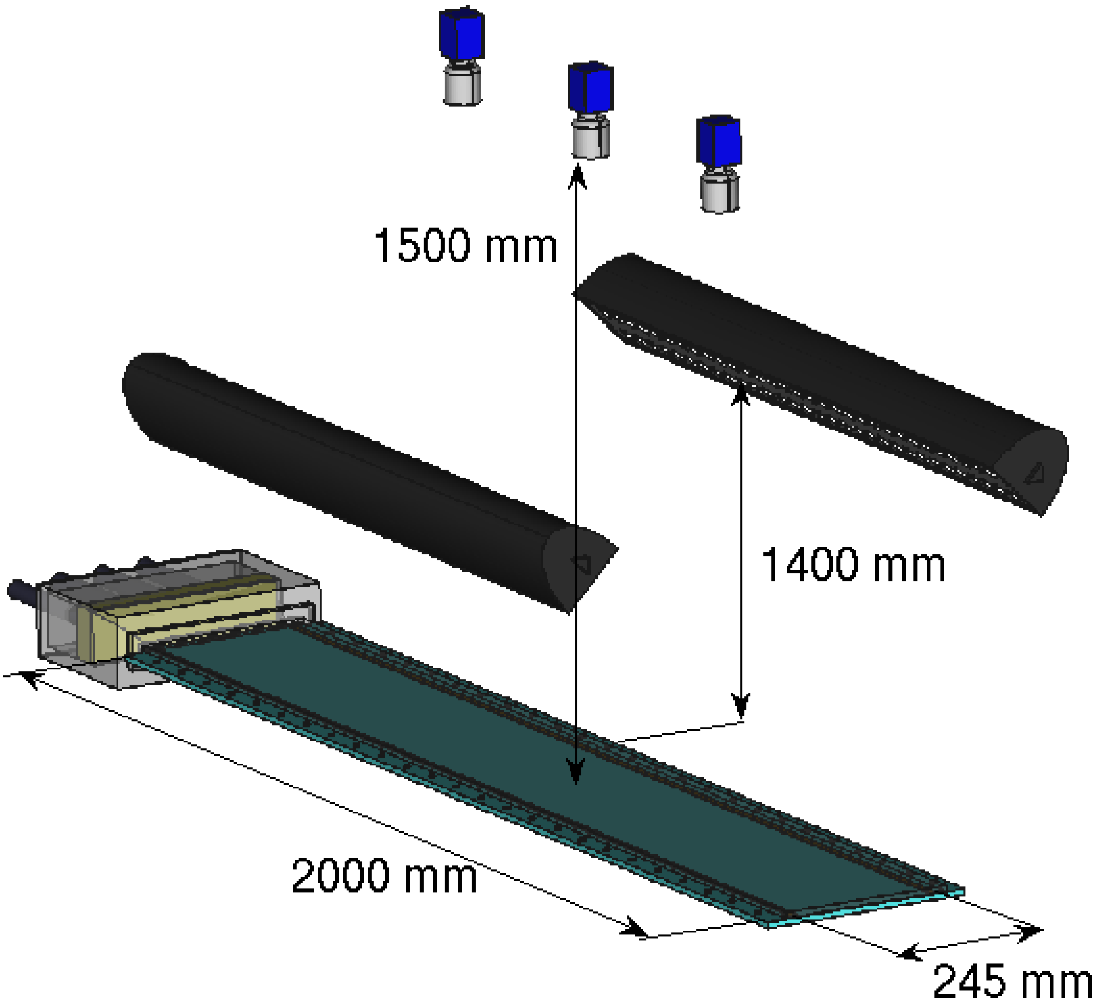

Figure 3.1: Experimental setup.

$(4000h, 2h, 490h)$, where L_x,L_y and L_z are lengths along the streamwise direction, wall-normal direction and spanwise direction respectively. The gap between the two plates is $L_y = 2h = 1$ mm.

The working fluid is water seeded with particles for flow visualization. A reservoir kept at the height of 21 m giving enough pressure head for the water to flow through the channel. The water level in the reservoir is maintained within ± 2 cm. The water from the reservoir is brought to the channel inlet through a PVC pipe with a 25 mm internal diameter. As the flow is gravity driven, the flow rate can change depending upon the pressure drop in the system. In the present experiments, isolated stripes surrounded by laminar flow are studied. The pressure drop due to an isolated stripe deviates little from laminar flow, and the resulting fluctuations in the pressure drop are small compared to the pressure head available. Therefore we can safely approximate the flow to be with the constant flux. Water is injected in the settling chamber through

4 inlets and is allowed to pass around a plate installed in the front of the four pipe inlets inside the settling chamber preventing turbulent jets from entering the settling chamber and the convergence. A porous sponge is kept in the settling chamber just before the convergence, which breaks the large eddies passing to the channel at the entry. This arrangement maintains laminar flow in the channel up to $Re \approx 1150$. After the flow is passed through the porous sponge, it is accelerated through a convergence of length 100 mm and with the ration of convergence 90:1. For $Re > 1150$, the disturbances from the side walls can trigger turbulence. However, the onset of turbulence is well below this value of Re, and in the range of Re of interest, the flow in the channel remains laminar if not perturbed voluntarily.

A flowmeter is installed between the reservoir and the entrance of the channel. The temperature probe is installed in the settling chamber just upstream of the sponge. The channel is illuminated along both sides with the help of LED lamp-banks installed parallel to the channel axis kept at both sides of the channel 1400 mm above it. Three high frame rate cameras are installed above the channel to capture the evolution of the turbulent structures. The water exits the channel at atmospheric pressure and then recirculated to the reservoir with the help of a submersible pump.

At a distance of 100 mm from the test section entrance, three holes of diameter 0.25 mm each, are drilled in the bottom plate along the spanwise direction. The distance between two adjacent holes is 100 mm, and the central hole among the three lies on the streamwise axis, i.e., the centerline of the channel. These holes are used to inject pressurized water jet in the channel in order to create spot perturbations. Additional methods to generate turbulence in the flow are explained in Section 3.3

3.2 Measurements and instruments

An accurate estimate of the flow velocity and the kinematic viscosity is necessary to estimate Reynolds number (Re) correctly. Flow velocity is determined based on the measured flow-rate and the area of the cross-section of the channel. As the viscosity of water changes with temperature, an accurate value of the fluid temperature is also essential. This section summarizes the instruments used to measure these quantities.

3.2.1 Temperature measurement

The viscosity of water changes with the temperature. The viscosity dependence on the temperature of the working fluid i.e., water, is approximated with the following relation

$$\nu = a + bT + cT^2 + dT^3 \text{ where}$$
$$a = 1.7869 \times 10^{-6}, b = -0.05839 \times 10^{-6}, c = 0.00118 \times 10^{-6} \text{ and } d = -0.00001118 \times 10^{-6} \tag{3.1}$$

This relation is obtained by fitting a cubic curve on kinematic viscosity-temperature data of water from IAPWS 2008 [Cooper and Dooley, 2008]. Temperature is in $^{\circ}C$ and kinematic viscosity is m^2/s. As can be seen from Figure 3.2, this fit is valid in the operational range of temperature i.e.$T \in (18, 26)$.

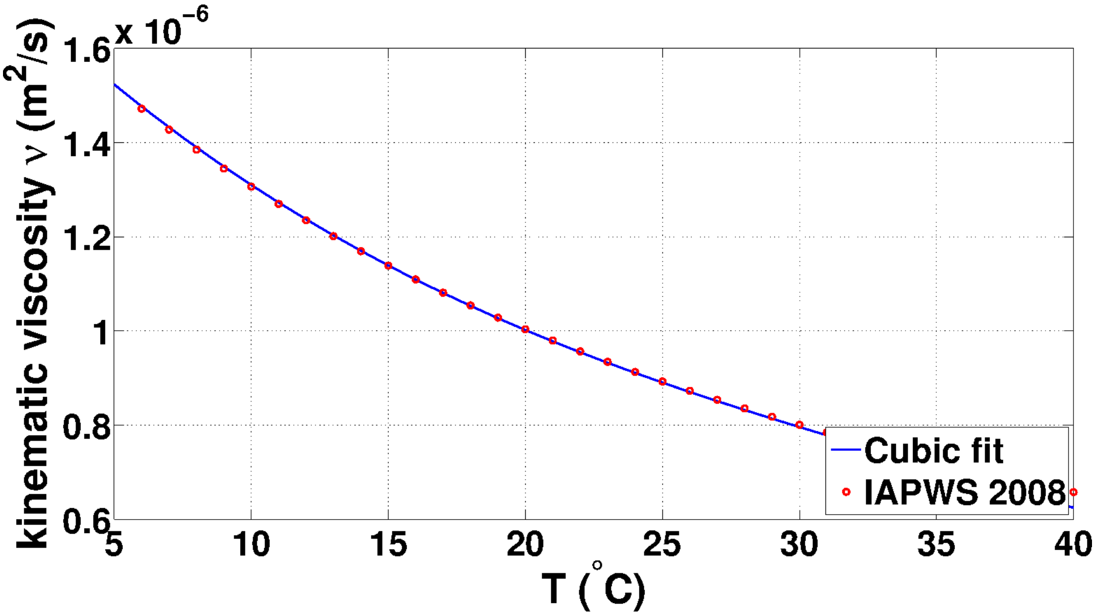

Figure 3.2: Kinematic viscosity of water as a function of temperature. The cubic fit is valid for an operational range of temperature, which is $T \in (18, 26)$.

Therefore to determine Re accurately, it is necessary to have an accurate estimation of the fluid temperature. Temperature is measured with the help of a PT100 probe, which has an accuracy of $\pm 0.5^{\circ}C$. The probe is placed inside the settling chamber just before the convergence, upstream of the sponge. The signal is averaged over a timespan of 2 s.

3.2.2 Flow measurement

Another necessary quantity other than the temperature in estimating Re is the bulk velocity in the channel, which can be deduced from the flow rate. The flow rate is measured with the help of an electromagnetic flowmeter installed before the entrance to the channel. The flowmeter is manufactured by ABB (model FEP311), with the internal diameter $25mm$. The accuracy of the flowmeter is 0.4% of the measured flow rate. The range of the measurement of the flow rate that can be handled with the flowmeter is $4 - 200lpm$. For the experiments, the flow rate range is $Q \in [9, 20]lpm$. The flow rate is estimated by averaging over 2 s of the signal from the flowmeter.

3.2.3 Cameras/Image capturing

The evolution of the flow is captured by three overhead high frame rate cameras (Model:acA2040-180km-Basler ace) placed on the top of the channel at a distance of ~ 165 cm from the channel top. The standard Nikon lens (model AF Nikkor 50mm f/1.8D) is attached to all the three cameras. The three cameras are placed in a line equidistantly. These cameras have a maximum frame rate of 180 fps at 4 MP resolution, and the maximum resolution is 2048×2048 pixels. However, the lower resolution of 512×512 is used in this experiment as it is enough to capture the turbulent fraction of the stripes, and it also makes image processing faster and uses lower storage is 512×512. The images captured are grayscale.

Each camera captures an area $\sim 35cm \times 35cm$. The three cameras are arranged in such a way that the lens axis is vertical, and there is a small overlap of $\sim 1cm$ in the view fields of the neighbouring cameras. The images are stitched together, cropping the overlap and the extra regions, to get the larger frame of the channel. Together, the view fields of the cameras cover an area of ~ 1000 mm $\times 245$ mm of the channel- which translates into lengthscales $2000h \times 490h$.

3.3 Perturbation methods

In plane Poiseuille flow (PPf), for $Re < 5772$, a finite perturbation is needed in order to trigger turbulence. We perturb the flow using two different methods. One is a localized or spot perturbation which is suitable for a higher flow rate ($Re > 900$), and the other method is the extended perturbation, which is suitable at a lower flow rate ($Re < 900$).

3.3.1 Spot perturbation

The spot perturbations are triggered by injecting a jet of water through one of the small tap-holes drilled near the entrance of the channel test section (see Figure 3.3). It is a prevalent method used in experiments to trigger turbulence [Alavyoon *et al.*, 1986; Henningson and Alfredsson, 1987]. Water is kept in a pressurized reservoir connected to the small injection holes of diameter 0.25 mm via a solenoid valve. Pressure in the reservoir is maintained at ~ 8 bar. The flow can be perturbed by opening the valve continuously for $4 - 5$ ms or by firing the valve for 2-3 times in a small time interval of $7 - 8$ ms. When the valve opens, pressurized water from the reservoir is allowed to pass through it, creating localized spot-like perturbations in the laminar flow in the channel. This turbulent spot eventually develops into turbulent stripes. The quantity of water that passes through the valve every time it opens is minimal (< 0.1 ml)compared to the flow rate (~ 0.3 l/s) in the channel. This perturbation method works efficiently for $Re > 900$. However, below that, the method is no more efficient as stripes are rarely formed using spot perturbations as Re reduces.

3.3.2 Extended perturbation

Similar to the pipe flow, the perturbation amplitude necessary to trigger turbulence increases as Re decreases ([Darbyshire and Mullin, 1995]). The spot perturbations are not strong enough to nucleate turbulence at $Re < 900$. Therefore a different method is implemented to perturb the flow. In this method, a small magnetic object such as an iron sphere or a flat small iron piece is permanently kept inside the channel held in a place by an external magnet. Turbulence is triggered by moving this object suddenly in the laminar environment. A sudden motion of the object in the laminar flow creates

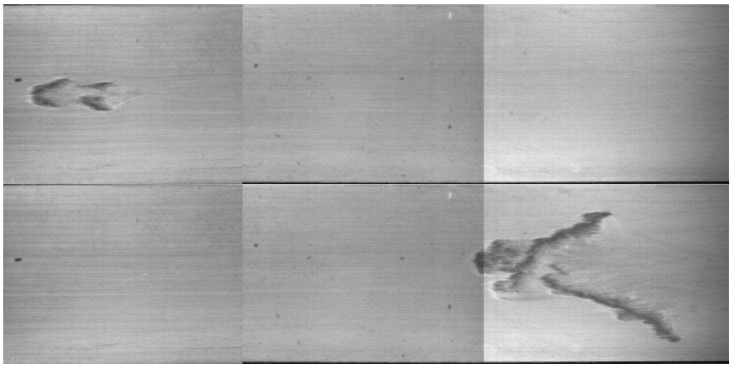

Figure 3.3: Spot perturbation produces a small perturbed nucleus near the channel entrance by injecting pressurized water through the tap holes drilled near the test section entrance. These perturbations evolve further into oblique turbulent stripes. This method is effective for $Re > 900$. (Flow is from the left to the right)

perturbations that have a larger area. These perturbations are powerful enough to trigger turbulence, which evolves further downstream into a turbulent stripe. As the object permanently remains inside the channel, there is a constant wake downstream of this object. However, for $Re < 900$, this wake decays and by itself does not trigger any turbulence.

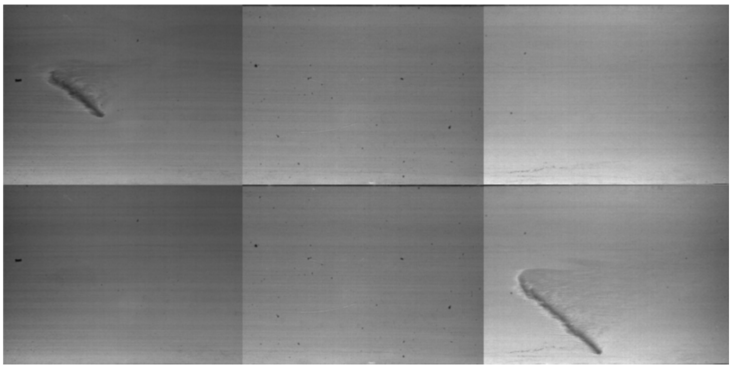

Figure 3.4: Extended perturbation at lower Re is achieved by moving an object placed permanently inside the channel with an external magnet. This method works efficiently in the range of $675 < Re < 900$ as it creates strong perturbations which can trigger turbulence at these Re.

This perturbation method is achieved through an external mechanism, fondly named 'Klitschko'. It consists of a pneumatic cylinder with a three-way valve, supplied with air at a pressure of 9 bar. The magnet is held in the holder attached to the free end of a piston of the pneumatic cylinder. This cylinder is mounted on an aluminium frame such that the cylinder remains horizontal. A padded stopper is placed in front of the cylinder, and it can be adjusted on the aluminium frame such that the stroke of the piston can be changed. The object inside the channel is held at a position with the help of this magnet. When the magnet moves, the object inside the channel follows it.

Care is taken such that the magnet does not have any physical contact with the channel. It is necessary in order to avoid any unnecessary background noise, which may otherwise occur due to the high acceleration and deceleration of the magnet.

In a small range for $900 < Re < 950$, both the perturbation methods -spot perturbation and extended perturbation - can be used. However, above $Re > 950$ extended perturbation becomes impractical as the wake of the object placed inside the channel starts triggering turbulence by itself.

3.3.3 Quenching

For $Re < 675$, it becomes challenging to create strong perturbations, even with the extended perturbation method. To study the dynamics of turbulent stripes at these low Re, an effective generation of the turbulent stripes is necessary. To ensure this, we used the method of quenching. Here, the principle is to create a turbulent stripe using extended perturbation at a Re where the extended perturbation is sufficient, i.e., $Re > 675$, and then subsequently reduce the flow rate to the Re of interest.

In the experimental setup, an arrangement is made such that the water to the channel can be bypassed through a parallel loop fixed with a solenoid valve which is normally closed. For the quenching, this solenoid valve is opened, allowing more water to flow through the channel, increasing the Re. Then the extended perturbation is activated, and a stripe is created. The valve is kept open for some time, allowing the turbulent stripe to evolve at this higher Re over a distance of $1200h$. Then the solenoid valve in the loop is closed, and Re is reduced - or quenched - suddenly. The stripe is allowed to settle at this lower Re for an approximate distance of $800h$ before the readings are taken. To investigate if the results are independent of the method of perturbation, experiments were performed at $Re = 700$, using extended perturbations as well as quenching. The results were not influenced by the use of any of the methods. Therefore, quenching perturbation is used o study turbulence in a range of $Re \in [600, 675]$.

3.4 Flow visualization

This experiment is designed to study the evolution of turbulent structures in the channel. In water, the turbulent structures or patterns are not visible to the naked eye. Therefore, flow visualization is necessary in order to observe these structures as they advect and evolve downstream. For the flow visualization, water in the channel is seeded with the synthetic mica particles. They are not spherical in shape but flat/ellipsoidal. These particles are coated with TiO_2, which can reflect incident light specularly. Though they are little heavier than water, because of the high velocities ($0.6m/s$), they remain in the channel for a very short time. It reduces the possibility of the particles settling in the channel. Instead, they follow the flow well enough, allowing us to visualize the turbulent patterns in the flow. We used synthetic mica particles (Eckart SYMIC C001) with diameter ($10\mu m - 40\mu m$).

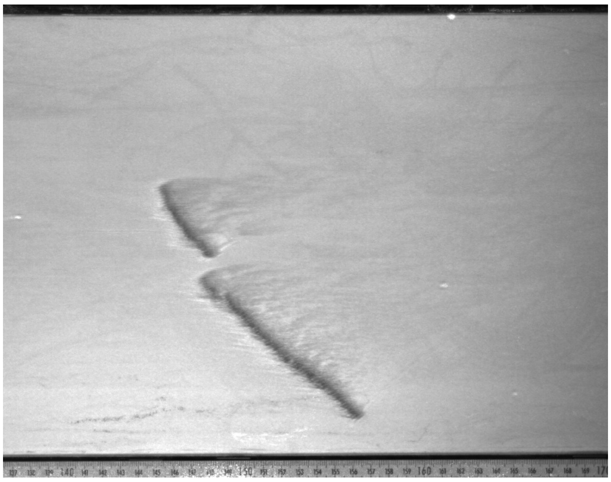

Figure 3.5: A turbulent stripe at $Re = 675$. The stripe is surrounded by bright laminar flow, and dark patches mark the turbulent region of the stripe. This difference is visible because of the difference in the reflected light intensities of the mica particles in the laminar and turbulent regions.

When the particles are in the laminar region, they align with the flow in the direction of the shear. Whereas in the non-laminar regions, on the other hand, the particles follow the eddies and their orientation changes continuously. Therefore these two regions show a difference in the intensity of the reflected light. The channel is illuminated with the LED banks installed on both sides of the channel parallel to the channel axis at the height of $140cm$ from the channel top. The LED banks are tilted at $60°$ with the vertical axis. With this arrangement, the region with laminar flow looks bright, and a darker region marks the turbulent patch. Figure 3.5 shows a turbulent stripe at $Re = 675$. The dark regions represent a turbulent stripe, and the brighter region represents the laminar flow surrounding the turbulent stripe.

This visualization technique does not provide information about the 3D velocity field but only a projection of turbulent structure on $(x - z)$ plane where x and z are along streamwise and spanwise direction respectively. However, for this experiment, information on turbulent fraction and general shape of the turbulent structures are adequate.

3.5 Image processing

In this experiment, the turbulent structures are recorded in the form of images captured by overhead cameras. The information about the turbulent structures like the length of the stripes, their orientation with respect to the mean flow direction, turbulent fraction, i.e., the area occupied by the turbulent structures are extracted from the images. A MATLAB code is developed using the inbuilt image processing toolbox in order to process these images. In the following, the algorithm for image processing is summarized. To estimate the area and length of the turbulent stripe in the image, it is necessary to process the images in order to detect the edges between the regions of different intensities (i.e., laminar and turbulent regimes).

1. Background images are captured at the start of the experiment before taking the readings at each Re. These background images are the images of the fully laminar velocity field.

2. The three cameras provide three images at each instant. Therefore all the images are cropped and stitched together to have a full view of the flowfield.

3. Non-uniformities in the image result from the illumination gradient due to the lighting arrangements. This non-uniformity can be removed either by subtracting the grayscale values of the background image from the image to be processed or by dividing the grayscale values of the image of interest with the background image.

The background image also has identical non-uniformity as this image is captured with identical illumination settings. Here we remove the non-uniformities by dividing the grayscale values of the image with the background image.

4. After removing the non-uniformities, the high-frequency noise in the image is filtered using 2D adaptive noise filter known as Wiener filter, using 5×5 masking. This smoothing operation helps in distinguishing whole turbulent stripe from laminar flow.

5. Further sharpening of the edges of the laminar-turbulent interface in the smoothed image is done using “unsharp masking”. In this technique, the image is sharpened by subtracting blurred -“unsharpen” version of the image from itself. It, in turn, sharpens the edges between the laminar-turbulent interface in the image. These parameters are chosen by trial and error so that they are robust for all the images captured in the experiment.

6. Now the image is converted to a binary image with a threshold. In the binary image, laminar flow is represented by 0, and the turbulent region is marked by 1.

7. The connected domains are then identified from the binary image by identifying continuous clusters of the binary values. Each connected domain is treated as a single stripe. This is important in evaluating the evolution of the length and the area of the turbulent stripe.

This image -processing algorithm is robust for different threshold values used for different image-processing techniques used. The information extracted from the processed images is listed in the following section.

3.6 Inferred quantities

The following information can be extracted from the processed images.

Length of a stripe The length of a stripe is determined by estimating a curve-length along a turbulent stripe. From a processed image, many points at inside a stripe are identified with equidistant z coordinate (along spanwise direction). Connecting these points, in turn, gives curve-length of the stripe

Turbulent fraction One way of estimating turbulent fraction is to compute the exact area of the turbulent region from the pixels in the turbulent region. The other way with which turbulent fraction can be approximated is by multiplying stripe curve-length by its thickness. We choose the latter because - as will be discussed later - it is observed that the stripe thickness remains almost the same for the range of Re of our interest. Therefore, the estimation of the curve length is representative of the turbulent fraction.

Angle of the stripe An isolated turbulent stripe is reasonably straight barring the region near the tail. The angle of the stripe is defined as the angle made by this straight part of the stripe with the mean flow i.e., the streamwise direction. Therefore, fitting a straight line on the stripe-barring the near-tail region - on the processed image gives the angle of the stripe

Velocity of the stripe Information such as bulk velocity/centerline velocity of the laminar flow at particular Re, the frame rate of the cameras used is coupled with the location of the stripe in the successive images to estimate the normalized velocity of the stripe. The velocity of the tip and the tail of the stripe is estimated by identifying the location of the tip and the tail in successive images. Difference between the locations and information about the time gap between two images give the absolute velocity of the tip and the tail in the streamwise and the spanwise direction. The advective time units are defined as $t^{*} = h/U_{cl}$. The stripe velocities are computed with respect to the advective time units.

3.7 Experimental procedure

The Re of interest is obtained by adjusting the flow rate, taking into account the temperature and depending upon the Reynolds number suitable perturbation method is chosen. In either of the perturbation methods, an isolated individual stripe is generated near the entrance of the test section at a location $\approx 300h$ from the inlet. The stripe then travels downstream, and once it enters the view field of the overhead cameras, the cameras are triggered. The turbulent stripes advect in the streamwise as well as in the spanwise direction. When the stripe touches the side-wall of the channel, it decays at once. Therefore, it is necessary to take the readings of the stripe when it is not touching the side-walls. Once the stripe leaves the channel completely, the next stripe is generated.

The location where the entire stripe arrives in the view field is little more than $2000h$ from the inlet. Therefore, the stripe evolves for a considerable amount of time before the readings are taken. As mentioned earlier, the combined view field of the overhead cameras is $2000h$ in the streamwise direction. Therefore the evolution of the individual stripe can observed over this entire length. For every stripe, 25 images are taken capturing its evolution from one end of the view field to the other end.

At each Re evolution of at least 1200 stripes is recorded. For Re near the critical point, the number of stripes recorded is even more. All the reported quantities of interest such as growth rate, tip and tail velocities, natural angle of the stripes etc. are measured and averaged over thousands of stripes.

While performing the experiments, the temperature is monitored continuously. The flow rate is regularly adjusted to have a constant value of Re to nullify the changes in Re due to temperature fluctuations. In every run, Re was maintained within ± 10 of the desired value. The range of Re over which readings are taken is $[600, 950]$ in a step of 25.

3.8 Results

This work aims to study the behaviour of turbulent stripes near the onset of turbulence and to estimate a critical point above which turbulence can sustain indefinitely. We investigate a mechanism with which turbulence proliferates near onset. In order to do so, we estimate the mean growth rate of individual stripes and its relation with Re. Then we examine the significance of the splitting and the decay of individual stripes and its effect on the sustenance of turbulence. We also report here a natural angle of the stripes with respect to the streamwise direction and how it changes with Re.

3.8.1 Angle of the stripes

It is observed that the isolated individual stripes grow at a preferred angle with respect to the mean flow direction depending on Re. When a stripe is created, as it advects downstream, it settles to a particular angle. This angle changes with Re. We, henceforth refer it as a “natural angle” of the stripes at a particular Re. In other words, when the stripe is allowed to evolve naturally, it settles down to the orientation equal to its natural angle as $t \to \infty$. In this experiment, the channel is long enough to allow the stripe to adjust to the natural angle well before it is advected in the view field of the overhead cameras. Usually, it is observed that the natural angle at any Re has a spread but a definite mean.

At higher Re, for e.g. $Re = 950$, the natural angle of the stripe with the streamwise direction is $\approx 30^\circ$. But as Re decreases this angle increases and for $Re < 850$ the natural angle approaches 45°.

Interestingly the natural angle never exceeds around 45° at any value of Re. It can be noted that a natural angle of the turbulent stripes at the onset of turbulence is 45°.

3.8.2 Turbulence near onset

Near onset, the turbulent bands are isolated and are tilted with respect to the streamwise direction. When the laminar flow is perturbed, the disturbance eventually grows into an oblique stripe, as shown in Figure 3.10. A turbulent stripe is composed of many

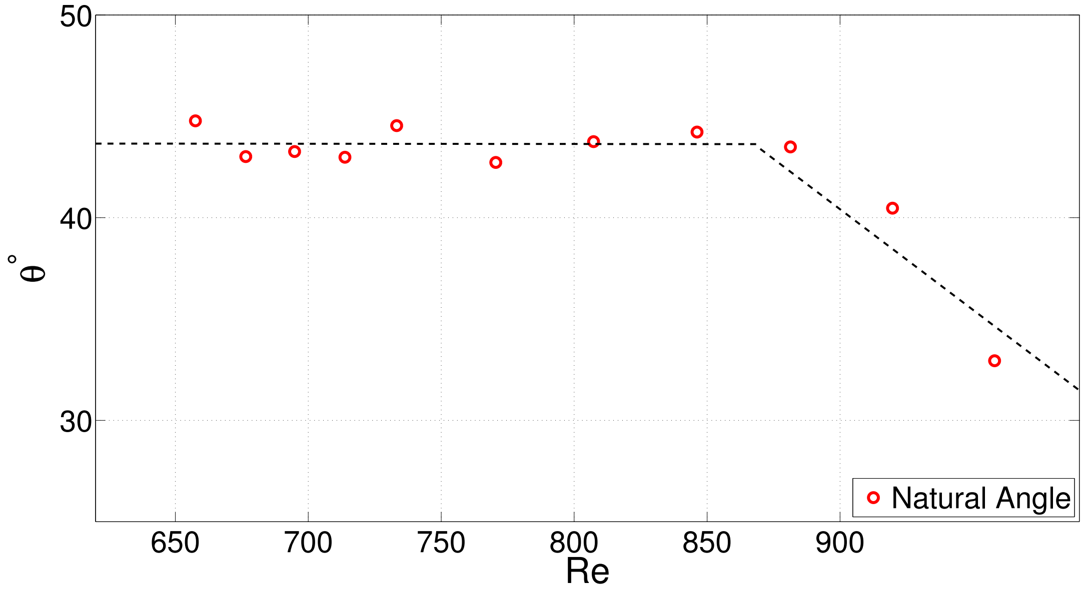

Figure 3.6: Angle made by the stripes with respect to the mean flow direction as a function of Re. At higher Re, the stripes make a narrow-angle with respect to the mean flow direction. As Re reduces, the natural angle approaches $45°$.

quasi-streamwise streaks and vortices or rolls. The downstream tip of the stripe is characterized by wedge-shaped oblique streaks (Figure 3.7). There is a continuous addition of new streaks from the "tip" of the stripe by which the stripe grows. This process of streak addition is shown in Figure 3.8. At the downstream end i.e., the "tail" of the stripe, the patches of streaks are shed intermittently. These patches, when get disconnected from the stripe, generally tend to decay.

As the stripe advects downstream, the combined effect of the addition of new streaks from the tip and decay from the tail results in translation of the stripe in the spanwise direction. The length of an individual stripe is determined by the balance between growth at the tip and decay at the tail.

When the decay at the tail is more than the streak addition from the tip, the stripe shrinks as it travels downstream before the ultimate collapse. The decay process is shown in Figure 3.9. The stripe at $Re = 640$ advects in the streamwise as well as the spanwise direction. It continuously sheds streaky patches from the tail at a rate higher than the tip growth. Therefore the length of the stripe reduces as the stripe travels downstream as can be seen from the middle panel of the figure and then the whole stripe disintegrates and collapses eventually, as shown in the last panel.

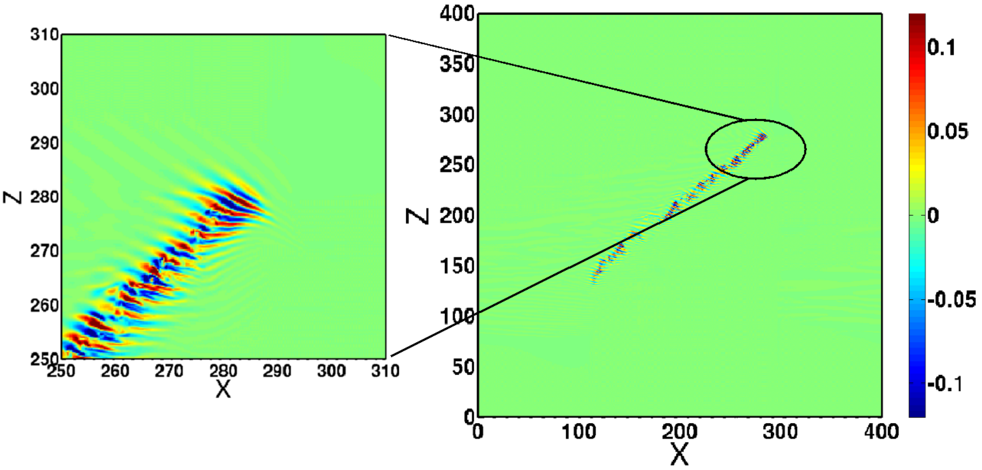

Figure 3.7: Turbulent stripes in numerical simulations at $Re = 660$ with wall-normal component of fluctuation velocity in a domain size $(L_x, L_y, L_z) = (400, 2, 400)$. The stripe is composed of quasi-streamwise streaks and vortices. The flow is from the left to the right.

When the tip growth rate is more than that of the tail decay, the stripe grows as it is advected downstream. Figure 3.10 demonstrates a growing stripe at $Re = 675$. The leftmost panel is where the stripe first arrives in the view field of the overhead cameras. The length of the stripe increases as it moves further downstream as can be seen in the successive panels.

In addition to the balance between the tip growth and tail decay, another mechanism that plays an important role in the proliferation of turbulence near onset is the “splitting” of stripes. As discussed earlier, the streaky patches are shed from the tail and generally decay once they are separated from the parent stripe. However, sometimes, when the shed patch is strong enough, it may create another stripe. This nucleation of turbulent stripe does not always succeed, and the patch decays without creating a new stripe. However, when the nucleation is successful, a new stripe starts growing upstream of the parent stripe. Figure 3.11a shows an unsuccessful splitting attempt at $Re = 825$. The streaky patch (circled in red colour) after getting detached from the parent stripe fails to nucleate a new stripe and decays eventually. The successful attempt to nucleate a new stripe and a consequent increment in the turbulent fraction by “splitting” can be seen in Figure 3.11b. Here a stripe at $Re = 880$ sheds a streaky patch- marked by a red circle- which nucleates a new stripe which starts growing upstream of the parent

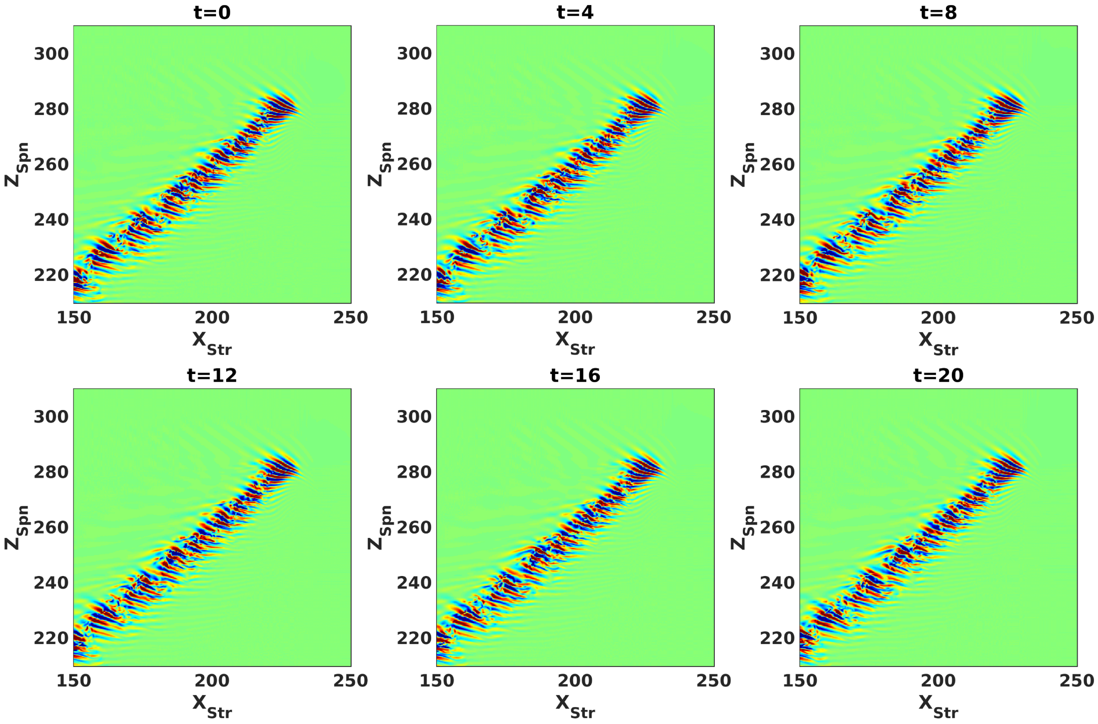

Figure 3.8: Continuous addition of streaks at the tip of the stripe. The figure shows snapshots of an isolated stripe at $Re = 660$ in time. It can be seen that at the tip of the stripe, the streaks are added continuously. The snapshots are taken in the comoving frame of the tip and contain the wall-normal velocity component at the plane $y = 0$. The flow is from the left to the right.

stripe.

Another mechanism in addition to the stripe growth and splitting is “branching”. In branching - like splitting - a new stripe is nucleated from a shed patch of vortices. However, unlike splitting, the new stripe is formed in the opposite orientation of the parent stripe. The angle of the new stripe with the mean flow direction is the same ($\pm\theta$) as that of the parent stripe, but the orientation is different ($\mp\theta$). Therefore, this mechanism is responsible for forming criss-cross turbulent stripe patterns in the flow. Figure 3.12 shows a branching event (marked by a red circle) at $Re = 1050$ of a stripe generated by the spot perturbation. The spot evolves into two stripes oriented to the streamwise direction in symmetrically opposite fashion and as the stripe advect downstream, new stripes “branch out” from the parent stripe in the symmetrically opposite direction that of the parent stripe.

As will be demonstrated later, at the onset of sustained turbulence, the two rel-

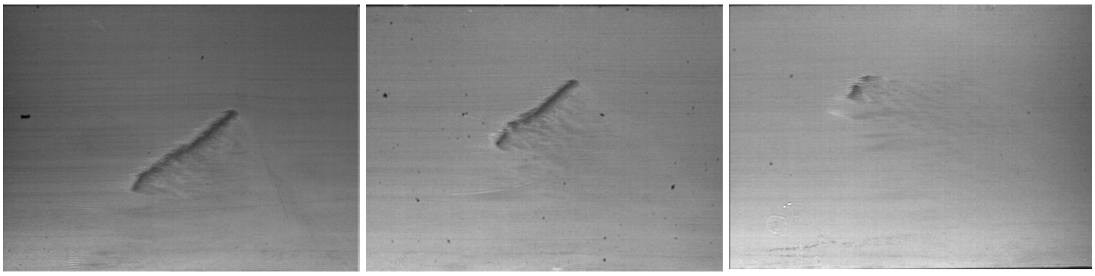

Figure 3.9: Decaying turbulent stripe at $Re = 640$. The stripe grows at the downstream tip by adding new streaks and decays from the upstream tail by shedding streaks. When the shedding rate at the tail is higher than the addition of new streaks from the tip, then the result is an eventual decay of the stripe. The flow is from the left to the right.

Figure 3.10: Growing turbulent stripe at $Re = 675$. When a continuous addition of new streaks at the downstream tip is more than an intermittent streak decay at the upstream tail, the stripe length increases in an average sense as it is advected in the streamwise and spanwise direction. The flow is from left to right.

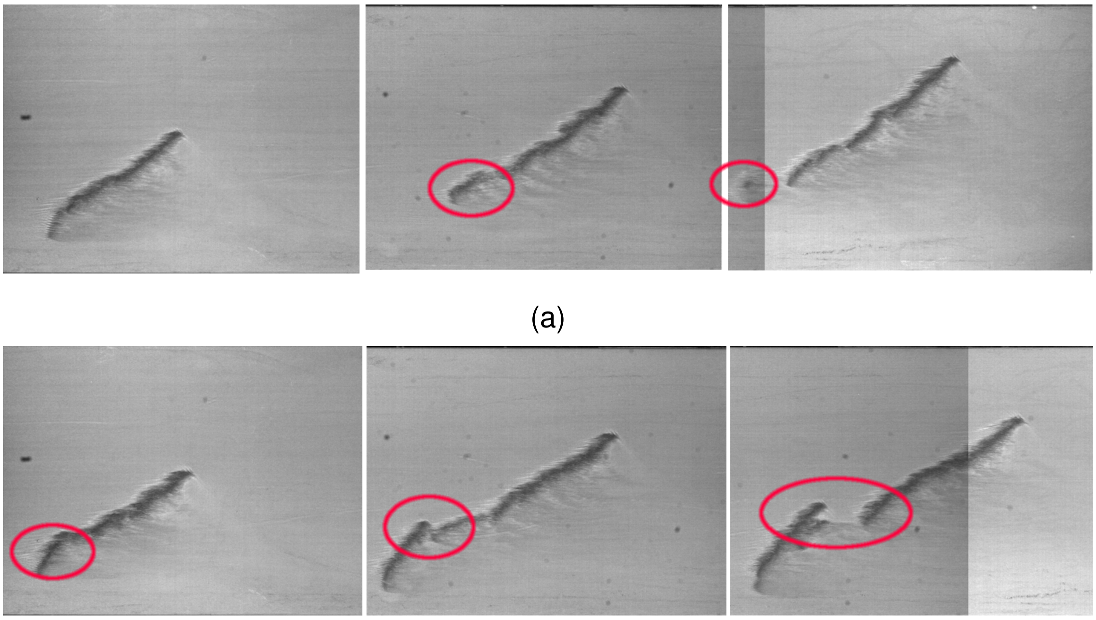

(a)

(b)

Figure 3.11: Stripe splitting. (a)Unsuccessful splitting of the stripe at $Re = 825$. The streaky patch gets separated from the tail. However, as it advects downstream, the streaky patch decays as it is not strong enough to regenerate a new stripe upstream of the parent stripe. The decaying patch has been marked by a red circle. The flow is from left to right. (b) A successful splitting of the stripe at $Re = 880$. Here, the separated turbulent patch from the tail is strong enough to create a new stripe upstream of the parent stripe. The red circle denotes the evolution of the streaky patch as it moves downstream. The flow is from left to right.

evant mechanisms are stripe growth and splitting. The probability of experiencing a branching event near the critical point is practically zero. In these experiments, we did not observe any branching event around the critical point. Therefore, the mechanisms which are relevant near the critical point are stripe extension, splitting, and stripe decay.

3.8.3 Mean growth rate

The turbulent fraction is determined by computing the area of the stripe from the image. At each Re, we take an ensemble average of turbulent fraction and compute the mean turbulent fraction as a function of time. The rate of change of averaged turbulent fraction in time gives a mean growth rate at a particular Re. The mean growth rate of

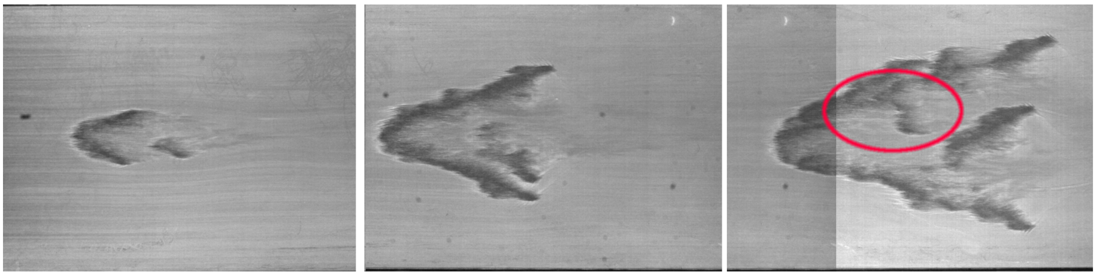

Figure 3.12: Branching event at $Re = 1050$. In branching, a new stripe is formed from a parent stripe and grows at a tilt angle the same as the parent stripe but in the opposite orientation. The flow is from the left to the right

a turbulent fraction of individual stripes with Re is shown in Figure 3.13. For $Re < 650$, the mean growth rate is negative i.e., the turbulent fraction shrinks below this Re. For $Re \approx 650$ the mean growth rate becomes positive and then for $Re > 670$ the mean growth rate increases almost linearly with Re. It indicates that the turbulence is sustained at $Re > 650$. Therefore, we propose that $Re \approx 650$ is the critical point of the channel flow above which turbulence sustains indefinitely

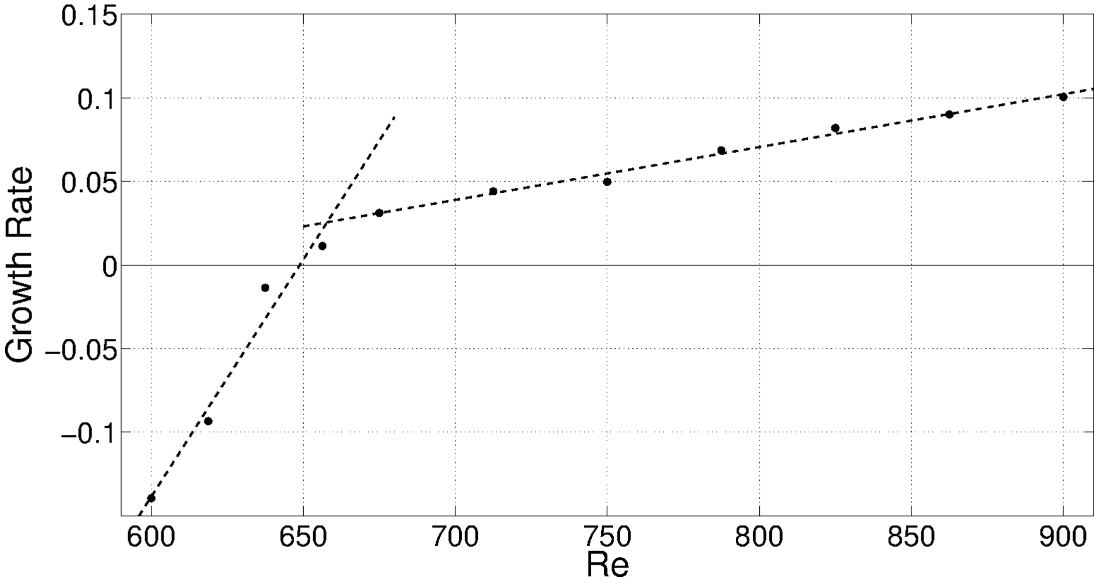

Figure 3.13: The mean growth rate of the individual stripes as a function of Re. The mean growth rate is zero at $Re \approx 650$, and increases linearly with Re for $Re > 670$.

In the subsequent sections, we further investigate the mechanisms behind the growth and decay of the turbulence around the critical point.

3.8.4 Extension of an individual turbulent stripe

As discussed earlier, the turbulent stripe is advected downstream with the mean flow. In addition, the growth due to continuous addition of the streaks at the tip and the intermittent shedding of the streaky patches from the tail result in the translation of the stripe in the spanwise direction as well. The advection velocity of the turbulent stripes, normalized with the centerline velocity of the laminar flow in the streamwise direction is shown in Figure 3.14. The stripes advect almost at the same velocity $0.7U_{cl}$ for all Re. The advection velocity is slightly higher than the mean or bulk velocity, which is $2U_{cl}/3$.

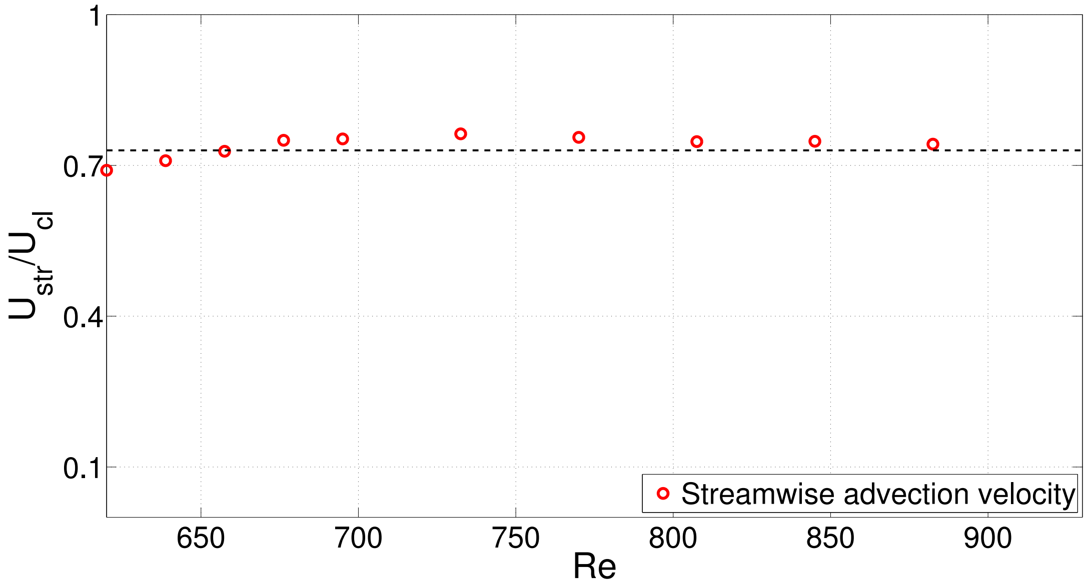

Figure 3.14: The advection velocity of the turbulent stripes along the streamwise direction as a function of Re. The whole stripe travels in the streamwise direction with a velocity slightly larger than the mean flow.

For any individual stripe, the advection velocity along the streamwise direction is the same for the whole stripe -from tip to tail. This is the reason that once the stripe settles to its natural angle, it does not change as it advects downstream. The change in the length of the stripe results from a difference between the spanwise advection of the tip and the tail, which itself is attributed to the respective growth and decay processes.

It is observed that the velocity of the stripe tip is constant for a particular Re because the addition of the new streaks at the tip of the stripe is at a constant rate. Similar to the stripes in PCf [Duguet *et al.*, 2011], when the stripe advects downstream, the tip velocity along the spanwise direction is constant. However, for an individual stripe, there is a lot of variation in the tail velocity along the spanwise direction due to a regular but random shedding of the streaks.

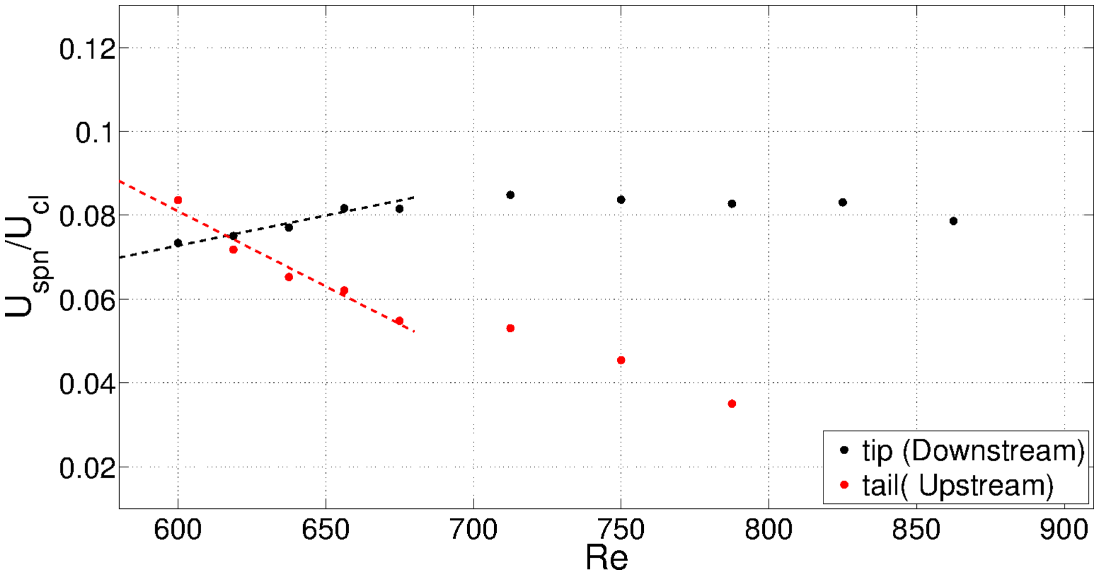

Figure 3.15: The spanwise velocity of the tip (red dots) and the tail (black dot) - normalized with the centerline velocity of the laminar parabolic profile with the same mass flux - as a function of Re. When normalized, the velocity of advection along the streamwise direction does not change with Re, and the stripes travel at a slightly higher velocity than the bulk velocity.

As can be seen in Figure 3.15, the tip velocity in the spanwise direction (marked in red) increases significantly with increasing Re until $Re \approx 660$ and then more or less remains constant. However, the tail velocity in the spanwise direction decreases monotonically with increasing Re. Below $Re < 620$ the mean tail velocity is more than the mean tip velocity and the competition between the tail shedding and tip growth below $Re < 620$ results in shrinking of the individual stripes. The tip growth and tail decay process balance each other at $Re \approx 620$.

3.8.5 Mechanism behind turbulence proliferation

As stated earlier, the decay from the tail is due to the regular but intermittent shedding, unlike the tip growth, which is a continuous process. Though the stripe extension through the tip growth-tail decay balance at $Re = 620$, the separated patches of the streaks from the tail fail to nucleate new stripes below $Re < 650$ and consequently, a successful splitting event is very rare at $Re < 650$. Only when $Re > 650$, we observed that the streaky patches separated from the tail are strong enough to nucleate a new stripe upstream of the parent stripe, and both the stripes grow independent to each other as they travel downstream. Splitting is responsible for the proliferation of turbulence in planar directions. In addition to the growth of a single stripe, splitting causes multiplication in the number of the stripes.

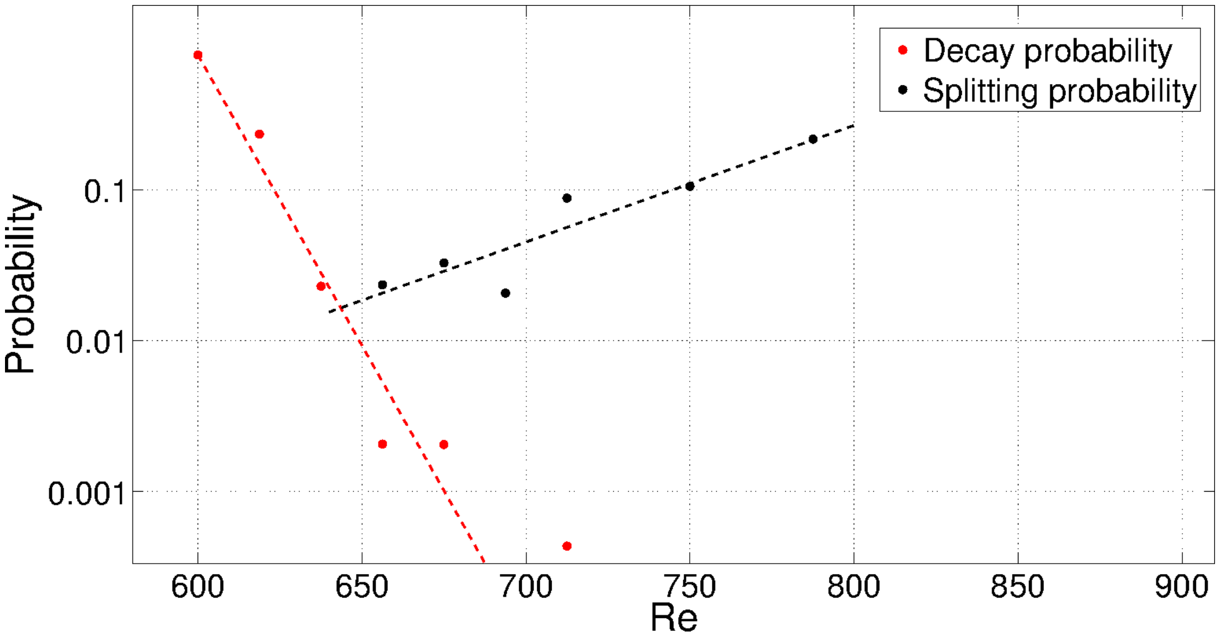

Figure 3.16: Probability of decay and splitting as a function of Re. Probability of stripe decay drops as Re increases (black), whereas, probability of successful splitting increases with Re (red). Splitting and decay balance each other at $Re \approx 650$.

The probability of the splitting increases with Re as shown in Figure 3.16 marked by red dots. This probability is estimated by observing the number of stripes which show successful splitting within the observation window. The black dots, additionally, show the probability of the stripes decaying completely. For $Re < 600$, all the stripes decay within the channel with decay probability 1. However, as Re increases, the probability of decay reduces. At $Re = 650$, only 2.5% of the total number of the investigated stripes decay before they leave the observation window. The decay and splitting probability balance at $Re \approx 650$. As Re increases further, the splitting probability becomes much higher than the decay probability.

We further studied the splitting and decay processes closely. At $Re = 618$, the mean growth rate is negative, and stripes shrink as they travel downstream before collapsing. At this Re, almost all the stripes decay before leaving the channel. It is observed that most of the stripes decay in the downstream half of the channel. We plotted the survival probability as a function of time of the stripes at $Re = 618$ at different streamwise location (i.e. at different advective time units) in Figure 3.17. All the stripes considered here have an initial length of $\sim 230h$. Once the stripes shrink to a length of $\sim 120h$, 90% of the stripes decay in the next 500 advective time units.

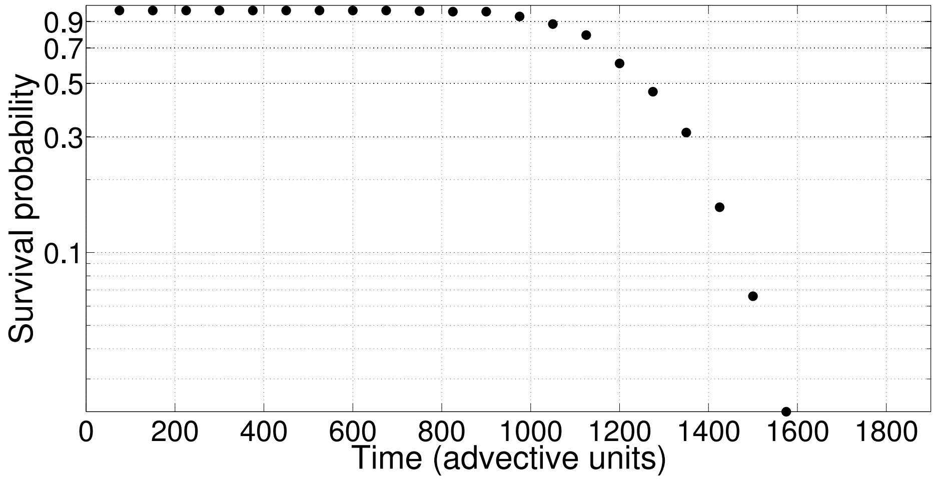

Figure 3.17: Survival probability of stripes at $Re = 618$ at different advective time units. Until ~ 670 advective time units, very few stripes decay showing higher survival probability. However, as stripes shrink, the decay probability also increases. The decay probability is coupled with the stripe length. For the shorter stripes, the chance of decaying is much more than that of longer stripes.

Interestingly, the decay probabilities do not fall exponentially with advective time, contrary to the puffs in pipe flow [Avila *et al.*, 2011]. The decay rate is not constant and increases with advective time as the stripes shrink. It suggests that the decay rate depends upon the length of the stripes.

Figure 3.18 shows the distribution of the stripe lengths at the moment of decay (left

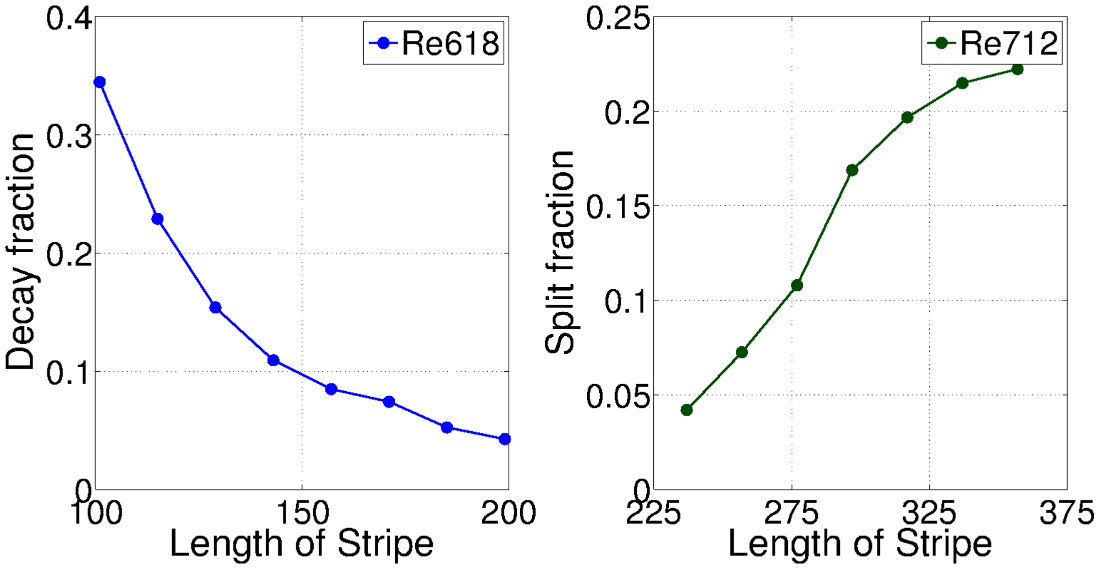

Figure 3.18: Dependence of stripe survival and decay on stripe length. The left panel consists of a distribution of the lengths of the stripes at $Re = 618$ at the moment of decay. Shorter stripes tend to decay more than the longer stripes. The right panel, on the other hand, shows the distribution of the length of stripes at the moment of successful splitting at $Re = 712$. Longer stripes tend to split more compared to the shorter stripes.

panel) at $Re = 618$. Stripes with small lengths tend to decay more. Hence, it can be concluded that the probability of decay is inversely proportional to the stripe length. In plane Couette simulations [Shi *et al.*, 2013] where the stripe length is fixed because of the periodic boundary conditions, the decay probabilities fall exponentially. However, in reality, the stripes are fully localized and grow or shrink, resulting in variability of the length. We, therefore, propose that the stripe lifetimes are memoryless only for the stripes with a fixed length. However, for naturally expanding/shrinking stripes, the decay of a stripe as a whole is not memoryless and the stripes age.

Also, in the same figure (Figure 3.18), the distribution of the stripe length at the successful splitting is shown (right panel). As stripe length extends more, the probability of the stripe splitting also increases. The dependence of the splitting and decay probabilities on the stripe length couples them to the growth rate i.e., stripe expansion rate.

Therefore, stripe expansion/shrinking is the crucial mechanism that governs splitting and decay of the stripes, which in turn plays a vital role in sustaining turbulence in the channel. Splitting can take place only when the stripes are expanding. If the stripe is shrinking, the detachment from the tail results in the relaminarization of the flow.

At the onset of the splitting ($Re \approx 650$), the turbulence expands by stripe expansion and also by creating new stripes upstream of the parent stripe through splitting. In effect, the turbulence proliferates in the two dimensions, one of the dimensions being the direction of stripe expansion.

We further studied the final collapse of the stripes. A typical behaviour of a decaying individual stripe at $Re = 618$ (Figure 3.19) gives an insight in to the decay process. The initial length of the stripe is $200h$, and it shrinks because of the competition between tip growth and tail decay until the length becomes $120h$ (marked by a red trend line). After $120h$, the rate of decay increases suddenly (marked with blue line). This behaviour has been observed over 1000 shrinking and then decaying stripes. The faster decay rate of the stripe below $120h$, which leads to the final collapse of the stripe, is due to the uniform disintegration of the stripe. Thus the stripe decay as a whole is composed of two processes viz. shrinking and stripe collapse.

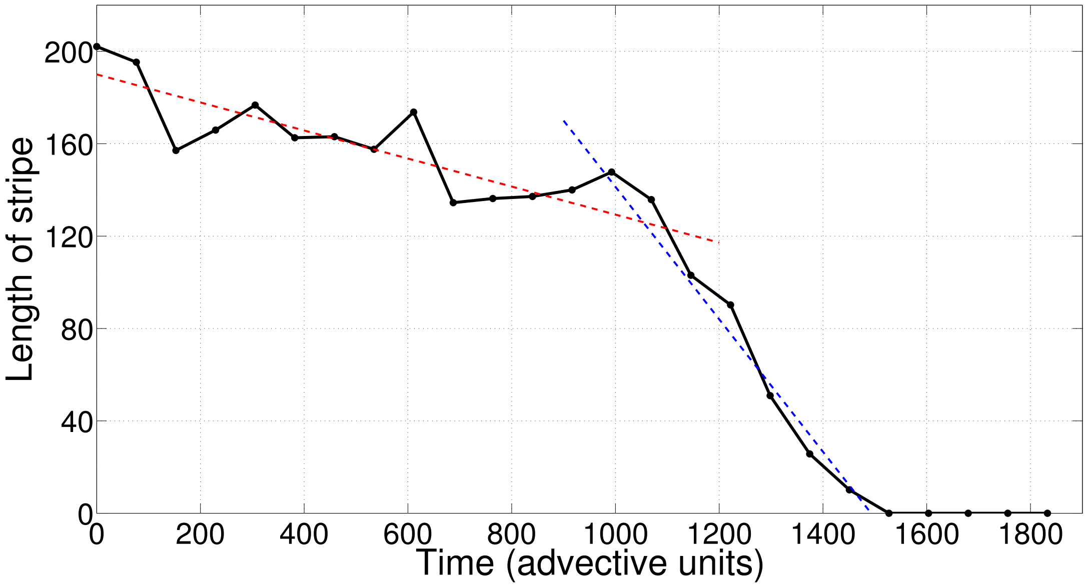

Figure 3.19: Evolution of a length of an individual stripe at $Re = 618$. This stripe travels downstream shrinks initially because of tip growth-tail decay competition (red). Then once the stripe shrinks below $120h$, the rate of decay increases suddenly. This increase in the decay rate is due to the uniform disintegration of the stripe (black).

This final stripe collapse is studied by plotting the survival probabilities of the stripes with an initial length of $120h$. Only the stripes which are intact at this length are considered for the readings. It can be seen that until 400 advective time units, almost all the stripes survive. However, interestingly after that, the survival probability diminishes exponentially. It means that for the short stripes, the memoryless behavior of the decay is recovered. This is an additional observation regarding the stripe decay process. Similar observations about the memoryless collapse of the stripe are reported in a numerical study of PCf by Manneville [Manneville, 2011].

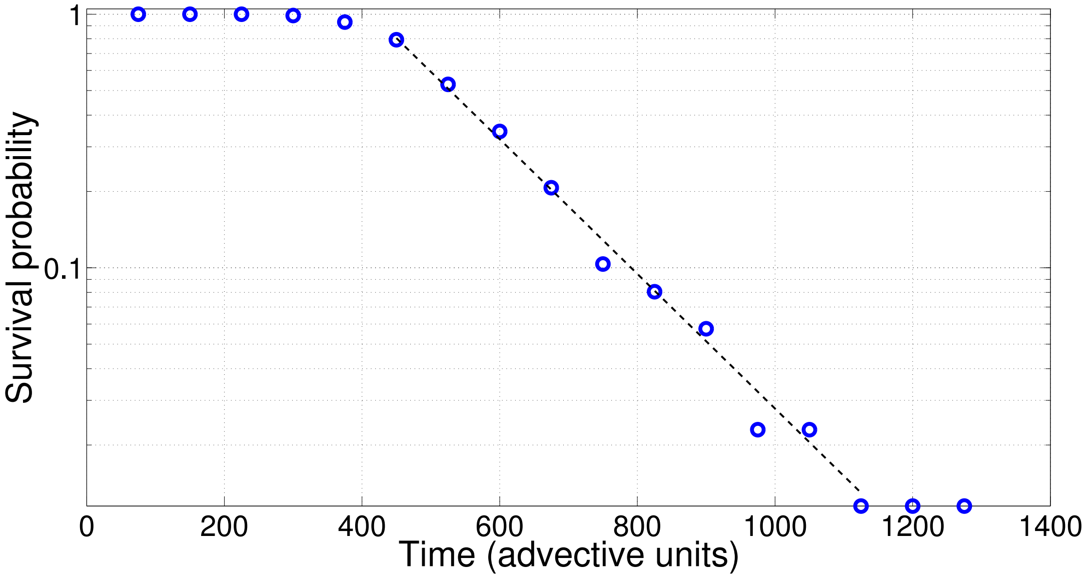

Figure 3.20: Survival probabilities of shorter stripes ($\sim 120h$) at $Re = 618$. The stripe survival probability is very high until ~ 400 advective time units. However, after that, the survival probability decreases exponentially. It represents the stripe collapse, and it can be argued that the stripe collapse is a memoryless process.

3.9 Summary

The experiments in the channel flow are carried out in the largest aspect ratio channel constructed to the knowledge of this author. Near the onset, turbulence manifests in the form of oblique stripes. At the critical point, the angle made by the stripes with respect to the mean flow direction is $\sim 45°$. As Re increases, the angle becomes smaller.

The mean growth rate of a turbulent fraction with Re suggests that the critical point above which turbulence is sustained in channel flow is $Re \approx 650$. Unlike pipe flow -

where the decay and growth processes are independent - in PPf, all these processes are coupled.

The key mechanism with which an individual stripe changes its length, as it travels downstream, is the competition between the tip growth due to streak addition at the downstream end and shedding of the streaky patches from the upstream tail. These processes balance each other at $Re \approx 620$ and for $Re > 620$ the stripes start expanding. In this experiment, the first successful splitting event is observed little above the onset of stripe expansion i.e., at $Re > 650$. At this Re, the splittings and the decays are balanced. Both the splitting and the decay are coupled with the length of the stripe, and a successful splitting can occur only when the stripes are expanding. Also, the splitting probability increases with the length of the stripes. On the other hand, stripes with shorter length tend to decay/collapse more than the longer stripes. The splitting is responsible for the multiplication of the stripes as successful splitting creates new stripe downstream of the parent stripe and results in proliferation of turbulence in the channel flow in two planar dimensions.

The branching mechanism is significant in at Re much higher than the critical. Near the critical point branching events are infrequent, and in these experiments, no branching event was recorded around the critical Re. However, at higher Re branching becomes frequent and is the responsible mechanism for the criss-cross patterns observed at $Re > 950$. This mechanism has a more significant growth rate and thus much faster than the slower stripe expansion and thus can be detected easily in the shorter experiments. In current experiments, we did not study branching in detail.

Finally, we denote that this study is not adequate to comment on any universality class of the transition. However, it is to be noted that none of the mechanisms violate the conditions stated by directed percolation conjecture by Grassberger-Janssen [Grassberger, 1982; Janssen, 1981]. We show that the transition to the absorbing state (laminar state) is expected at the critical point identified here and future study about the transition should target the regime $Re = 650 \pm 15$.

4 Bifurcations of turbulent stripes in plane Poiseuille flow

As stated earlier, a variety of shear flows like pipe flow (HPf), plane Couette flow (PCf), plane Poiseuille flow (PPf) become turbulent despite the laminar base flow being linearly stable. The base laminar flow in PCf [Drazin and Reid, 2004] and in pipe flow [Meseguer and Trefethen, 2003] are linearly stable for all Re. But in PCf, turbulence occurs in the form of oblique stripes at $Re \sim 325$ [Dauchot and Daviaud, 1995; Prigent, 2001] and in pipe flow turbulence is observed in the form of localized patches called puffs even at $Re \approx 2000$ [Wygnanski and Champagne, 1973; Avila *et al.*, 2011]. Similarly,in PPf, though the base laminar flow becomes unstable to infinitesimal perturbations at $Re = 5772$ [Orszag, 1971], as shown in Chapter 3, turbulence exists at Re much below than this limit [Carlson *et al.*, 1982; Nishioka and Asai, 1985; Alavyoon *et al.*, 1986; Lemoult *et al.*, 2013]. This suggests that this subcritical transition to turbulence is independent of the linear stability properties of the base laminar flow, and the turbulent structures have a nonlinear origin [Waleffe, 2001; Waleffe, 2003; Wedin and Kerswell, 2004; Kerswell, 2005; Eckhardt *et al.*, 2007].

Laminar plane Poiseuille flow becomes unstable to Tollmien-Schlischting waves at $Re = 5772$. Historically, the investigation started with the possibility of bifurcation of the base laminar flow to these two-dimensional Tollmien-Schlichting (TS) waves and then later to the three-dimensional waves [Stuart, 1960]. It was discovered [Ehrenstein and Koch, 1991] that the first bifurcation towards the TS waves is subcritical, but the bifurcation branch fails to reach the values Re as low as those observed in early transition experiments [Carlson *et al.*, 1982; Nishioka and Asai, 1985; Alavyoon *et al.*, 1986]. Also, importantly, the TS waves are composed of spanwise oriented vortices, and the coherent structures observed near the transitional regime are composed of streamwise streaks and vortices (Figure 4.1). Therefore TS waves bear little resemblance with the

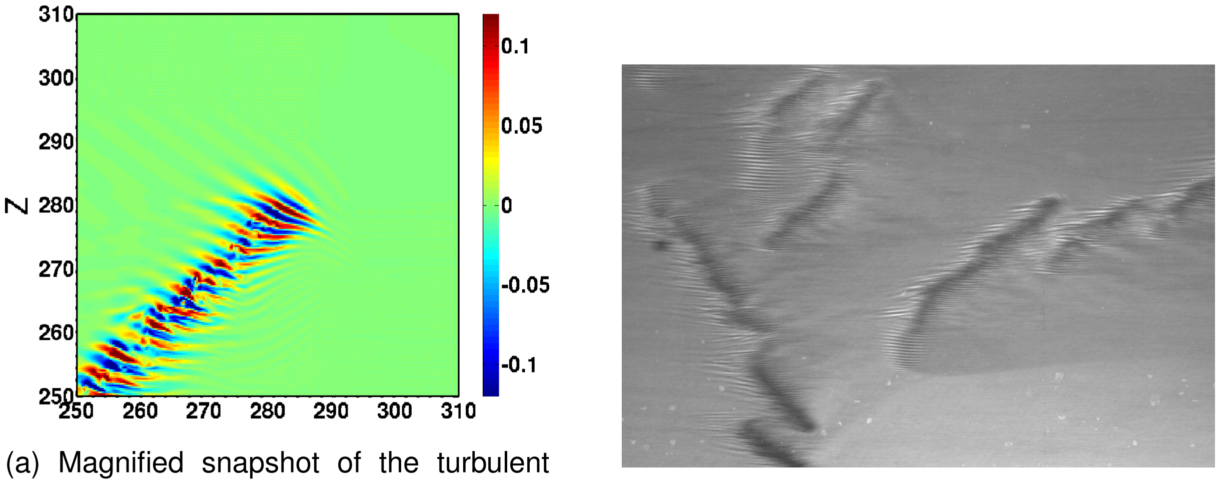

(a) Magnified snapshot of the turbulent stripe at $Re = 660$ from a numerical simulation in a domain size 400×400. The velocity field plot consists of a wall-normal component v. The turbulent stripe in its core is composed of quasi-streamwise streaks and vortices.

(b) Turbulent stripes from experiments at $Re = 750$. The experiments are carried out in a channel of size $4000h \times 2h \times 490h$. The flow is from left to right. The stripes are oblique to the streamwise direction.

Figure 4.1: Turbulent stripes

turbulent structures at onset.

The studies of the self-sustaining process at low Re in small periodic domains [Hamilton *et al.*, 1995] suggested that the alternative solutions of Navier-Stokes equations should exist at Re near the onset of turbulence, which are more relevant to the transition process. These solutions appear in a saddle-node bifurcation at some finite Re. They are generally expected to be linearly unstable and disconnected from the base laminar profile. The idea is that turbulence occurs through a sequence of bifurcations of these invariant solutions.

Many such solutions have been found in PPf in minimal flow units (MFU) [Jiménez and Moin, 1991; Waleffe, 2001; Nagata and Deguchi, 2013; Wall and Nagata, 2016; Park and Graham, 2015; Neelavara *et al.*, 2017]. However, the solutions found in MFU are spatially periodic and lack key features of turbulent structures observed in experiments near the onset of turbulence such as localization and obliqueness. In the latter case, turbulence takes the form of localized stripes surrounded by laminar flow and oblique to the mean flow direction as has been shown in a variety of experimental studies [Hashimoto *et al.*, 2009] and simulations in large domains [Tsukahara *et al.*, 2005; Xiong *et al.*, 2015; Tao *et al.*, 2018]. The turbulent stripes first appear to form close to regular patterns, and with decreasing Re, they become more and more isolated (see Figure 5.2 in the subsequent chapter) [Xiong *et al.*, 2015; Tao *et al.*, 2018]. This property is apparently common to most wall-bounded shear flows near the onset (in Re) of apparition of non-trivial fluid motion, including plane Couette flow [Prigent *et al.*, 2002], rotor-stator flow [Cros and Le Gal, 2002], counter-rotating Taylor-Couette flow [Coles, 1965], annular pipes [Ishida *et al.*, 2016], etc.

Another peculiar fact about PPf is that the turbulent stripes at the onset can take multiple orientations similar to PCf [Prigent, 2001; Barkley and Tuckerman, 2007]. As has been shown in Figure 3.6, the stripes have a distinct preferred orientation with respect to the mean flow direction at each Re. As Re reduces the angle of the stripes with respect to the mean flow direction increases first, and then asymptotically goes to $45°$. Therefore, a relevant bifurcation scenario explaining the appearance and sustenance of such oblique turbulence structures should rely on nonlinear solutions satisfying several conditions so far never fulfilled together :

1. spatial localization
2. obliqueness of the interface consistent with the experimental range of angles [Duguet and Schlatter, 2013]
3. presence of quasi-streamwise vortices and streaks [Bottin *et al.*, 1998a].
4. Consistency of the range of existence of the solutions in Re with the range in Re where turbulence exists in the form of tilted stripes.

In the following, we demonstrate numerically the existence of unstable traveling waves satisfying the above properties, the emergence of these traveling waves at various tilt angles θ and the routes to chaos starting from these traveling wave solution branches.

4.1 Numerical set-up

The simulations are carried out in a doubly periodic rectangular domain tilted with respect to the mean flow direction using *Code-2*.

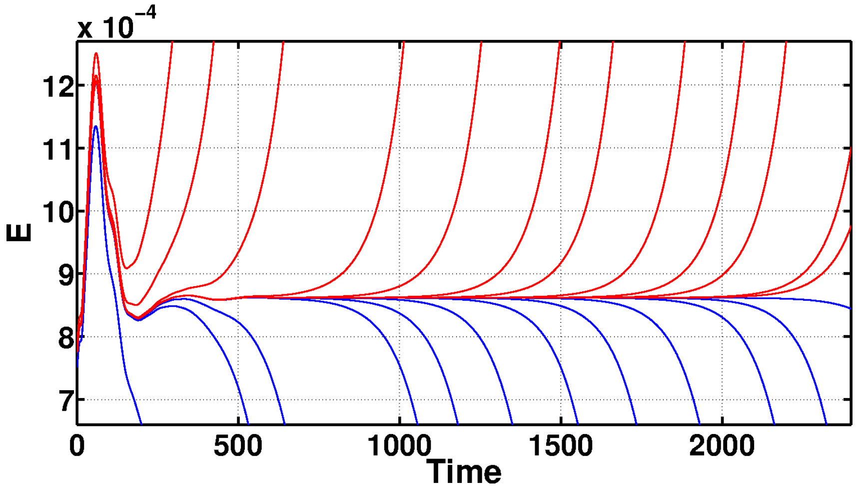

Figure 4.2: Edge tracking at $Re = 720$ at the tilt angle $\theta = 35°$ in a domain of size $(L_x, L_y, L_z) = (10, 2, 40)$. The trajectories marked in red visit the turbulent attractor, and the blue trajectories directly go to the laminar fixed point. However, as the trajectories - obtained by the bisection method - approach the edge state, the kinetic energy of the fluctuations settle down to a constant value. It is the signature of a traveling wave solution.

The domain size was chosen as $(L_x, L_y, L_z) = (10, 2, 40)$ where L_x and L_z are the lengths of the domain in periodic directions x and z respectively. L_y is the distance between the walls of the domain. The resolution used is $(N_x, N_y, N_z) = (72, 49, 256)$. A first attempt to identify the invariant solutions is carried out at $Re = 720$ at a tilt angle $35°$ using the bisection method starting from a random divergence-free velocity field as an initial condition. After a few iterations, it was noticed that the perturbation kinetic energy $E(t)$ settles to a constant value free from any temporal fluctuations as shown in Figure 4.2.

This is the signature of a traveling wave solution. This solution is then converged further using the Newton method (see Figure 4.3a). This traveling wave solution is localized in z and is periodic in x. The TW consists of three identical pairs of slow and fast quasi-streamwise streaks (red and blue) arranged alternately along x. This solution shows structural similarities with an oblique localized turbulent stripe with quasi-streamwise streaks and vortices arranged alternately (Figure 4.1). Unlike the previous studies about the bifurcation scenarios [Avila *et al.*, 2013; Zammert and Eckhardt, 2015; Kreilos and Eckhardt, 2012] the simulations are carried out in a full space i.e., without imposing any symmetry constraints on the numerical domain other than periodic boundary conditions in x and z and tilt angle θ i.e., the angle made by the smaller side (x) of the domain with the mean flow direction. However, it was observed that, even when no such symmetry was imposed externally, the converged TWs show shift in x and reflect in y symmetry S_{rx}, where

$$S_{rx} : [u, v, w](x + \frac{L_x}{2}, y, z) \rightarrow [u, -v, w](x, -y, z) \tag{4.1}$$

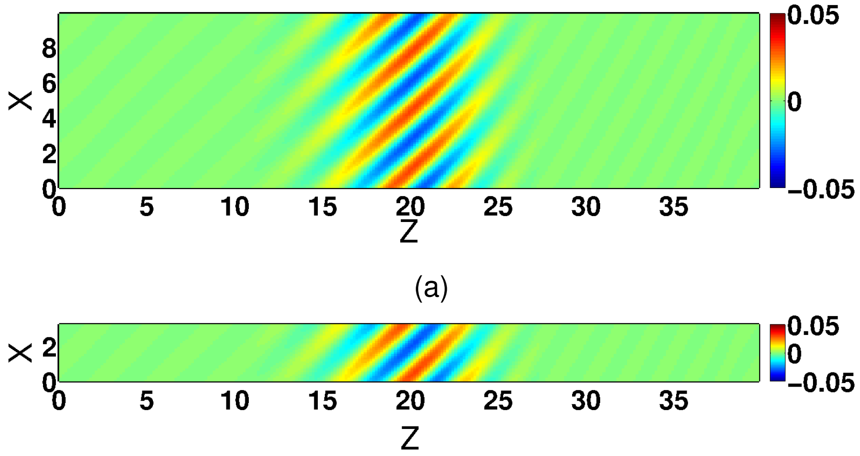

(a)

(b)

Figure 4.3: Lower branch TW solution at $Re = 720$ at $\theta = 35°$ in two domains with domain dimension along the stripe L_X and $L_x/3$. (a)Edge state which is a traveling wave solution in domain size $(L_x, L_y, L_z) = (10, 2, 40)$. This Newton converged lower branch solution has only one unstable eigenvalue. This localized solution features three identical wavelengths in x comprising of alternate slow and fast quasi-streamwise streaks. (b) Edge state which is a traveling wave solution in domain size $(L_x, L_y, L_z) = (3.333, 2, 40)$ at the same tilt angle of $\theta = 35°$. This solution also has only one unstable eigenvalue. This localized solution has only one wavelength in x, which is structurally identical with a wavelength in the bigger domain.

The three pairs of high and low speed streaks suggest that a similar TW solution should exist in a numerical domain with $L_x = L_x/3$ and correspondingly $N_x = N_x/3$. Therefore, the domain size is reduced by a factor 3 in the x direction. Thus the new domain size then becomes $(L_x, L_y, L_z) = (3.33, 2, 40)$ with the resolution $(N_x, N_y, N_z) = (24, 49, 256)$. Again edge tracking has been carried out in this smaller domain. Indeed the invariant solution or the edge state obtained at $Re = 720$ for this smaller domain is the same as the TW solution in the bigger domain and contains only one wavelength in x instead of three (Figure 4.3b. This TW also shows S_{rx} i.e., shift in x and reflect in y symmetry. The reduction in the domain size reduces computational costs and avoids subharmonic instabilities, which may arise in larger domains.

The edge states have been determined through bisection method for different values of $L_x \in \{6.66, 13.33\}$ fixing $L_z = 40$. The invariant solutions in the corresponding domains belong to the same family of TW solutions and only differ in the number of wavelengths in x with two high speed-low speed streaks pairs in $L_x = 6.66$ and four in $L_x = 13.33$. Examining the stability of all the solutions by the Arnoldi method show only one unstable direction. This confirms that these solutions are edge states for the corresponding domain sizes at $Re = 720$ and tilt angle $\theta = 35°$. Therefore, in the following study, we fixed the domain size to
$(L_x, L_y, L_z) = (3.33, 2, 40)$.

The governing equations, defined in an unbounded domain, are equivariant with respect to the two discrete symmetries

$$S_y : [u', v, w'](x', y, z') \rightarrow [u', -v, w'](x', -y, z') \tag{4.2}$$

$$S'_z : [u', v, w'](x', y, z') \rightarrow [u', v, -w'](x', y, -z') \tag{4.3}$$

It is to be noted that by virtue of the S'_z symmetry, a twin TW solution should exist in a domain tilted with angle $-\theta$ and its spanwise propagation velocity should also be opposite.

As discussed in Chapter 2, fixing the tilt angle also fixes the angle of the stripe with the mean flow direction, which is equal to the domain tilt angle. This fact allows us to study bifurcation scenarios for the stripes with different orientations with respect to the mean flow direction.

4.2 Spatial localization in L_z

Experiments show that at Re as low as 700 the turbulent stripes are *isolated* in space. The solutions relevant to this regime of turbulence should also show this property. In order to examine the localization properties of the invariant solutions, the edge tracking through bisections is repeated for the different values of $L_z \in \{20, 40, 80, 120\}$ while keeping $L_x = 3.33$. The numerical resolution was kept identical in x and y except in the z direction. Here the integer value N_z was kept proportional to L_z which can be any real number. The Re is kept at 720, and the domain is tilted with respect to the mean flow direction at an angle $\theta = 35°$. In all the cases, the bisection gives TW solutions that belong to the same family as shown in Figure 4.4 (In the figure, for the sake of representation twelve domains are stacked on top of each other in x). They are localized in z and extended in x. All of these similar TW solutions are composed of alternate low and high-speed quasi-streamwise streaks.

These solutions are then converged using Newton iterations (see Section 2.8), and the stability of these solutions is determined using the Arnoldi method. Figure 4.5 shows the Floquet multipliers computed for all the above TW solutions. As can be seen, only one Floquet multiplier for each TW solution has a value greater than unity, i.e., the TW solutions are linearly unstable with one unstable direction.

The localization of the TW solutions is evident from Figure 4.6. It shows the z-dependence of the perturbation kinetic energy $e_v(z)$ for all the domains. As the domain size increases, $e_v(z)$ drops exponentially confirming the spatial localization of the TW solutions in z. It suggests that the corresponding TW for $L_z \to \infty$ exists and is a spatially isolated state. In what follows, the value of L_z is frozen to 40.

These invariant solutions fulfill the conditions outlined above in agreement with the experimental observations.

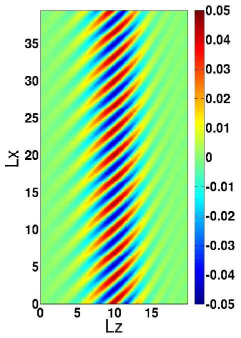

(a) $(L_x, L_y, L_z) = (3.33, 2, 20)$

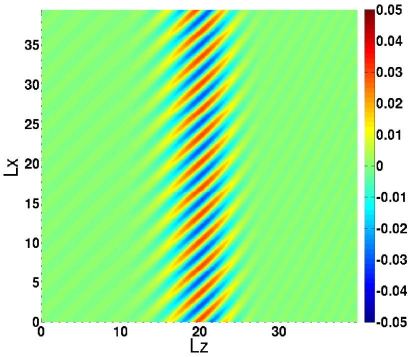

(b) $(L_x, L_y, L_z) = (3.33, 2, 40)$

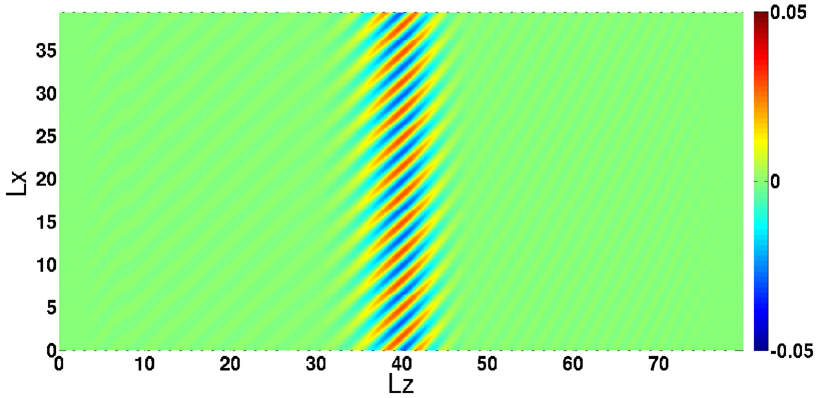

(c) $(L_x, L_y, L_z) = (3.33, 2, 80)$

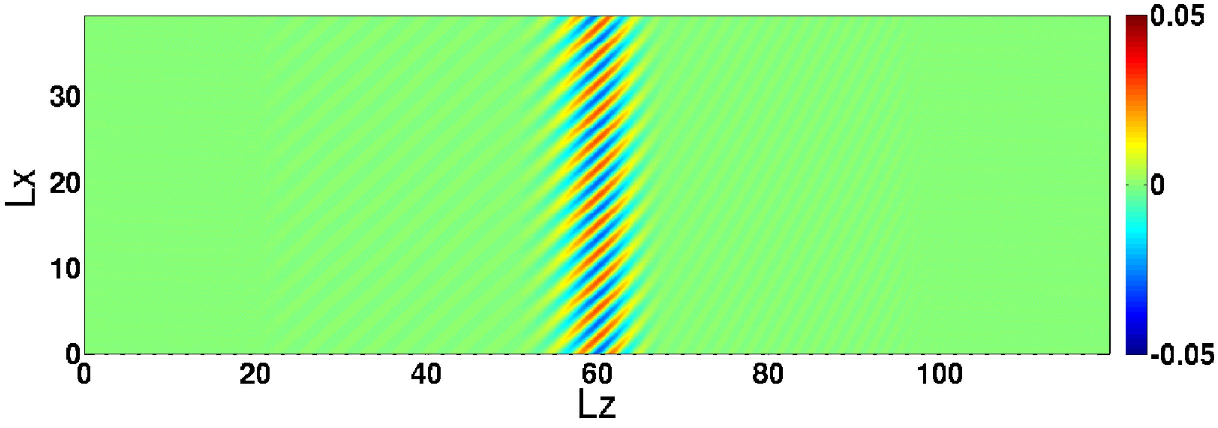

(d) $(L_x, L_y, L_z) = (3.33, 2, 120)$

Figure 4.4: Newton converged TW solutions at $Re = 720$ for domains of different L_z with fixed $L_x = 3.33$ tilted at an angle $\theta = 35°$ with respect to the mean flow direction. These solutions are linearly unstable with only one unstable direction and therefore qualify as edge states for corresponding domains. For the visualization purpose, the representation consists of domains stacked on top of each other nine times in x in order to make their oblique structure clearer.

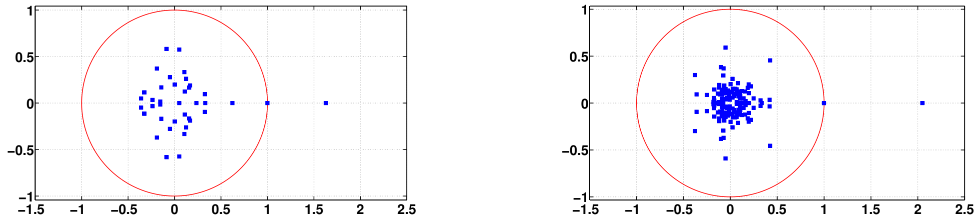

(a) $L_z = 20$ (b) $L_z = 40$

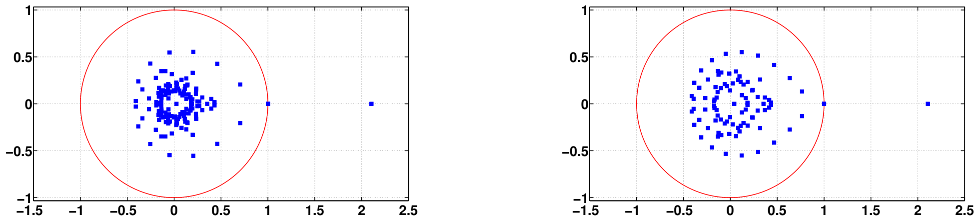

(c) $L_z = 80$ (d) $L_z = 120$

Figure 4.5: Floquet multipliers for TW solutions in the domain with $Lx = 3.33$ and different L_z. For all the solutions, there is only one unstable direction making each of these solutions an edge state for the corresponding domain size.

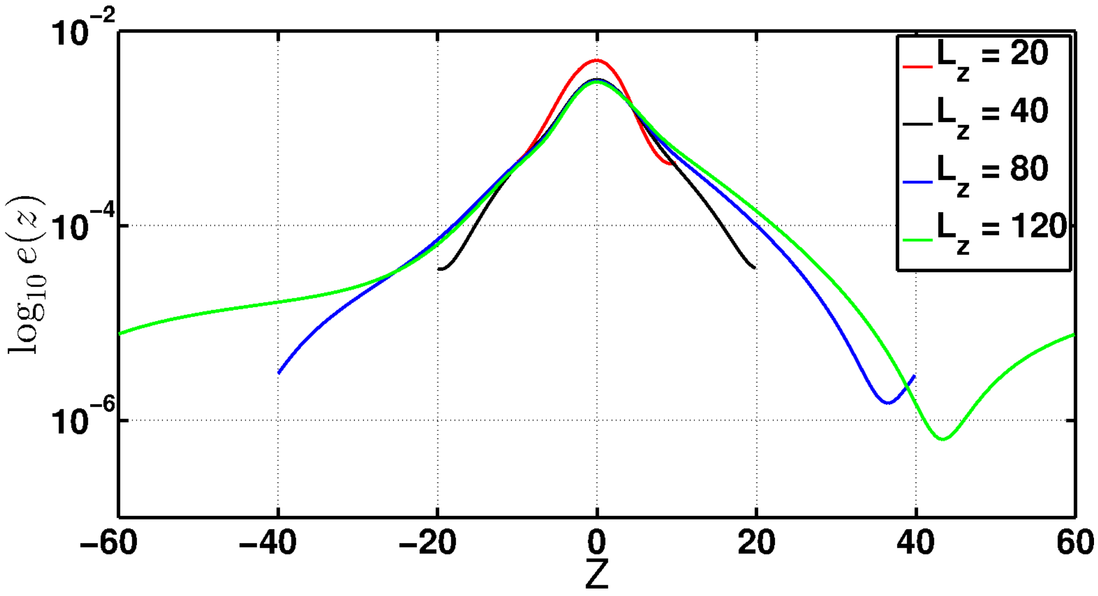

Figure 4.6: Independence on Lz. The perturbation kinetic energy averaged over x, and y is plotted as a function of z. As L_z increases, the tails of the curve show exponential decay. This confirms the spatial localization of these TW solutions. It means a spatially isolated TW solution exists even when $L_z \to \infty$.

4.3 Solutions at different tilt angles

In PPf, stripes occur with a multitude of orientations depending upon the Reynolds number (Figure 3.6). A search for the invariant solutions at different angles is carried out in a range $0^\circ < \theta < 90^\circ$ in a step of 5° in a domain $(L_x, L_y, L_z) = (3.33, 2, 40)$. The value of Re chosen is again 720, as turbulent stripes are easily observable in the experiments at this value. The bisection successfully identified the invariant solutions only for $25^\circ \leqslant \theta \leqslant 60^\circ$. For all these tilt angles, where the bisection was successful, the invariant solutions at $Re = 720$ are found to be TWs and belong to the same family.

As can be seen from the velocity fields in Figure 4.7, the TW stripe thickness changes with the tilt angle θ. An estimate of the stripe thickness can be obtained from the wall normal component of the perturbation kinetic energy $e_v(z)$ as shown in Figure 4.8a), where

$$e_v(z) = \frac{1}{L_x L_y} \int_{-1}^{1} \left(\int_{0}^{L_x} v^2 dx \right) dy \tag{4.4}$$

Interestingly, the wall normal energy E_v of the TW solutions monotonically increases with θ. But in a range $\theta \in (25^\circ, 45^\circ)$ its rate of change with θ is much smaller than for $\theta \in (45^\circ, 60^\circ)$. However, $max(e_v(z))$ has a clear minimum between $\theta \in (40^\circ, 45^\circ)$. Looking at Figure 4.8a, it is clear that the spread of $e_v(z)$ is narrower at $\theta = 25^\circ$ and gradually becomes wider as θ increases and $max(e_v(z))$ decreases at the same time . For $\theta > 45^\circ$ the spread continues to widen and $max(e_v(z))$ increases again. The thickness of the solutions is estimated by choosing a cutoff of $e_v(z) = 0.0001$. As shown in Figure 4.9 the thickness of the LBTW stripe solution is minimum at $\theta = 25^\circ$ and then increases monotonically with θ .

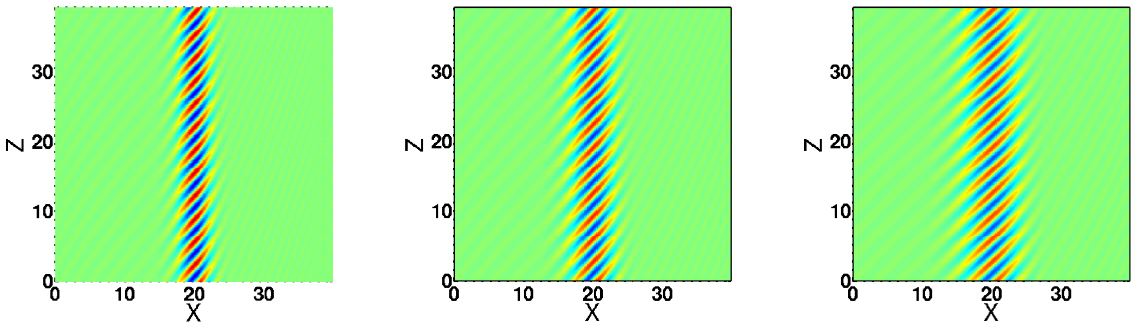

(a) $\theta = 25^\circ$

(b) $\theta = 30^\circ$

(c) $\theta = 35^\circ$

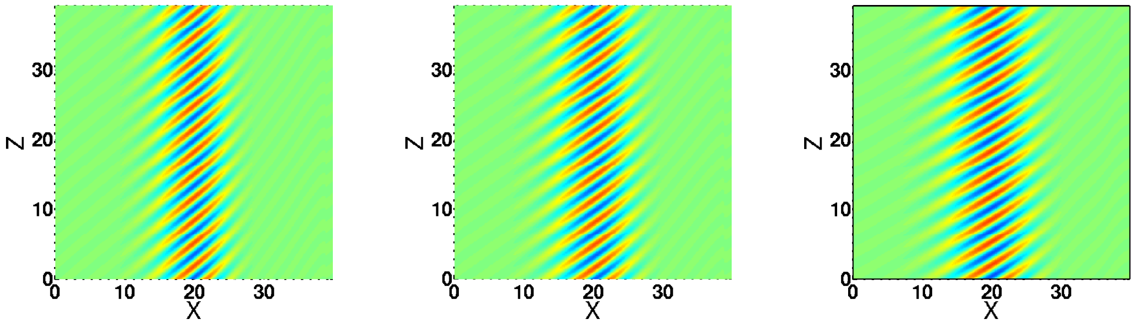

(d) $\theta = 40^\circ$

(e) $\theta = 45^\circ$

(f) $\theta = 50^\circ$

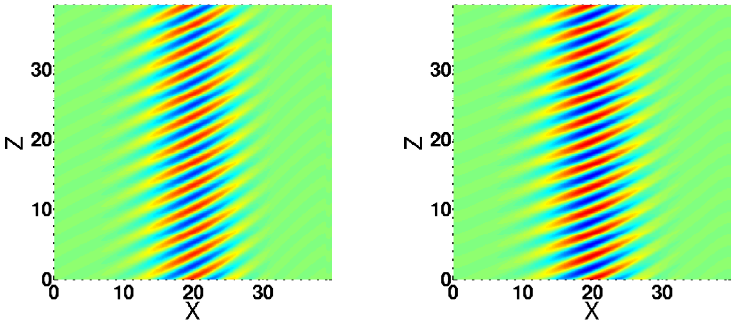

(g) $\theta = 55^\circ$

(h) $\theta = 60^\circ$

Figure 4.7: Newton converged lower branch traveling wave solutions at $Re = 720$ for different θ obtained through the bisection method. These solutions are localized in z and are extended in x. All the solutions contain the stripe composed of alternate slow and fast quasi-streamwise streaks which is also a defining feature of the turbulent stripes in PPf. Here also ,for the demonstration purpose, the flow fields are plotted by stacking 12 copies of a domain $(L_x, L_y, L_z) = (3.33, 2, 40)$ along x.

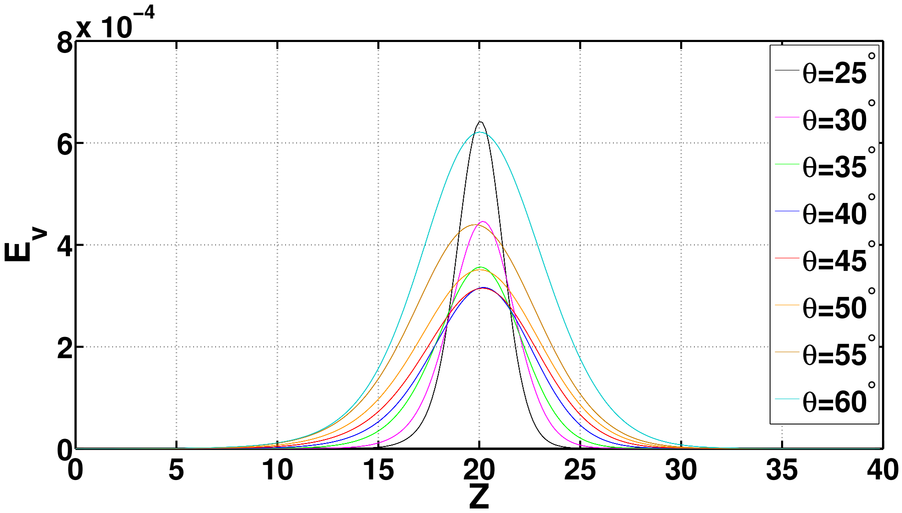

(a)

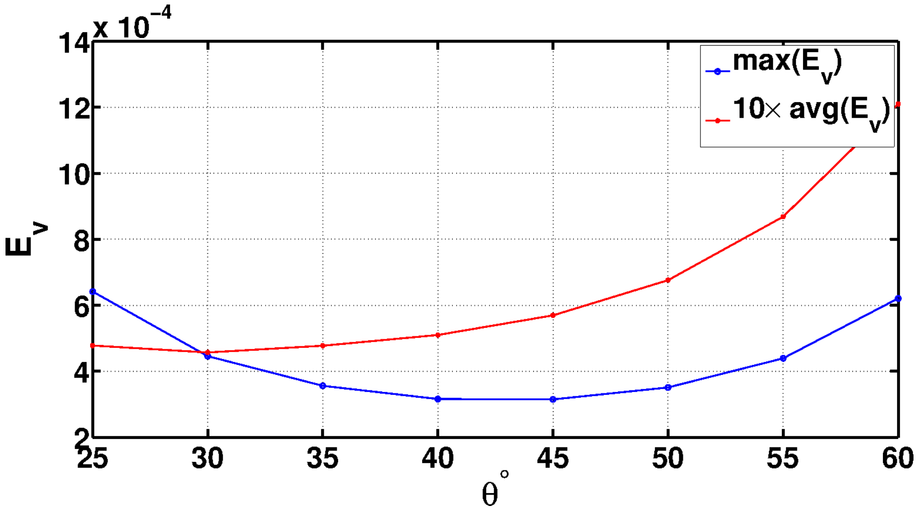

(b)

Figure 4.8: The behaviour of e_v with z and maximum of $e_v(z)$ with θ (a) The wall-normal component of the perturbation kinetic energy in $e_v(z)$ along z. Setting an appropriate cutoff gives us the thickness of the stripe. (b) The maximum in wall-normal perturbation kinetic energy changes with tilt angle θ. The maximum in $e_v(z)$ is lower for $\theta \in (40°, 45°)$

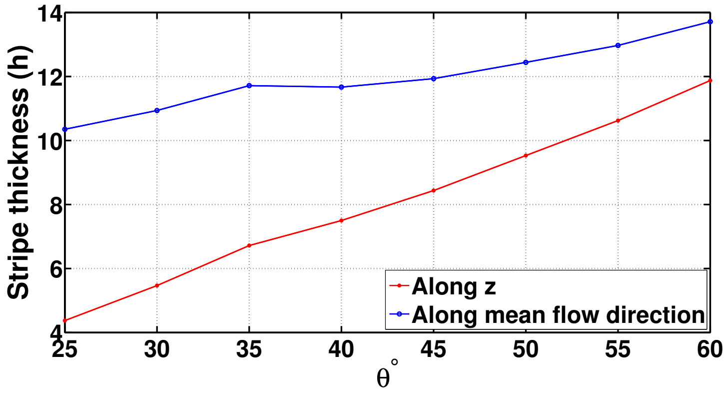

Figure 4.9: The thickness of the lower branch TW stripe solution increases with θ. The red curve represents the stripe thickness measured across the stripe i.e., perpendicular to the stripe, whereas the blue curve shows the stripe thickness measured along the mean flow direction.

4.4 Bifurcation of traveling waves

To investigate the dynamical origins of the above TWs, we continue to solution branches to lower Re using quadratic extrapolation method explained in 2. The other parameters like θ, L_x and L_z, are kept unchanged.

θ	Saddle Node Re_{SN}	Hopf bifurcation Re_H	No. of unstable eigenvalues in the vicinity of the saddle node (LB)
$25°$	488.8826	1058.12	$1r + 1 \times 2c$
$30°$	426.5995	598.034	$1r + 2 \times 2c$
$35°$	393.2030	424.92	$1r + 2 \times 2c$
$40°$	375.4929	408.44	$1r + 2 \times 2c$
$45°$	370.5567	393.58	$1r + 2 \times 2c$
$50°$	377.8913	403.83	$1r + 2 \times 2c$
$55°$	400.4196	421.16	$1r + 2 \times 2c$
$60°$	448.8425	462.49	$1r + 1 \times 2c$

Table 4.1: Values of Re at the saddle-node bifurcation point of TW solutions for different tilt angles θ. It also lists the stability of LBTW in the vicinity of the saddle-node point. When LBTW is an edge state, there is only one real unstable eigenvalue. As Re is reduced, LBTW undergoes Hopf bifurcation adding complex pair of eigenvalues.

The bifurcation diagram of the TW solutions at various angles is shown in Figure 4.10. All the TWs emerge through saddle-node bifurcations at values of Re listed in Table 4.1. From the saddle-node towards increasing Re, there are two solution branches referred to as lower branch (LBTW) and upper branch (UBTW) traveling waves. For all the solutions, the perturbation kinetic energy decreases for LBTW and increases for UBTW as Re increases. In other words, as Re increases, the amplitude of perturbations necessary to cross the laminar-turbulent boundary decreases. For the chosen computational domain size, the TW solution which exists at the lowest Re is for the stripe tilted with respect to the streamwise direction at an angle $\theta = 45°$ which is $Re_{SN} = 370.5567$.

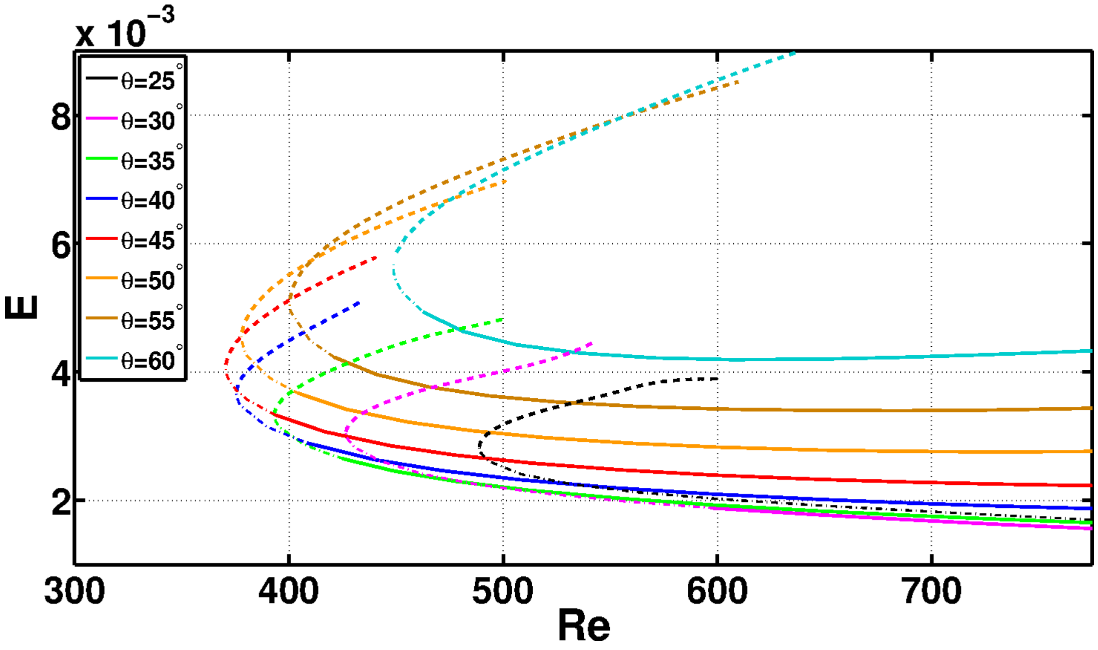

Figure 4.10: The bifurcation diagram of TW solutions for various tilt angles θ in different colours. The bifurcation is shown on Re vs. E plot where E is the perturbation kinetic energy averaged over the domain volume. As Re increases, the perturbation kinetic energy of the lower branch traveling wave solutions decreases, suggesting that a smaller and smaller perturbation amplitude is needed to cross the laminar-turbulent boundary and therefore to trigger turbulence.

At the saddle bifurcation point, both the upper and the lower branches of all the solutions are unstable with more than one unstable direction. As Re increases, the upper branch solutions become more and more unstable with additional unstable eigenvalues. However, the lower branch starts losing the unstable directions and after a certain value of Re retains only one unstable direction and thus qualifying as the edge state. In Figure 4.11, the saddle-node Re at multiple tilt angles θ is shown (blue). It also shows values of Re above which the lower branch of TW solution has only one unstable direction. These points have been marked by red dots. These are the points where the TW solutions undergo a Hopf bifurcation. The value of Re for the Hopf bifurcation of the LBTWs reduces as the tilt angle θ is increased and reaches minimum value at $45°$. Then it increases again with θ.

For each tilt angle, the route to chaos starts from this Hopf bifurcation of the LBTW. The periods of the relative periodic orbits emerging from the Hopf bifurcation of the lower branch TW solutions are listed in Table 4.2. For different tilt angles, the RPO

θ	T_{p1}	T_{p2}
25	42.4874	N/A
30	29.8828	66.832
35	73.0069	31.548
40	84.3443	29.3557
45	27.6013	96.8748
50	109.1105	25,9726
55	120.2174	23.125
60	127.2664	N/A

Table 4.2: Time period T_{p_1} (resp. T_{p_2}) of the first (resp. second, if any) RPO bifurcating from the LBTW branch for various tilt angles (deduced from the eigenvalues at their respective Hopf bifurcation). The period T_{p_1} is computed at $Re = Re_H$.

time periods are different and change non-monotonically with θ. It can be proposed from this fact that after the Hopf bifurcations the routes to chaos can be distinct for distinct tilt angles.

These TW solutions have phase velocities in both the streamwise and the spanwise directions. Figure 4.12a shows the streamwise and spanwise phase velocities of the TW solution branches for different θ. The lower branches of all the solutions are advected faster in the streamwise direction compared to the respective upper branch solutions. The streamwise phase speed of the lower branch solutions is higher than the bulk velocity U_b but lower than the streamwise centerline velocity U_{cl} and the upper branch solutions travel at a phase speed which is less than the bulk velocity. This scenario is generic to the wall-bounded shear flows [Wedin and Kerswell, 2004; Pringle *et al.*, 2008]. It is in agreement with the energy of the lower branch and upper branch solutions. The higher the perturbation kinetic energy of a turbulent structure, the lower is its phase speed.

However, interestingly, the phase velocity along the spanwise direction is slower for the LBTW and higher for the UBTW.

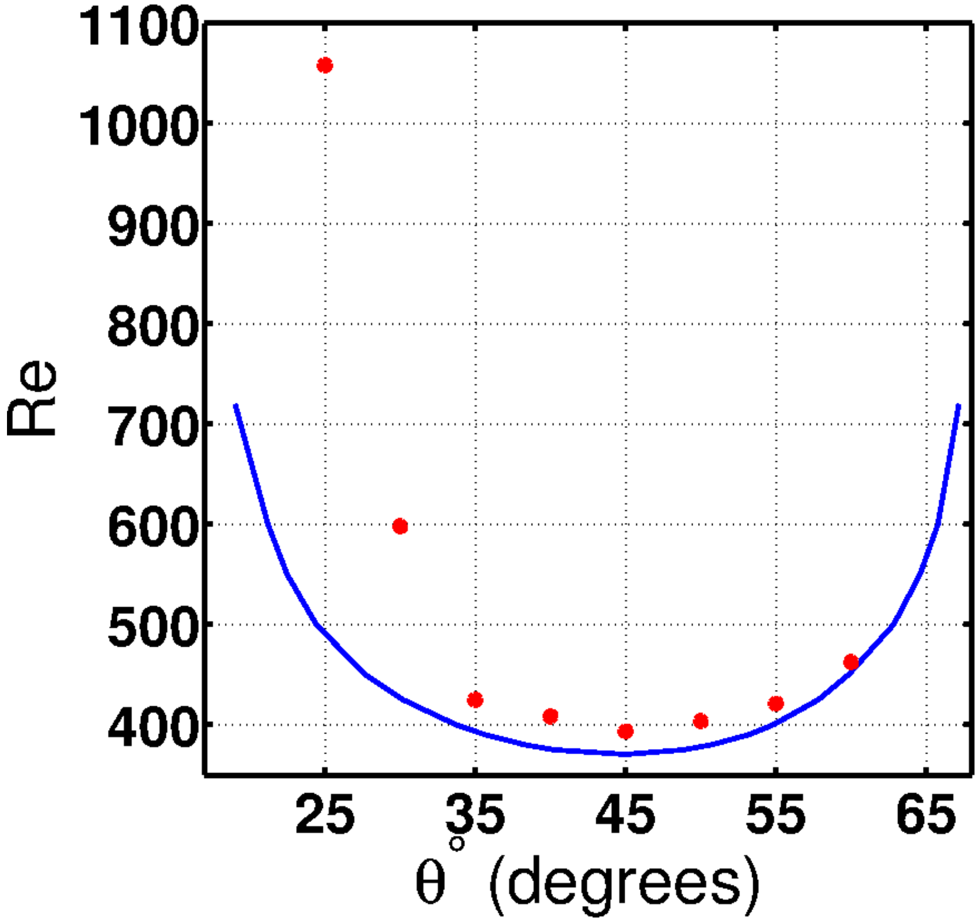

Figure 4.11: The locus of saddle-node bifurcation points at different tilt angles, connected by a blue curve. The red stars represent the Re above which the LBTW is an edge state.

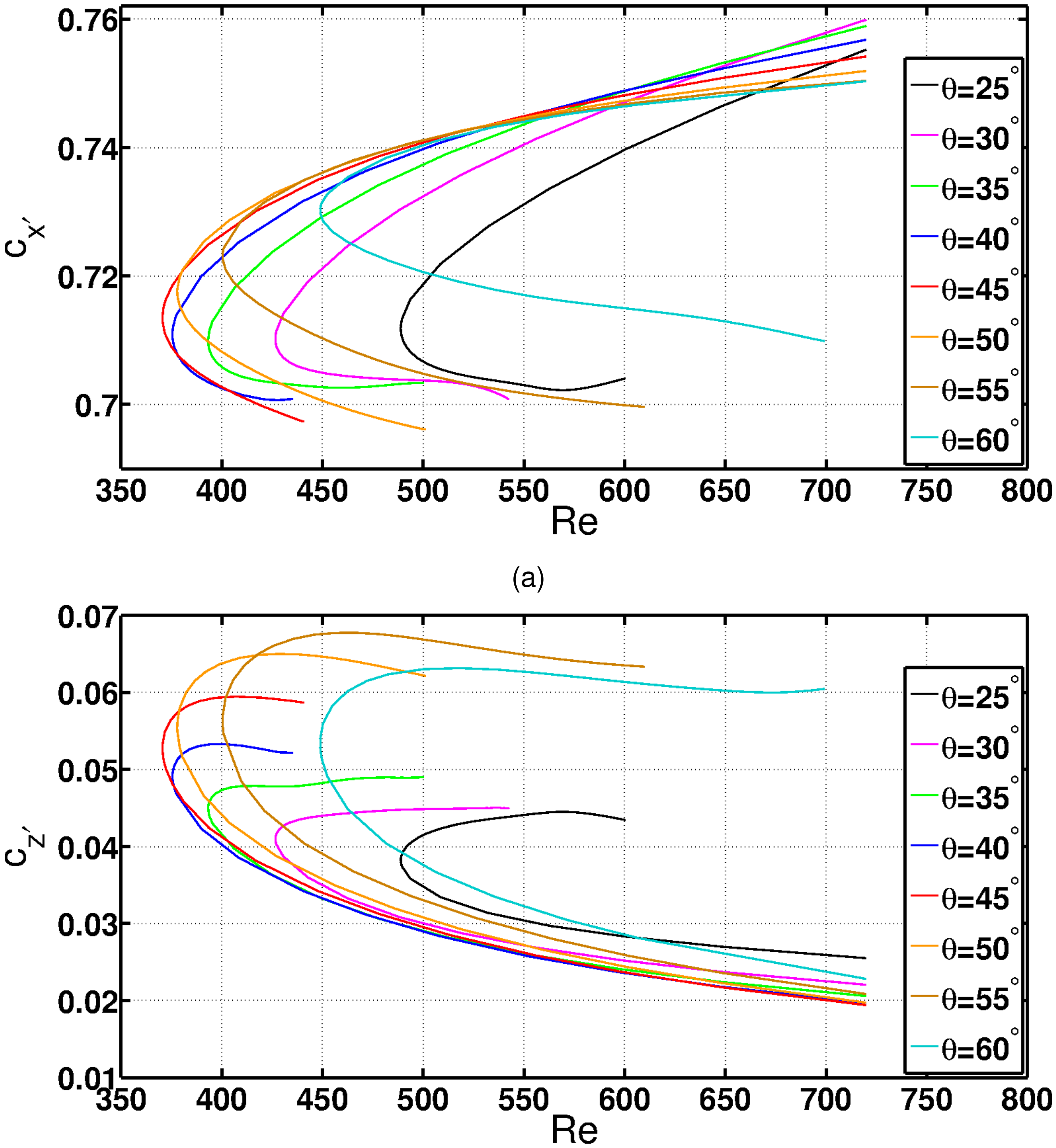

(a)

(b)

Figure 4.12: Phase velocities of the TW solution branches. (a) The streamwise phase velocity of TW solution branches. The lower branch solutions are faster than the corresponding upper branch solutions. (b) The spanwise phase velocity of TW solution branches. In the spanwise direction, the upper branch solutions have higher velocity than their lower branch counterparts.

4.5 Continuation in tilt angle θ

Earlier studies in PCf report that the stripes in PCf do not exist at all the tilt angles in a range [Barkley and Tuckerman, 2007; Duguet *et al.*, 2010a]. Similarly, in PPf, the invariant solutions exist only for a subset of $\theta \in [0, 90]$. Therefore a parametric study is necessary in order to determine the range of tilt angles that show the laminar-turbulent interface i.e., the edge. The bisection carried out at $Re = 720$ was successful in identifying TWs as edge states only for $25^\circ \leq \theta \leq 60^\circ$, which in all cases were easily converged using the Newton algorithm. However, to investigate the range of angles in which the TW solutions can exist, it is necessary to trace out the TW solutions in the space of a new parameter, which is a tilt angle θ. Similarly, the continuation in parameter Re explained in previous section, the LBTW solutions are continued in parameter θ with fixed Re and domain size L_x and L_z. This continuation reveals the range of θ in which the TW solutions exist in chosen domain size and at the chosen value of Re. This continuation in θ is performed at various Re. Figure 4.13

The range of tilt angle (and therefore the stripe angle with the mean flow direction) θ for which the TW solutions exist, reduces as Re is lowered. At $Re = 370.59$ which is the lowest Re the solution exists only for $\theta = 45^\circ$. The locus of the θ_{max} and θ_{min} forms a curve on $Re - \theta$ plane in Figure 4.13b, which represents all the saddle-node bifurcation points for the chosen domain size, tilted at an angle θ with the mean flow direction. This curve is plotted separately in Figure 4.11. It gives an envelope beyond which the localized, TW stripe solutions do not exist for the chosen domain size. The curve appears as slightly asymmetric parabola centered around 45°. It means that as Re gradually increases from zero, the first TW encountered is found to be the TW at $\theta = 45^\circ$. Then as Re continues to increase the range of possible angles widens. However, as Re increases further, the range seems to become asymptotic, and outside this range, the stripe solutions do not exist.

Besides, the routes to chaos for stripes of several selected orientations will be discussed. All the routes start from the secondary bifurcations (viz. Hopf bifurcation) of the same family of lower branch traveling wave solutions, but the routes to chaos differ significantly. The upper branch TW appears not to play any significant role in shaping the state space of the turbulent stripes.

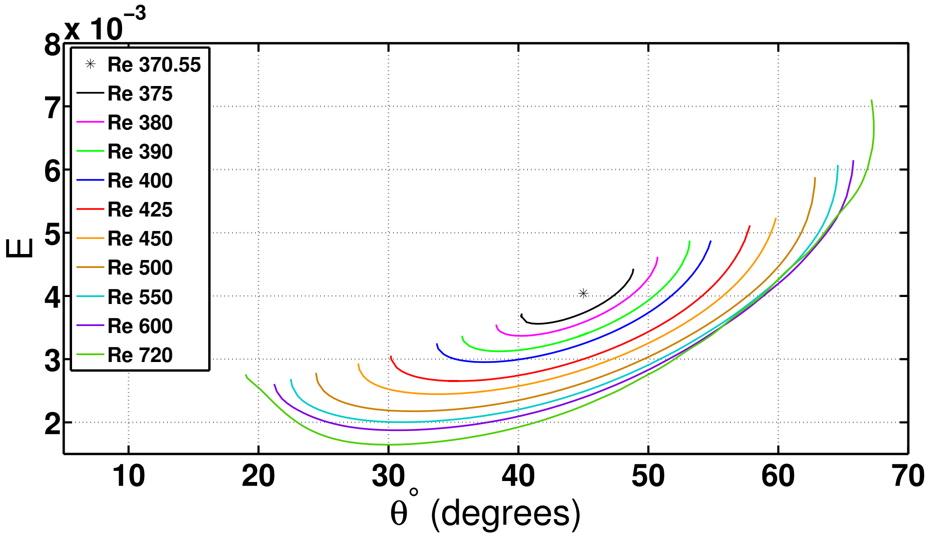

(a)

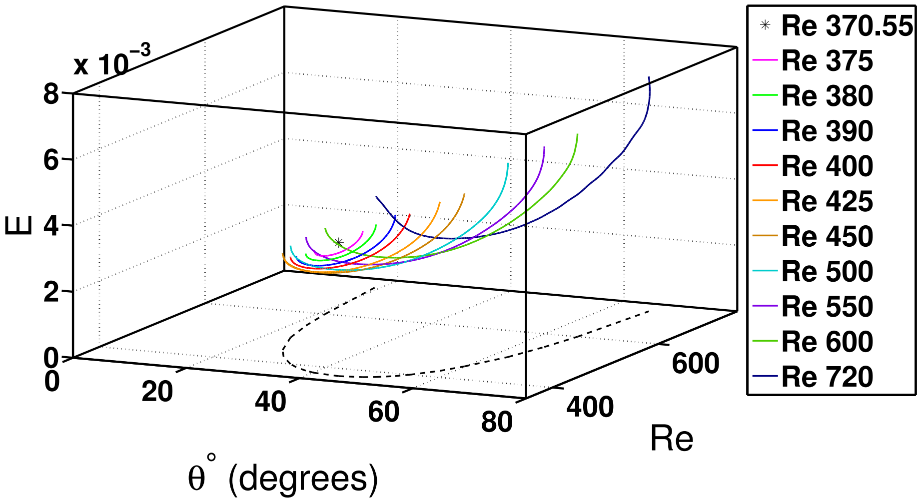

(b)

Figure 4.13: The range in θ of the lower branch TW solutions at different Re. (a)Continuation of LBTW solutions in θ in $E-\theta$ plane (b) Continuation of LBTW solutions in θ for different Re in $Re-\theta-E$ space. The dotted curve at the bottom $\theta-Re$ plane represents the locus of the saddle node points for TW solutions for different tilt angles θ

4.6 Continuation in L_x

It is found that for the chosen domain size i.e. $(L_x, L_y, L_z) = (3.33, 2, 40)$ the minimum Re at which TW solution exists is $Re = 370.59$ at a tilt angle $\theta = 45°$.The TW solutions are localized in z but are extended in x due to the periodicity. For the chosen domain size in x i.e. $L_x = 3.33$ the solution consists of only one wavelength. A parametric study of these solutions was performed by changing the wavelength i.e. L_x .

The tilt angle was chosen as $\theta = 45°$ and L_x is varied, fixing $Re = 720$. The numerical resolution used for the parametric study in L_x is different from the previous investigations. As the continuation in L_x results in a change in the domain size, it is necessary to choose a numerical resolution which will be sufficient at a larger domain size. Therefore the numerical resolution is chosen as $(N_x, N_y, N_z) = (48, 49, 324)$. The LBTW solutios at $Re = 720$ for different L_x are shown in Figure 4.15.

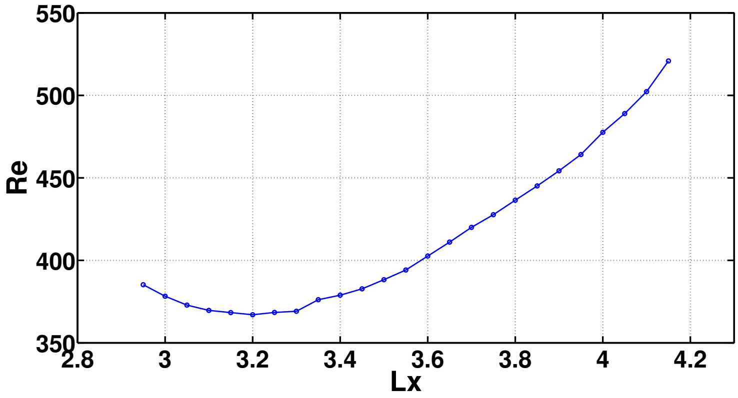

Figure 4.14: Minimum Re or saddle node bifurcation point Re_{SN} at tilt angle of $\theta = 45°$ for different values of L_x in a domain $(L_x, 2, 40)$

The different solutions obtained at different L_x are then continued in another parameter i.e., Re. Again, all the solutions with a different wavelength in L_x occur through saddle-node bifurcations. Figure 4.14 shows the Re of the saddle-node bifurcation for the solutions with different L_x. A local minimum for Re_{SN} is found around 367 and occurs for $L_x = 3.2$. Note that this value is close to the value of 3.33 considered in most of the computations reported here. We can not exclude the possibility for other local minima corresponding to other yet unreported families of traveling wave solutions.

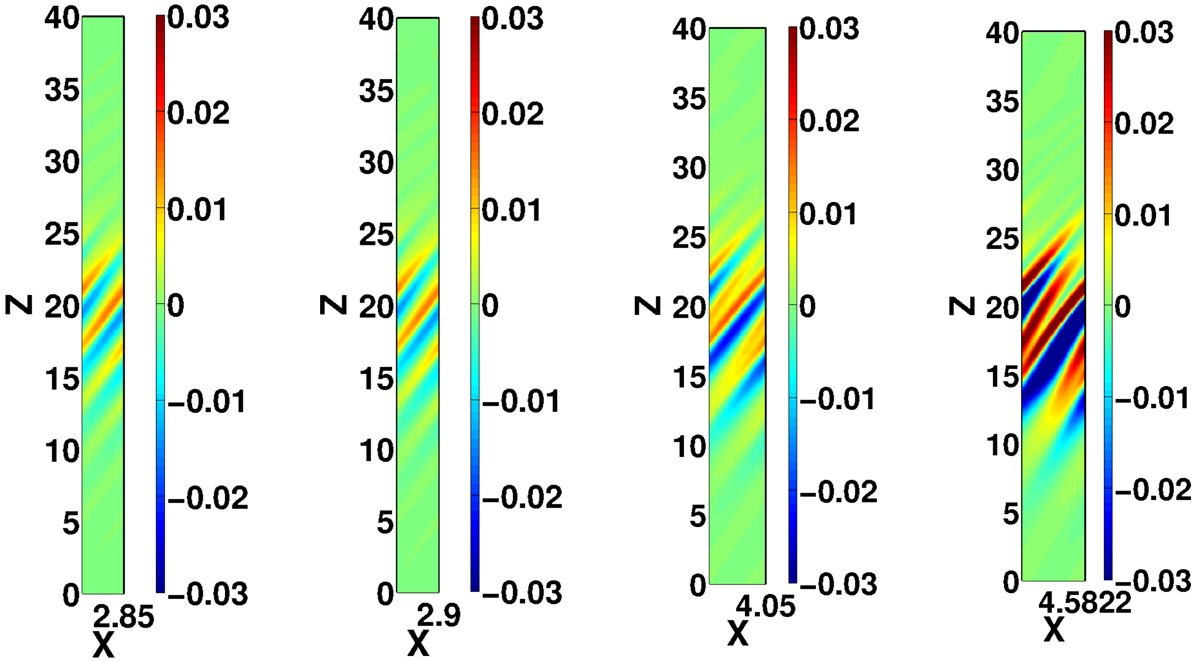

(a) LBTW solution at $Re = 720$ with $L_x = 2.85$

(b) LBTW solution at $Re = 720$ with $L_x = 2.90$

(c) LBTW solution at $Re = 720$ with $L_x = 4.05$

(d) LBTW solution at $Re = 720$ with $L_x = 4.5821$

Figure 4.15: LBTW solutions at $Re = 720$ at various L_x. The flow-fields show wall normal velocity $v(x, y = 0, z)$.

4.7 Route to chaos

For any angle θ for which a TW solution was found as an edge state, it is possible to track the bifurcations of the TW solution until transient (or possibly sustained) temporal chaos occurs, in the spirit of the studies in Refs. [Kreilos and Eckhardt, 2012], [Zammert and Eckhardt, 2015] and [Avila *et al.*, 2013]. From these works respectively in the context of plane Couette flow, plane Poiseuille flow (both MFU) and localized pipe flow turbulence, both in the presence of additional discrete symmetries imposed, a generic bifurcation scenario emerged as Re is increased beyond the primary saddle-node bifurcation : the edge state solution loses stability in a sequence of classical low-dimensional bifurcations, such as period-doubling or Neimark-Sacker bifurcations, until a chaotic attractor is formed. The story continues further as this chaotic attractor grows in size until it touches its own boundary (the “edge”), resulting in transient rather than sustained chaos, with mean lifetimes decreasing with increasing Re. Mean lifetimes have been found to increase again for larger Re. Only spatial proliferation can resolve the apparently contradictory fact that high-Re turbulent flows should have non-transient dynamics [Avila *et al.*, 2011].

Here we provide an example of a route to chaos for $\theta = 35^\circ$. It is to be noted that the situation is roughly analogous to that in pipe flow from Ref. [Avila *et al.*, 2013] as spatial localization occurs in one dimension only. Here, however, there is no discrete symmetry imposed beyond the obvious x-periodicity. Besides, θ is a well-defined imposed angle and plays the role of an additional parameter, whereas in realistic configurations no angle is imposed.

4.7.1 $\theta = 35^\circ$

In this section, the tilt angle and therefore, the angle of the stripe with mean flow direction is fixed at $\theta = 35^\circ$. The domain size is fixed at $(L_x, L_y, L_z) = (3.33, 2, 40)$. As explained earlier, the invariant TW solution is determined at $Re = 720$ via the bisection method. Then the quadratic extrapolation is used to trace the solution branch in parameter space, the parameter being the Reynolds number Re. The bifurcation diagram showing this route to chaos is shown in Figure 4.16. The y-axis of the diagram represents the perturbation kinetic energy. The points on the bifurcation diagram are plotted taking the mean of this perturbation kinetic energy over corresponding attractors/saddles. The details of the diagram are discussed in the following.

It is observed that this TW solution emerges through a saddle-node bifurcation at $Re_{snTW} = 393.203$. At the bifurcation point, two TW solution branches emerge, the 'upper branch' (UBTW) and the 'lower branch' (LBTW). From the saddle-node bifurcation, both the branches can be traced to higher Re. The TW solution determined at $Re = 720$ and discussed above belongs to the lower branch i.e., LBTW.

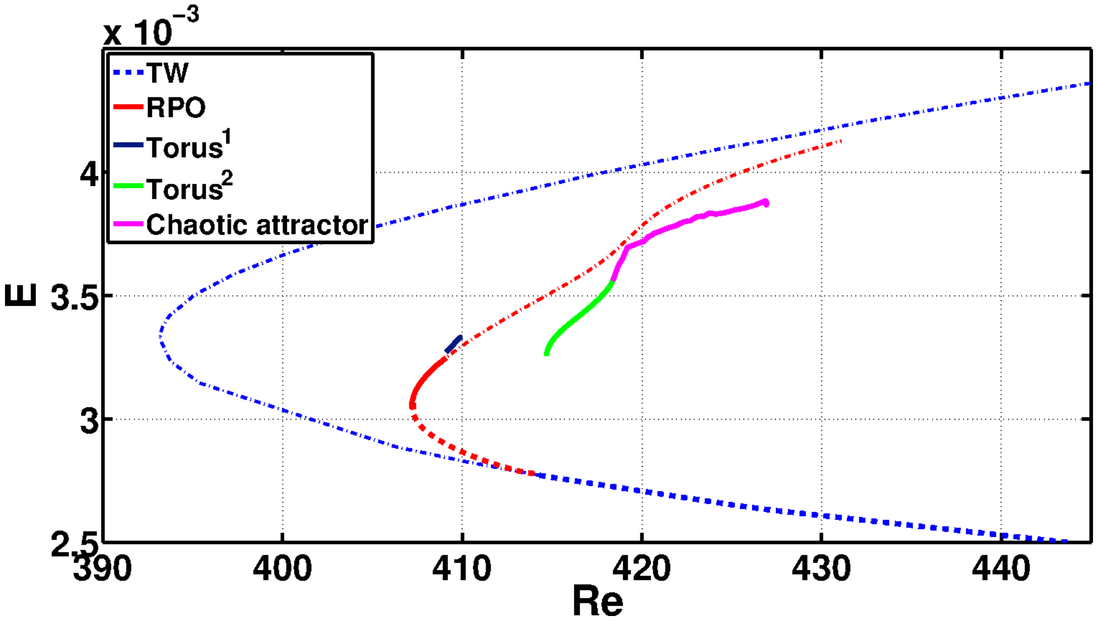

Figure 4.16: The route to chaos for a stripe at a tilt angle $\theta = 35°$.

Importantly, unlike in [Avila *et al.*, 2013; Zammert and Eckhardt, 2015; Kreilos and Eckhardt, 2012] the lower TW solution is not an edge state for all the values of $Re > Re_{snTW}$, which alters the route to chaos. At the saddle-node bifurcation, both the lower and the upper branch are highly unstable with multiple unstable eigenvalues. As Re increases, the UBTW becomes more and more unstable, but LBTW loses the unstable eigenvalues, and from $Re > Re_H = 414.25$ onwards retains only one unstable eigenvalue. In other words, the LBTW is an edge state on the laminar-turbulent basin boundary for $Re \geq Re_H = 414.25$.

While tracing the LBTW towards *lower* Re, it undergoes a Hopf bifurcation and gains two unstable complex eigenvalues at $Re = Re_H = 414.25$. A branch corresponding to a relative periodic orbit solution (RPO) bifurcates off this point and could be tracked using the same continuation algorithm in the direction of decreasing Re. This RPO solution itself appears through a saddle-node bifurcation at $Re_{snRPO} = 407.2019$.

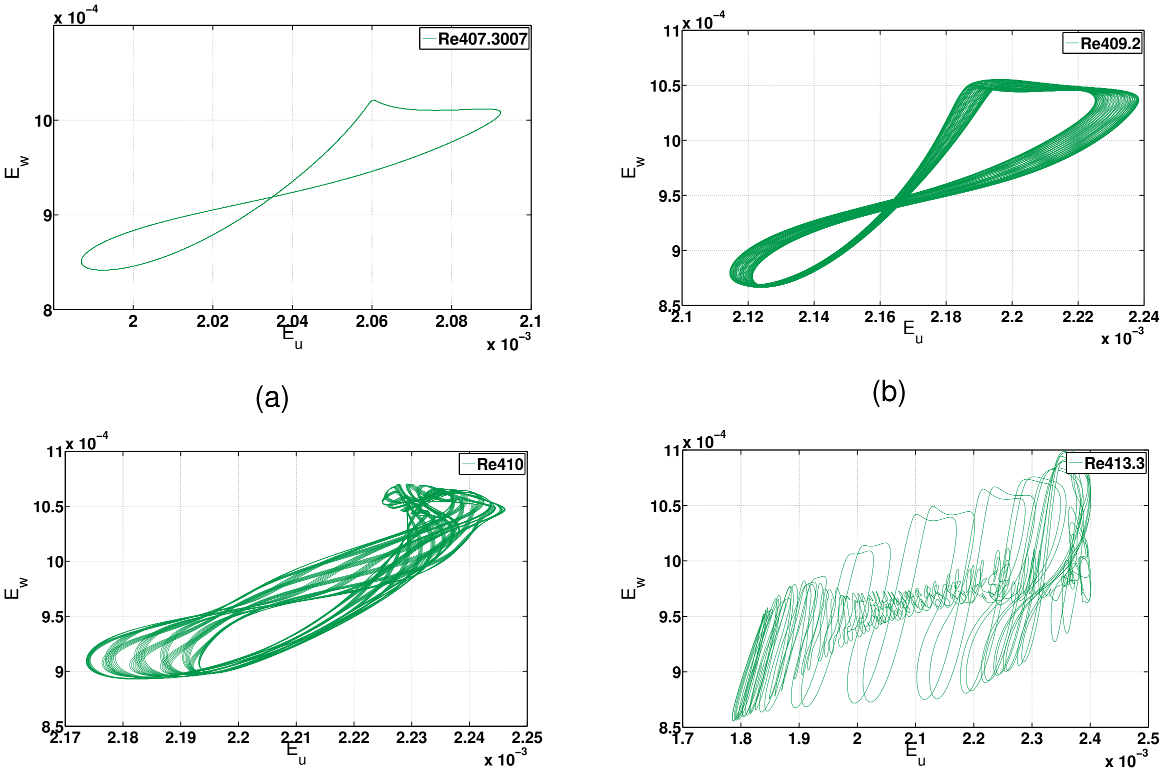

(a) (b)

(c) (d)

Figure 4.17: (a) Stable UBRPO at $Re = 407.30$. This UBRPO is stable between the range of $407.20 < Re < 409.1$. Then it undergoes Neimark-Sacker bifurcation, and the new attractor is 2-Torus (b) Stable 2-Torus at $Re = 409.2$. This 2-Torus emerges from the bifurcation of the UBRPO. It remains stable in a range $Re \in (409.1, 410.1)$. (c) 2-Torus just before breakdown at $Re = 410$. This torus becomes unstable for $Re > 410.1$ and then disappears. Afterward, the dynamics become transient, and the trajectories starting from underlying RPO spend a considerable amount of time along the unstable RPO and then go to the laminar fixed point. This transient dynamics is evident in $Re \in (410.1, 413.3)$. (d) Complicated attractor at $Re = 413.3$. This attractor deemed to be organized around an unstable periodic orbit and an unstable 2-Torus. The heteroclinic connections between these two unstable sets construct this attractor.

At the saddle-node bifurcation of the RPO, the upper branch (UBRPO) is stable (Fig. 4.17a) and the lower branch (LBRPO) is unstable, with only one unstable eigenvalue. Therefore, in the range $Re \in [407.2019, 414.25]$ the edge state is the LBRPO and not the LBTW.

To our knowledge, this is the first example of a stable periodic orbit in subcritical shear flow in the absence of imposed discrete symmetry (beyond the imposed spatial periodicity and the tilt angle).

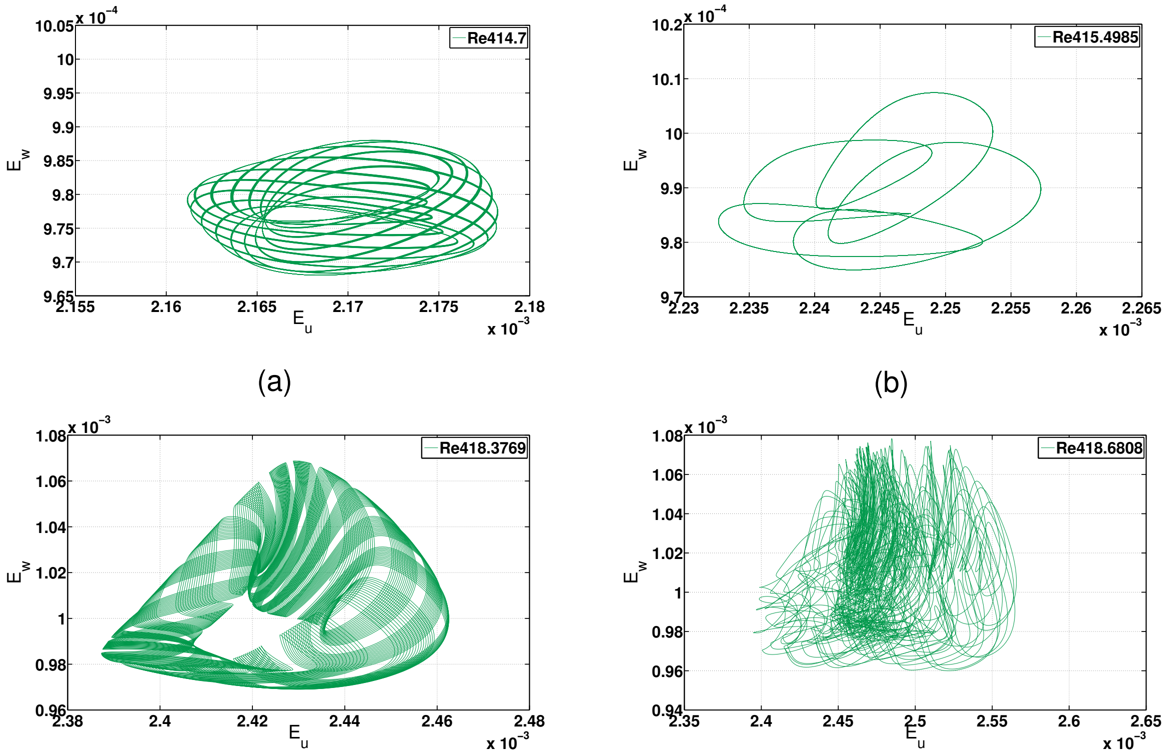

(a) (b)

(c) (d)

Figure 4.18: (a) 2-Torus T_2^2 at $Re = 414.7$. At $Re > 414.7$ the T_2^2 becomes stable and remains so for $Re < 415.2$. (b) The T_2^2 again falls to an RPO for intermediate range in Re. The figure shows the RPO at $Re = 415.498$. It is not clear if T_2^2 and this RPO are connected and if show then in what way. (c) 2-Torus at $Re = 418.377$. After a brief periodic window in Re the 2-Torus recovers and is stable in the range $416 \lessapprox Re < lessapprox418.4$. (d) T_S^2 becomes unstable and the dynamics look chaotic for a small range in $Re \in (418.4, 419.1)$.

The stable UBRPO is then continued to higher Re from its saddle-node bifurcation point. At $Re > 409.1$ it undergoes a Neimark-Säcker and hence becomes unstable in the favour of a stable T_1^2 (Figure 4.17b). Beyond this point, one cannot rely only on

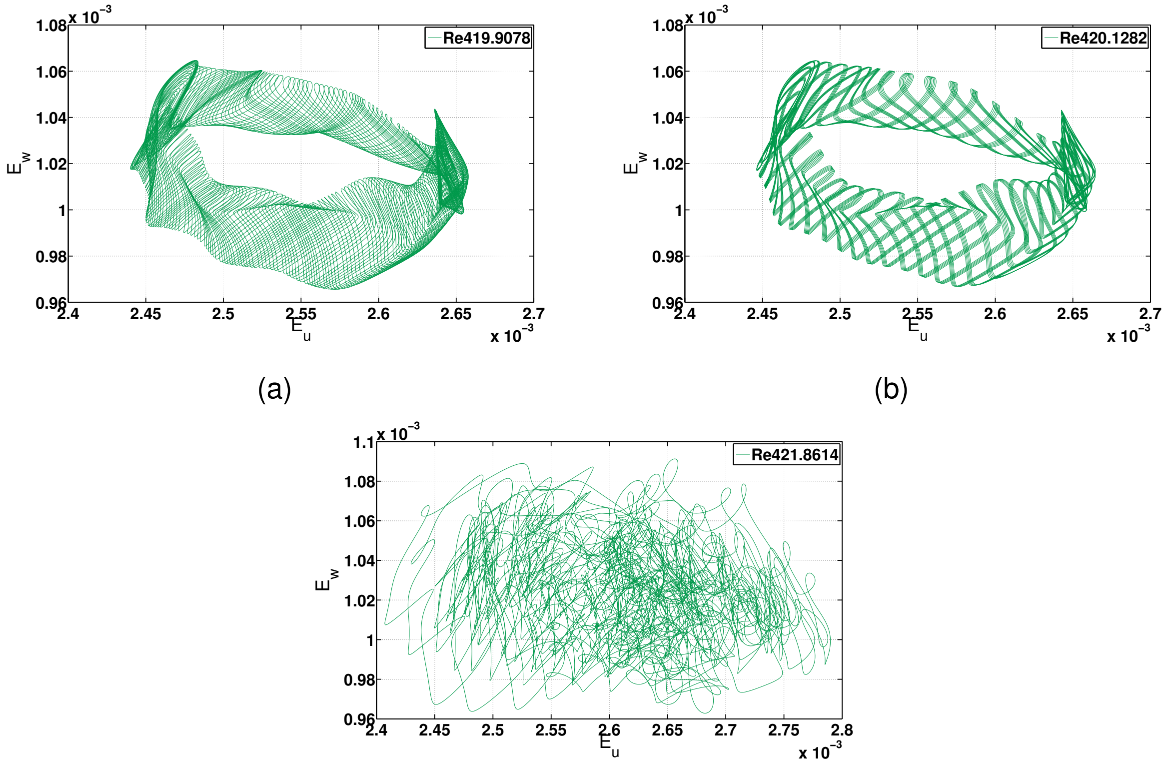

(a)

(b)

(c)

Figure 4.19: (a) A 2-Torus at $Re = 419.908$. (b) 2-Torus at $Re = 420.1282$. (c) Chaotic attractor at $Re = 421.86$.

the continuation algorithm anymore. The direct numerical simulations (DNS) initialized with the Newton converged invariant solutions are also necessary in order to describe the route to chaos. It makes fold bifurcations - in particular - difficult to locate. The 2-torus T_1^2 is then tracked until $Re = 410.1$ beyond which it seems to become linearly unstable 4.17c. Then in the small window of $410.1 \lessapprox Re \lessapprox 413.3$, the dynamics are transient. The trajectories starting from an RPO spend a considerable amount of time along the RPO and then finally go towards the laminar fixed point. Then again the attractor emerges in the phase space during the range $413.3 \lessapprox Re \lessapprox 414.7$ as shown in Fig 4.17d. The dynamics in this narrow range is harder to describe. It appears that the attractor is organized around the two unstable invariant sets viz. UBRPO and an unstable 2-torus. The underlying 2-Torus (Hereafter named as T_2^2) becomes evident as Re is increased further where it becomes linearly stable. This T_2^2 remains stable for $414.68 \lessapprox Re \lessapprox 415.4$. The phase portrait of the attractor is shown in Figure 4.18a. The origin of this T_2^2 is not clear. Careful "continuation" of T_2^2 by DNS towards neighbouring parameters indicates that T_1^2 is most likely born in a saddle-node bifurcation of 2-tori at

$Re \approx 414.675$.

With further increase in Re, another stable relative periodic orbit emerges at $Re = 415.49$ as shown in Figure 4.18b. It is not clear if T_2^2 and this RPO are connected to each other and if they are then in what way.

For $415.49 \lessapprox Re \lessapprox 418.38$ the attractor is another 2-Torus (T^23) (Figure 4.18c). Further increase in Re makes this -Torus linearly unstable and for a brief interval in Re the attractor becomes chaotic Figure 4.18d. It is not clear why this 2-Torus evolves to mildly chaotic attractor just for a brief period. One possibility is there are two unstable 2-Tori in the phase space at this parameter value and the heteroclinic connections between these two sets make the attractor mildly chaotic. Another unstable 2-Torus (T^24) appears as Re is increased beyond the point where the 2-Torus (T^24) becomes stable and remains so in a short range $419.18 \lessapprox Re \lessapprox 420.35$ as shown in Figure 4.19a and in Figure 4.19b. Now this (T^24) further becomes unstable and an chaotic attractor emerges at $Re > 420.35$ Figure 4.19c. For $Re \geq 426.9$ instances of relaminarisation are reported after a long chaotic transient. This suggests a boundary crisis near $Re \approx 426.93$.

Figure 4.20 shows the phase portraits of different attractors at different values of parameter Re. This figure helps in visualizing the evolution of the attractors with the parameter Re.

Summing up this investigation there is a non-trivial route to chaos, based on three successive saddle-node bifurcations : First the TW, then the RPO and finally a new family of tori T_2^2. Each successive saddle-node bifurcation brings an additional degree of freedom in the time dependence until robust chaos sets in.

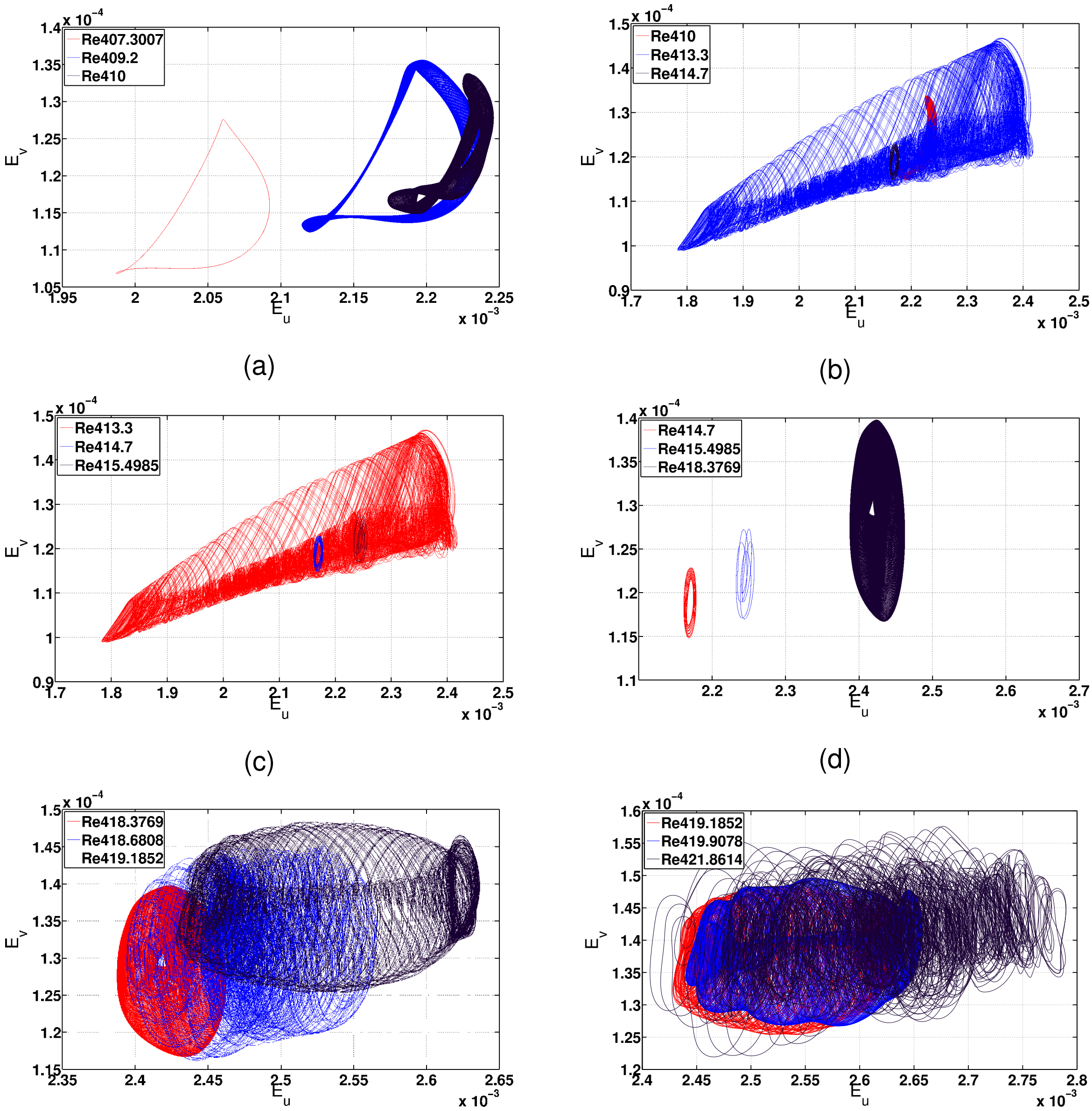

(a) (b) (c) (d) (e) (f)

Figure 4.20: The multiple attractors in the phase space plotted simultaneously to understand the relation between multiple attractors and their respective evolution (a)Phase portraits at $Re \in (407.30, 409.2, 410.0)$. It represents RPO, and T_1^2 at different Re. (b) Phase portraits at $Re \in [410.0, 413.3, 414.7]$(c) Phase portraits at $Re \in (413.3, 414.7, 415.498)$ (d) Phase portraits at $Re \in (414.7, 415.4985, 418.377)$. A stable 2-Torus, then a RPO in a brief window and then again a 2-Torus (e)Phase portraits at $Re \in (418.377, 418.681, 419.185)$. It shows a stable 2-Torus, its evolution to a mildly chaotic attractor and then to another stable 2-torus (f) Phase portraits at $Re \in (419.185, 419.908, 421.861)$. Two 2-Tori and a chaotic attractor

4.8 Discussions

Here, we reported new families of nonlinear traveling wave solutions of the channel flow which show localization, obliqueness of the laminar-turbulent interface and quasi-streamwise streaks and vortices - features shared by turbulent stripes in a variety of shear flows. The method relies on the ability of edge tracking to identify simple edge state solutions, coupled with an efficient root-finding algorithm. All the solutions reported here occur through saddle-node bifurcation in a parameter space parametrized by Re and are linearly unstable though the number of unstable directions is generally very low, ranging from one for edge states up to six for upper branch solutions near their saddle-node bifurcation point. To our knowledge, among all the reported solutions, these are the localized states which appear at the lowest value of Re with minimum $Re_{SN} \approx 367$ at $\theta = 45°$. Interestingly, it is the lower branch of all of these TW solutions from which the route to chaos starts. The routes leading from each of these traveling waves to chaos are essential to explain the direct emergence of turbulent stripes and deserve a separate parametric study. One example of a route to chaos for a stripe tilted at an angle $\theta = 35°$ has been extensively discussed in this chapter.

The main idea is that the state space for the turbulent dynamic is structured around a skeleton formed by the unstable nonlinear states with their stable and unstable manifold. The TWs identified here are the simplest of these states. The different Hopf bifurcations of these waves lead to new branches of stable/unstable periodic orbits whose further bifurcations, cover the turbulent attractor specific to each tilted domain.

We also report a strict subset of tilt angle values for which these TW solutions can appear. The angle selection mechanism of the stripes observed in the experiments can be studied considering this fact. As these solutions are nonlinear, adding different solutions to create a new solution is not allowed. Therefore it can be argued that different routes to chaos coexist for different values of the stripe tilt angle θ. The TW with $\theta = 45°$ is the one that persists to the lowest Re.

Interestingly, in the experiments, the stripes have the same angle with respect to the mean flow direction at the onset. It remains to be understood why no turbulent stripe forms or sustains with an angle larger than $45°$ in experiments, whereas this is allowed for traveling wave solutions. This seemingly contradictory fact is likely to be related to the choice of the tilted domains rather than to the traveling waves themselves.

5 Deterministic origin of turbulent stripes

The classical approach to investigate turbulence is to study the instabilities of the laminar base flow for the infinitesimal perturbations. Flows like Taylor Couette flow (TCf) with the inner cylinder rotating, show supercritical transition to turbulence where the flow becomes turbulent following a sequence of instabilities starting from the laminar base flow [Gollub and Swinney, 1975; Feigenbaum, 1979]. As the rotation speed increases, then at a critical Re, the laminar flow becomes unstable and undergoes a pitchfork bifurcation as shown in Figure 5.1a giving rise to the Taylor vortices [Cliffe *et al.*, 2012]. With further increase in the rotation speed, these vortices become wavy, and eventually, the flow becomes turbulent. However, in many other wall-bounded shear flows like pipe flow (Hagen Poiseuille flow-HPf), plane Poiseuille flow (PPf), plane Couette flow (PCf), etc. the transition to turbulence is subcritical meaning, turbulence arises in spite the laminar base flow being linearly stable, [Drazin and Reid, 2004]. The sub-critical transition to turbulence is also characterized by localized turbulent patches called puffs in pipe flow [Wygnanski and Champagne, 1973; Mullin, 2011] and oblique stripes in flows extended in two dimensions such as PPf,PCf,TCf etc. [Tsukahara *et al.*, 2005; Dauchot and Daviaud, 1995; Duguet *et al.*, 2010a].

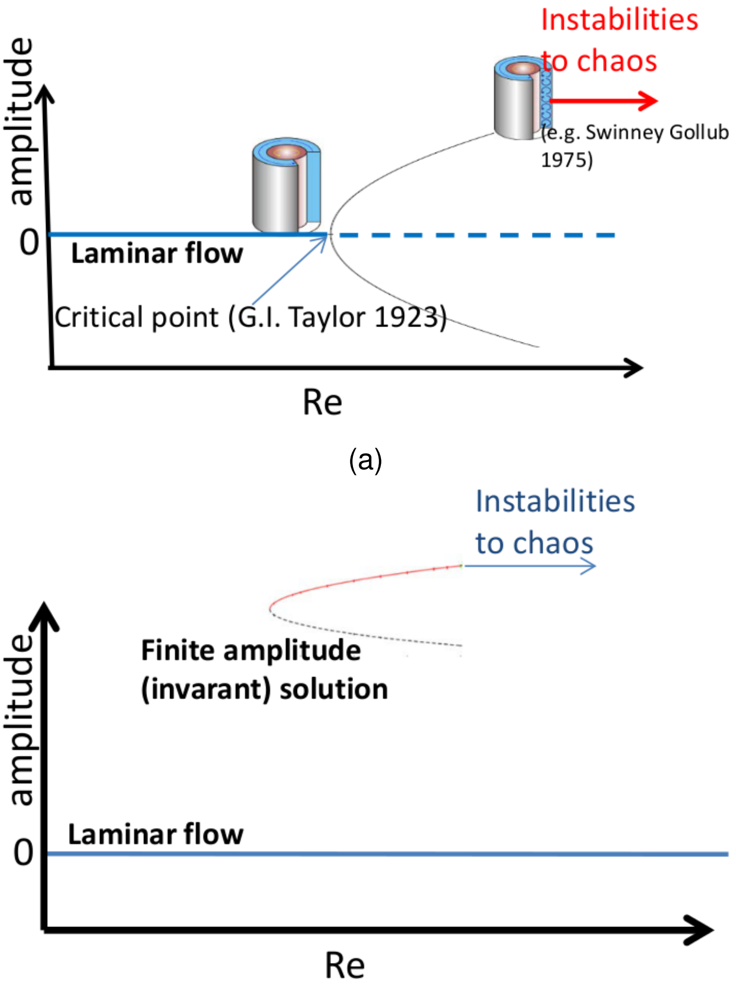

(a)

(b)

Figure 5.1: The instability sequence in (a) linearly unstable and (b) linearly stable flows. (a)The instability sequence of a linearly unstable flow (e.g., Taylor Couette flow with only inner cylinder rotating). The laminar base flow becomes linearly unstable and undergoes transcritical bifurcation at a critical Re. In the case of TCf with the inner cylinder rotating, the laminar base flow becomes unstable, giving rise to the Taylor vortices. As the rotation speed of the inner cylinder increases, the Taylor vortices become wavy, and eventually, the flow becomes turbulent. (b)In many shear flows, turbulence occurs despite the laminar base flow being linearly stable. The chaotic motion results from a sequence of instabilities emerging from the bifurcations of the non-trivial invariant solutions of the Navier-Stokes equations. These invariant solutions occur through a saddle-node bifurcation and are disconnected from the laminar base flow.

A popular proposition is that in linearly stable flows turbulence does not develop from a stable (experimentally observable) state but from unstable non-trivial exact coherent solutions (ECS) of the Navier-Stokes equations, which appear through saddle-node bifurcations as shown in Figure 5.1b [Eckhardt *et al.*, 2007]. These solutions are disconnected from the linearly stable laminar base flow. They can be either equilibria (EQ), traveling waves (TW), periodic orbits (PO) or relative periodic orbits (RPO) and are also referred to as invariant solutions [Waleffe, 1998; Kawahara *et al.*, 2012]. The invariant solutions are composed of low and high-speed streaks and streamwise vortices - which are also the structural components of turbulence. A sequence of bifurcations starting from these solutions lead to chaotic dynamics. Experiments in the pipe flow showed some signature of these ECS, especially the traveling waves but the agreement with the full instantaneous flow field is still inconclusive as recurrence in experiments is very rare [Hof *et al.*, 2004; De Lozar *et al.*, 2012].

A variety of ECS have been computed for different flows in numerical simulations [Nagata, 1990; Faisst and Eckhardt, 2003; Duguet *et al.*, 2008; Zammert and Eckhardt, 2014b; Zammert and Eckhardt, 2014a]. Many of them are computed in minimal flow units and therefore lack the vital property of turbulent structures at low Re which is their localization. Studies in the pipe flow [Avila *et al.*, 2013; Ritter *et al.*, 2016], plane Couette flow (PCf) [Kreilos and Eckhardt, 2012] and in PPf [Zammert and Eckhardt, 2015]- which are performed in symmetric subspace- show the emergence of ECS in saddle-node bifurcations and sequences of instabilities to a chaotic attractor and then to a chaotic saddle through a boundary crisis. After the boundary crisis when the chaotic dynamics become transient, it becomes difficult to trace these dynamics further to higher Re beyond the critical value of Re where the turbulent structures are observed in the experiments.

Equally, attempts to track turbulent puffs or stripes to lower Re where the dynamics are expected to simplify, have failed. Instead of simplifying turbulence becomes transient[Faisst and Eckhardt, 2004; Peixinho and Mullin, 2006; Hof *et al.*, 2006; Borrero-Echeverry *et al.*, 2010; Hof *et al.*, 2008] and abruptly relaminarizes.

As described in Chapter 3, the experiments were performed in a channel of size $(L_x, L_y, L_z) = (4000h, 2h, 490h)$ where x is streamwise direction, y is wall normal direction and z is spanwise direction. It is observed that at $Re = 1650$, turbulence occupies the entire domain (Figure 5.2a). For Re below ~ 1500 , criss-cross patterns start forming (Figure 5.2b and 5.2c). Further reduction in Re (below ~ 1050) these criss-cross patterns break into isolated stripes (Figure 5.2d). For $Re < 850$ the stripes orient themselves at angle $\theta \approx 45^{\circ}$ with respect to the streamwise direction (Figure 5.2e). Further reduction in Re below 650 results in laminar flow as the turbulent stripes become transient in nature.

In the following, we will demonstrate for plane Poiseuille flow that the turbulent state can be traced all the way to its origin. In this limit, the flow simplifies to a branch of invariant solutions of the Navier-Stokes equations, which is a traveling wave. As will be shown in the following, this TW branch is the same branch obtained using edge tracking at 45° in Chapter 4. Similar to the turbulent stripes in experiments, this dynamically simple structure also features obliqueness to the mean flow direction, spatially localization, and feature quasi-streamwise vortices and streaks.

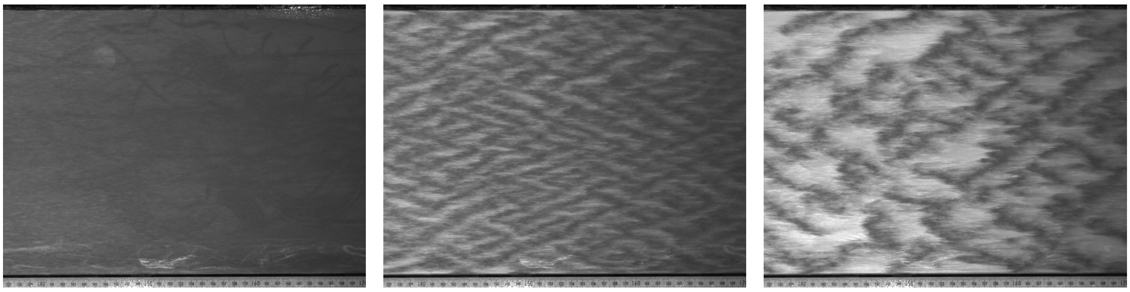

(a) $Re = 1650.$ (b) $Re = 1380.$ (c) $Re = 1125.$

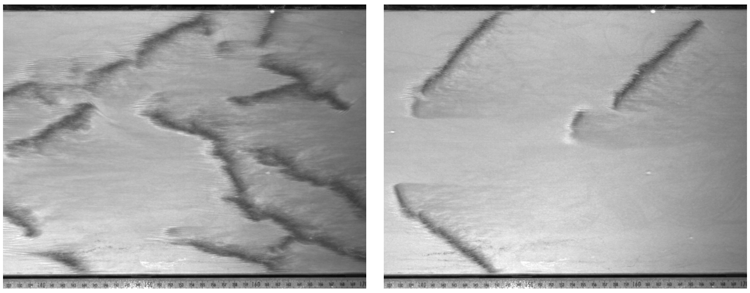

(d) $Re = 930.$ (e) $Re = 675.$

Figure 5.2: The figure shows flowfield visualizations from the experiments. These images are taken from the top of the channel where the axis of the camera is in the direction of the wall-normal direction y. Therefore the images depict flowfields in xz plane. (a) At $Re = 1650$, turbulence is fully developed and without any visible patterns or features. (b) When Re is reduced below 1500, the turbulence breaks into criss-cross patterns. The figure shows the flowfield at $Re = 1380$. (c) Further reduction in Re, for e.g., at 1125 the criss-cross patterns become more sparse. (d) As Re is lowered below ~ 1050 gives rise to isolated, oblique stripes. The image shows the isolated stripes at $Re = 930$ (e) As Re approaches a critical point, the orientation of the stripe tends to $\theta \approx 45°$. In all visualizations, the flow is from the left to the right

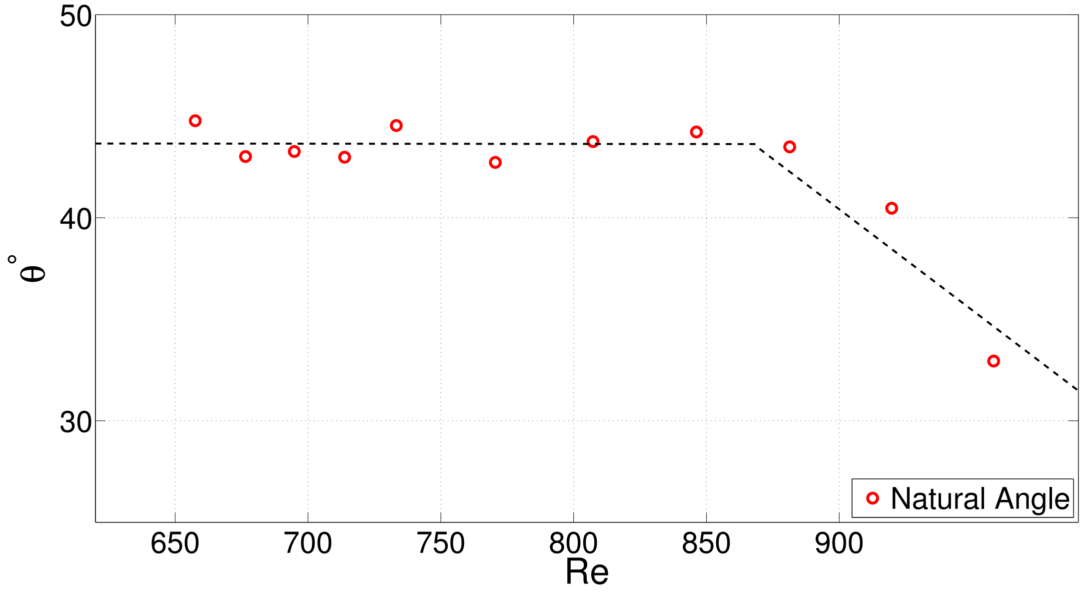

Figure 5.3: As Re is lowered, the stripes have a preferred orientation of $\theta = 45°$. This data is obtained from the experiments in the channel flow. (Ref. Chapter 3)

5.1 Numerical domain

The numerical domain is a rectangular domain of a size $(L_x, L_y, L_z) = (10, 2, 40)$ where L_x and L_z are the lengths of the domain in the periodic directions x and z respectively. L_y is the distance between the walls of the domain. The resolution used is $(N_x, N_y, N_z) = (96, 49, 256)$. As explained before, the turbulent stripes at lower Re have a preferred orientation of $\theta \approx 45^\circ$ with respect to the mean flow direction i.e., the streamwise direction (Figure 5.3). Here we use the tilted domain to simulate the turbulent stripes [Barkley and Tuckerman, 2005; Tuckerman *et al.*, 2014]. The tilt angle of the rectangular box, in turn, fixes the orientation of the stripe with respect to the streamwise direction (see Chapter 2). Therefore, the tilt angle i.e., the angle between the shorter side and the mean flow direction is fixed to $\theta = 45^\circ$. Without any symmetry reduction, the stripe is simulated in the full space. Constant mass flux is maintained along with the directions with periodic boundary conditions. No-slip boundary conditions are imposed at the walls of the domain $y = \pm 1$. For the simulation of turbulent stripe, Code-1 is used. The convergence of the invariant solution and the continuation of these solutions in parameter space is performed using libraries from Code-2. The solutions are converged until the error becomes $\epsilon < 10^{-13}$.

5.2 Method

Starting from a random initial condition at $Re = 900$, the flow settles to a turbulent stripe after ($t \approx 1000$) time units. The stripe is localized in the longer domain direction z and extended in the shorter direction x and oblique to the streamwise direction at an angle $\theta = 45^\circ$. It has all the structural components of turbulent stripes in experiments, like quasi-streamwise streaks and vortices.

Subsequently, the value of Re is reduced by 2, and the simulation is started using a turbulent stripe obtained at $Re = 900$ as an initial condition at $Re = 898$. This stripe settles to its attractor in the phase space in time ($t \approx 300$). After letting the simulation run for some more time, a flowfield is selected randomly and used as an initial condition for the next simulation with Re reduced by a step of 2. This 'quasi-static' reduction of the value Re in steps of 2 using the initial condition from the previous iteration is continued

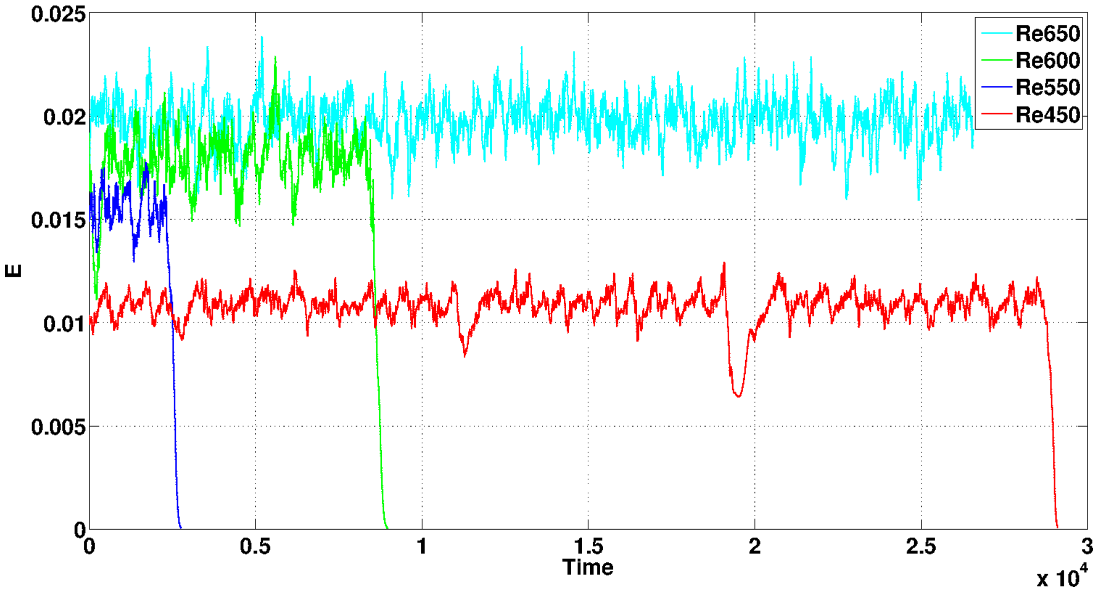

Figure 5.4: The time series at different Re. Though the stripe becomes transient at $Re < 650$, the lifetimes i.e., time for which the stripe sustains before laminarizing are long. The shortest lifetime is observed at $Re = 550$, which is $\tau \sim 2500$. These long lifetimes allow us to track the stripe at lower Re through a quasi-static reduction in Re.

until the value of Re reaches 430. Afterward, the step-size is reduced to 1, and the reduction is continued.

At $Re < 620$ the dynamics become transient i.e., if the simulation is continued for long enough time, the turbulent stripe laminarizes. Figure 5.4 shows the time series of the turbulent stripes at different Re. The shortest lifetime is of order $t \approx 2500$ which is at $Re = 550$. These transients are long enough to allow the dynamics to spend a considerable amount of time around the chaotic saddle in the phase space before going to the laminar state. It allows us to continue the quasi-static reduction in Re towards lower values.

As Re decreases, the fluctuations become smaller and smaller, and the dynamics become simpler. Figure 5.5 shows the evolution of flowfields as Re is reduced.

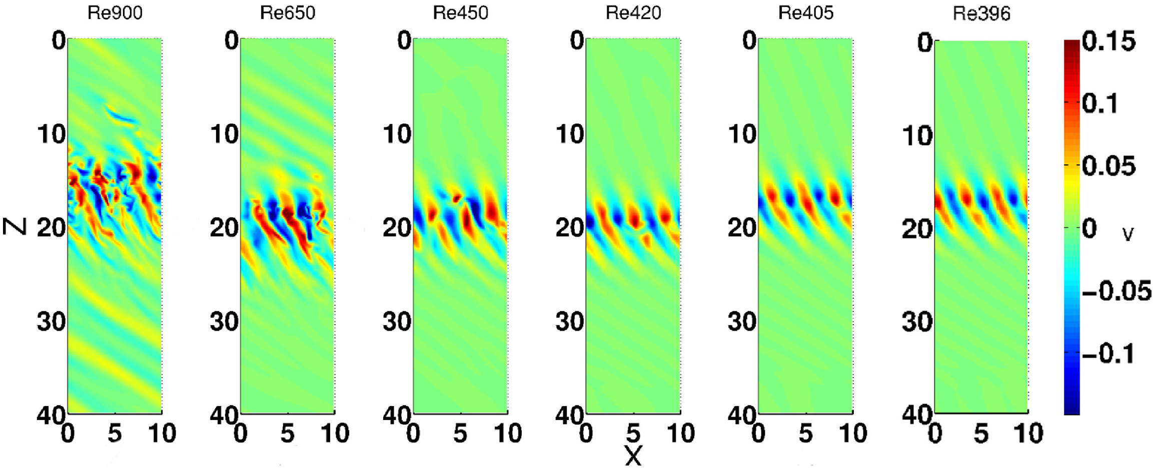

Figure 5.5: Wall normal component of the fluctuating velocity field in the central plane $y = 0$ at different Re. The turbulent stripe gradually evolves into a dynamically simple periodic orbit with decreasing Re. The leftmost panel shows a turbulent stripe at $Re = 900$. As Re is reduced, the flow field becomes dynamically simpler. At $Re = 420$, the dynamics is still chaotic but the fluctuation levels reduce considerably (See figure 5.8). At $Re = 405$, the stripe dynamics in the phase space falls on an attractor, which is topologically a 2-Torus. Further reduction in Re gives rise to a relative periodic orbit. The flow field of the RPO at $Re = 396$ is shown in the rightmost panel. The dynamically simple state at this Re shows all the structural components of the turbulent stripe, like quasi-streamwise streaks and vortices.

5.3 Bifurcation diagram

The bifurcation diagram (Figure 5.6) shows the origins of turbulent stripes in the parameter space of parameter Re. Starting from a turbulent stripe at $Re = 900$, as Re reduces turbulence remains sustained and at $Re < 650$ the dynamics become transient i.e., in the phase space, the attractor becomes a chaotic saddle.

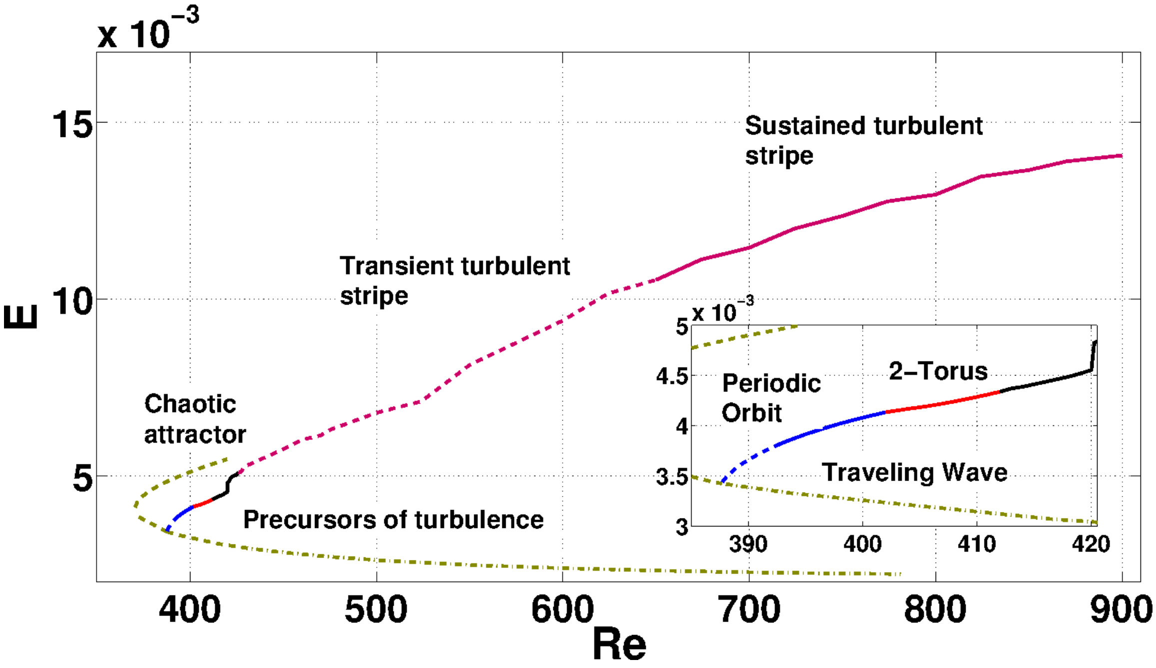

Figure 5.6: The bifurcation diagram obtained by adiabatically reducing the Reynolds number. With reducing Reynolds number, sustained stripe turbulence becomes transient (Re¡ 650), however, the turbulent stripes remain long-lived (order of thousands of advective time units) allowing for the reduction in Re. While the stripe energy reduces with Re, the dynamics remain highly chaotic down to Re 450 and only subsequently begin to simplify. In a range $Re \in (403.5, 412.9)$ the attractor is a 2-Torus. This attractor further simplifies into a relative periodic orbit at $Re < 403.5$. This RPO emerges from Hopf bifurcation of the LBTW at $Re = 387.6$. The traveling wave solution itself emerges in saddle-node bifurcation at $Re = 370.6$.

The dynamics remains transient until $Re = 426$. Below this value, the chaotic set becomes attracting through the boundary crisis. Further reduction in Re simplifies the chaotic attractor, and in a range, $420 > Re > 412.95$ the chaotic attractor is characterized by multi-mode oscillations i.e., a base 2-torus with intermediate bursts. At $Re < 412.95$ the chaotic attractor simplifies into a stable 2-torus. This 2-torus undergoes a reverse Neimark-Sacker bifurcation when Re is reduced, and at $Re \approx 403.5$ the attractor simplifies further to a relative periodic orbit or RPO. This RPO is stable until $Re = 393.5$. Below that it loses its stability. After the RPO becomes unstable, it is then continued further down by using quadratic continuation subroutines from **Code-2**. All the solutions are converged to $\epsilon = 10^{-14}$. This relative periodic orbit solution branch results from the Hopf bifurcation of the traveling wave (TW) at $Re = 387.6$. This unstable TW is also continued in parameter space with quadratic continuation. It is observed that this TW emerges from the saddle-node bifurcation at $Re = 370.6$. Below this Re, no ECS was observed. Here, we note that the traveling wave solution found here belongs to the same family of TW obtained using edge tracking at 45° in Chapter 4. The upper branch (UBTW) and lower branch (LBTW) which emerge through the saddle-node bifurcation are unstable from the beginning. With increasing Re, LBTW starts becoming more and more stable and in $415 < Re < 433$ loses all but one unstable direction. After that, the lower branch of TW solution acts as an edge state with codimension 1 - a stable manifold of which separates the initial conditions that go turbulent from the ones that laminarize. The upper branch of the TW (UBTW) on the other hand becomes more and more unstable with increasing Re. The point to be noted here is that, in the earlier studies of determination of the route to chaos, it is the upper branch which undergoes a sequence of bifurcations and therefore is instrumental in the route to chaos [Kreilos and Eckhardt, 2012; Avila *et al.*, 2013; Ritter *et al.*, 2016; Zammert and Eckhardt, 2015]. In the present study, the solution branch which is relevant for the route to chaos/turbulence bifurcates from the Hopf bifurcation of the LBTW.

The dynamically simple TW solution as well as the RPO solution structurally comprises of alternate high and low speed streaks aligned more or less along mean flow direction, arranged in the form of stripe (Figure 5.7a,5.7b) which are similar to the turbulent stripe (figure 5.7c).

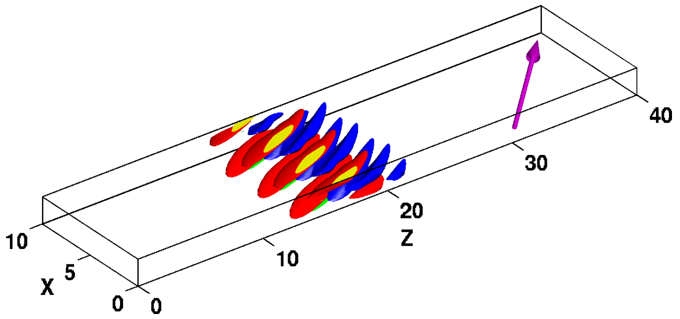

(a) Traveling wave at $Re = 370.59$. The isovalues : Streamwise velocity (red and blue) ± 0.13 and Streamwise vorticity (green and yellow) ± 1.0

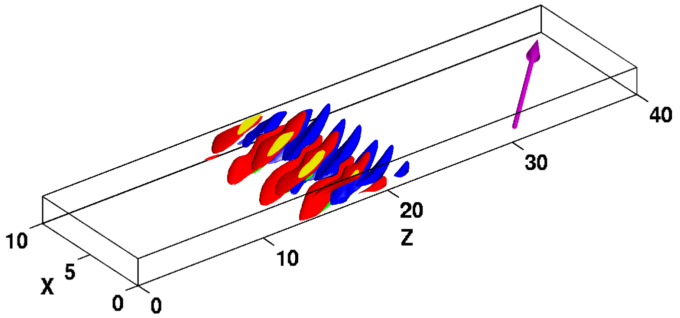

(b) Relative periodic orbit at $Re = 395$. The isovalues : Streamwise velocity (red and blue) ± 0.13 and Streamwise vorticity (green and yellow) ± 1 .0

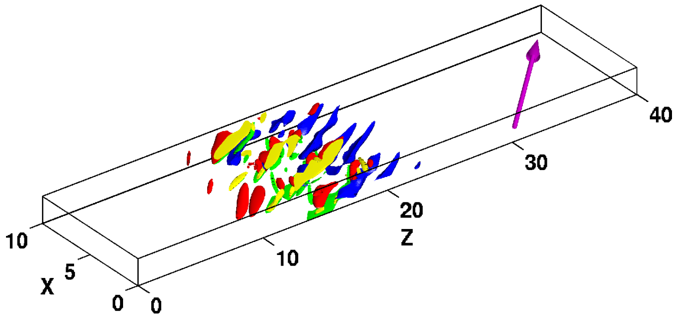

(c) Turbulent stripe at $Re = 750$. The isovalues : Streamwise velocity (red and blue) ± 0.26 and Streamwise vorticity (green and yellow) ± 1.1

Figure 5.7: Figure shows the (a) Traveling wave at its saddle-node bifurcation at $Re = 370.59$ (b) periodic orbit at $Re = 395$. It does not have any additional spatial symmetries and repeats itself with a period of $T = 10.93$. These localized structures are composed of low and high-speed streaks (blue and red resp.) and clockwise and counter-clockwise streamwise vortices (green and yellow). (c) Turbulent stripe at $Re = 750$ show the structural components like low and high-speed streaks and streamwise vortices like relative periodic orbit and the traveling wave solutions. The arrow shows the mean flow direction.

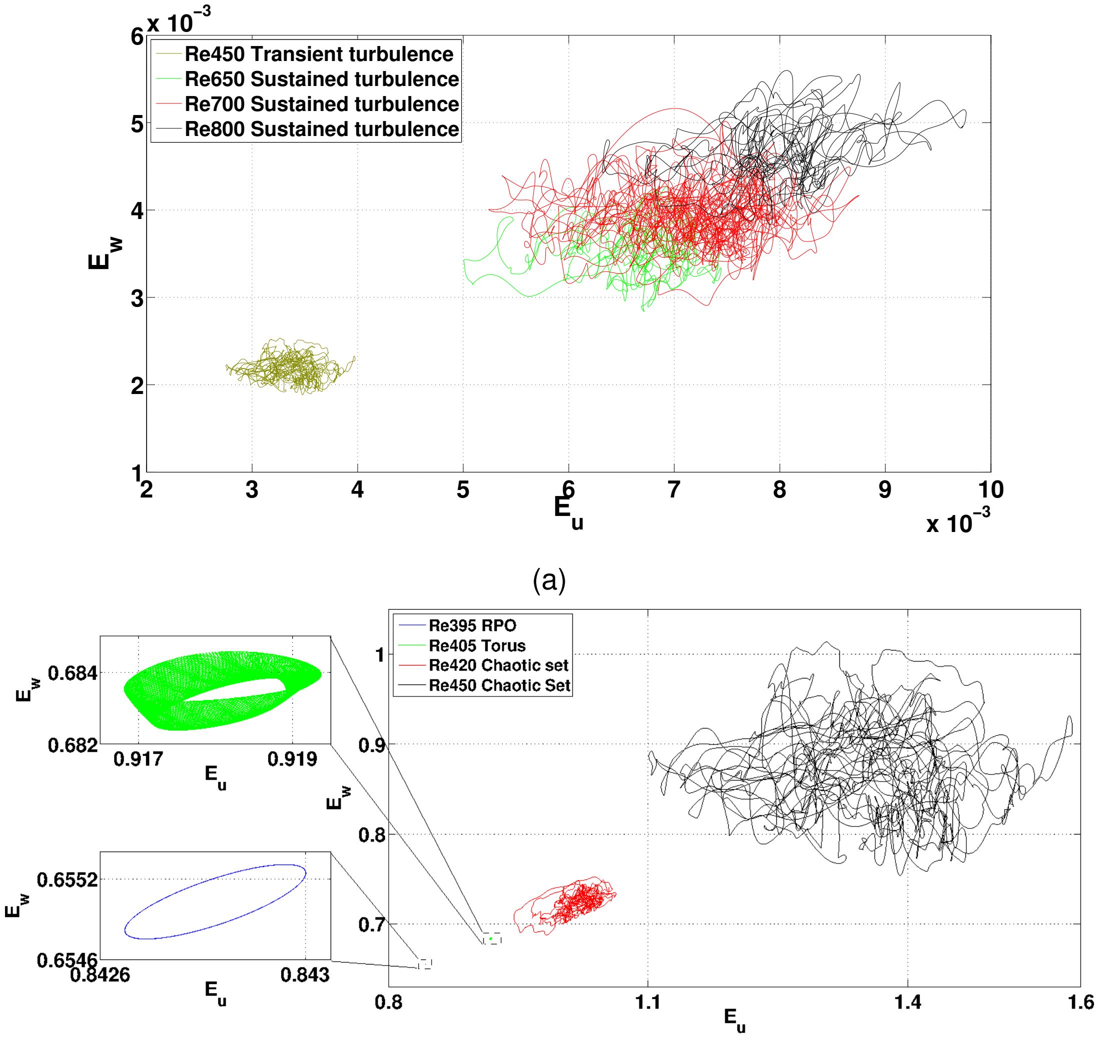

(a)

(b)

Figure 5.8: Phase portraits of different attracting and non-attracting sets at multiple values of Re on $E_u - E_w$ plane. (a) As Re reduces the size of the attractor also starts reducing. The chaotic set at $Re = 450$ is considerably smaller in size than that of at $Re = 650$. The mean energy also reduces with Re. (b) The chaotic set shrinks substantially between $Re = 450$ and 420. At $Re = 406$, the attractor is 2-Torus with a size order of magnitude smaller than that of $Re = 420$. RPO at $Re = 395$ is tiny and order of magnitude smaller than the torus

As Re is reduced, the mean temporal kinetic energy and the size of the chaotic sets reduce, as shown in Figure 5.8. The fluctuations at $Re = 450$ is almost 4 times smaller than that of $Re = 600$. The fluctuation levels drop considerably as Re reduces below 450 as can be seen from Figure 5.8b. For example, at $Re = 420$, the dynamics are still chaotic, but the fluctuations are an order of magnitude smaller now as compared to $Re = 450$. Similarly, the attractor size i.e., the fluctuation amplitude shrinks further as the attractor transforms from chaotic to 2-Torus to RPO. Figure 5.9 shows the fluctuation amplitudes for different attractors in $Re \in (393, 418)$. Interestingly, as 2-Torus turns into a chaotic attractor with multi-mode oscillations, the fluctuation amplitude jumps drastically.

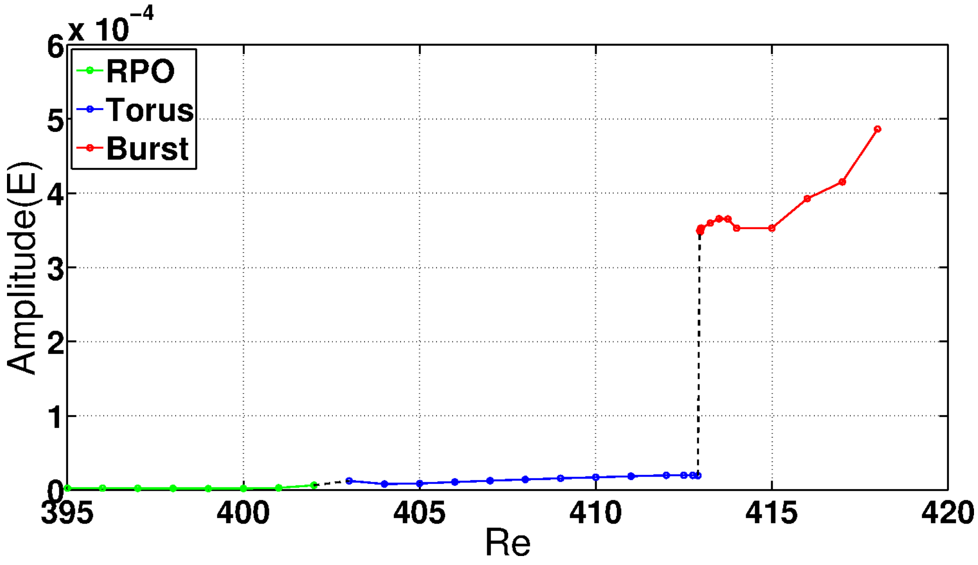

Figure 5.9: The amplitude of the attractor in perturbation kinetic energy E with Re. The amplitudes of attractor increase rapidly when the torus bifurcates into an attractor characterized by multi-mode oscillations.

5.4 Time series analysis and correlation dimension

Chaotic attractors are multi-dimensional complex objects. The dimensions of a chaotic attractor can be estimated using box-counting. However, this method only works reliably if the dimension is not too high.

The more straightforward way of characterizing the attractor is through the time-series of some scalar quantity obtained from chaotic dynamics. We use the method suggested by Grassberger-Procaccia in 1983 [Grassberger and Procaccia, 1983b],[Grassberger and Procaccia, 1983a] for the analysis of the time-series. It computes a particular correlation dimension of the attractor from the time-series. The details of the Grassberger-Procaccia algorithm and the implementation has been discussed in further subsections.

5.4.1 Delay coordinates

Consider a dynamical system $\dot{\boldsymbol{x}} = f(\boldsymbol{x})$. Let $\triangle t$ be a discrete timestep used for the computation and $y_n = y(\boldsymbol{x}_n)$ be some scalar observable. Then a sequence $\{y_n\}$ is a discrete timeseries of that scalar computed at every interval of $\triangle t$. The timeseries itself does not directly give the information about the dimensionality of the attractor. But by 'unfolding' the timeseries using the delay coordinates, the dimensionality can be extracted.

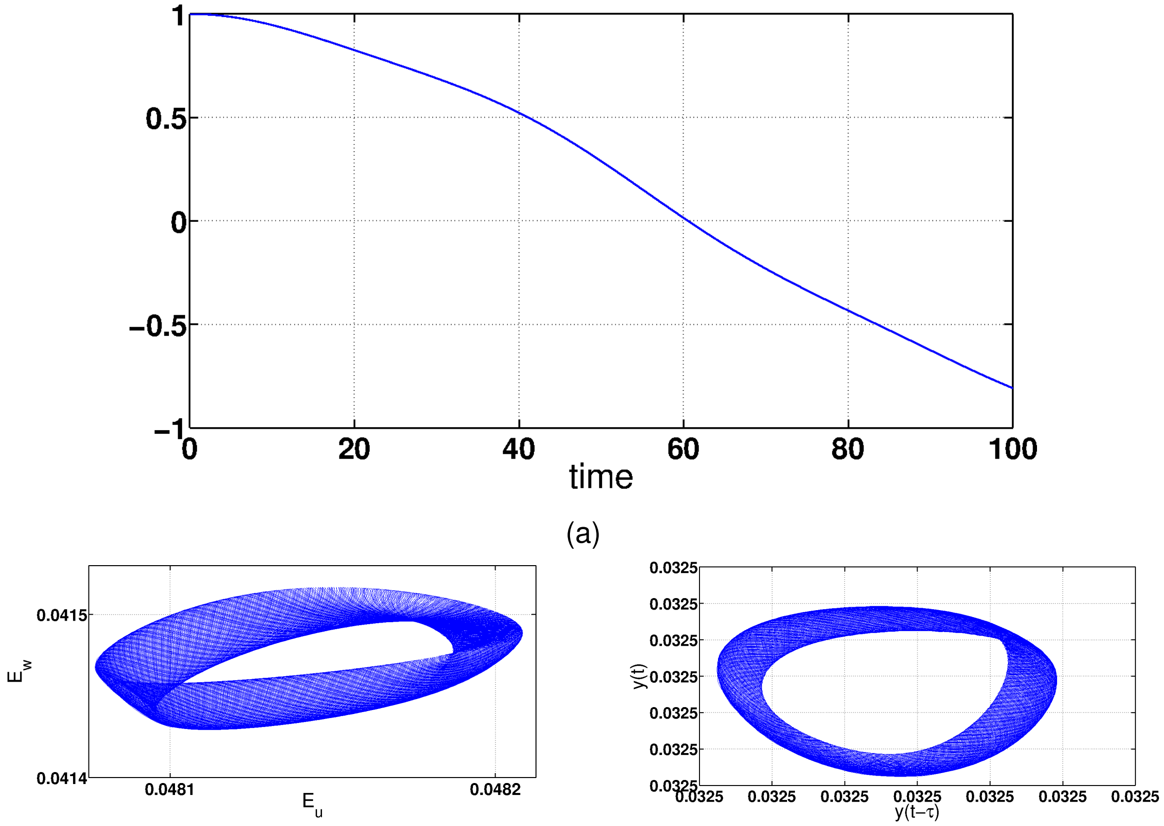

(a)

(b)

(c)

Figure 5.10: Comparison between the phase portrait and the reconstructed attractor. The topology of the attractor is maintained in the reconstructed version. (a)The autocorrelation of the time-series at $Re = 407$. The autocorrelation function has its first zero at $\tau = 60$. This τ is used as the delay for the reconstruction of the phase space of the attractor from the time-series of the scalar y_n. *b) The phase portrait at $Re = 407$. The high dimensional dynamics is projected on E_u and E_w plane where E_u and E_w are kinetic energy in x and z direction of the rectangular numerical domain. The attractor is a 2-Torus. (c)The reconstructed phase portrait at $Re = 407$ from the time-series of the global kinetic energy of the flow, with the embedding dimension $m = 2$. The phase portrait is reconstructed with the delay vectors $\boldsymbol{y}_n = (y_{n-\tau}, y_n)$ where delay time $\tau = 60$ i.e. first zero of the corresponding autocorrelation function.

Let τ be a time delay and m be the dimension of the embedding space. Then a vector in the m-dimensional embedding space is constructed as

$$\boldsymbol{y}_n = (y_{n-(m-1)\tau}, y_{n-(m-2)\tau}, ...y_n) \tag{5.1}$$

These vectors can reconstruct the phase space with one to one correspondence [Takens, 1981]. If there are N samples of scalar y_n available then for m embedding dimensions, there are $N - (m - 1)\tau$ embedding vectors $\boldsymbol{y}_n$. Usually, the delay time is chosen as the first zero of the autocorrelation function of the time-series. Figure 5.10c shows the reconstructed phase portrait constructed from the time-series of the dynamics at $Re = 407$. The time-series represents the kinetic energy of fluctuations computed at each time step. The delay vector is formed by using delay time $\tau = 60$ as it is the first zero of the autocorrelation function. The original phase portrait in Figure 5.10b is constructed from the two scalar observables viz. E_u and E_w. The reconstructed attractor (Figure 5.10c) maintains the qualitative shape of the attractor.

5.4.2 Correlation dimension

Let ϵ be a ball of size r which covers a part of the attractor. Let $p(r)$ be some weight which corresponds to the part of the attractor covered by this ϵ-ball. This quantity $p(r)$ scales with the radius of the ϵ-ball as

$$p(r) \approx r^D \tag{5.2}$$

Where D is the "dimension" of the attractor, which depends on the definition of the weight $p(r)$.

This weight is defined as a correlation sum. This correlation sum, for any ball of radius r, any embedding dimension m, and any scalar $r > 0$ is defined as :

$$C(m,r) = \frac{1}{N_{pairs}} \sum_{j=1}^{N} \sum_{k<j-\omega} \Theta(r - |\boldsymbol{y}_j - \boldsymbol{y}_k|) \tag{5.3}$$

where $N_{pairs} = (N - m + 1)(N - m - w + 1)/2$, Θ is the Heaviside step function, $\{\boldsymbol{x}_i\}$ the time-delay vector in space with embedding dimension m. It is necessary to omit the temporally correlated pairs i.e., "false neighbours" from the correlation sum for the correct estimation of D_2. In order to remove highly correlated pairs, we use ω as a Theiler window, i.e., a positive integer such that all the pairs below that number are omitted [Theiler, 1990]. Usually, the Theiler window is selected as $\sim 1.5\tau$, where τ is the first zero of the correlation function. Then $C(m,r)$ and r is plotted in a log-log plot, and the slope is calculated in the range of r where the curve is a straight line on the log-log plot. It gives us the estimation of D_2 such that

$$C(m,r) \propto r^{D_2} \tag{5.4}$$

D_2 is computed for the attractor unfolded in m^{th} embedding dimension where $m = 1, 2, 3....$ Then the value where D_2 converges, is called as the correlation dimension of the attractor (see Figure 5.11).

For a correct estimation of D_2, the time series must be long enough. Typically the relation of the length of the time-series (sampling points N) and the correlation

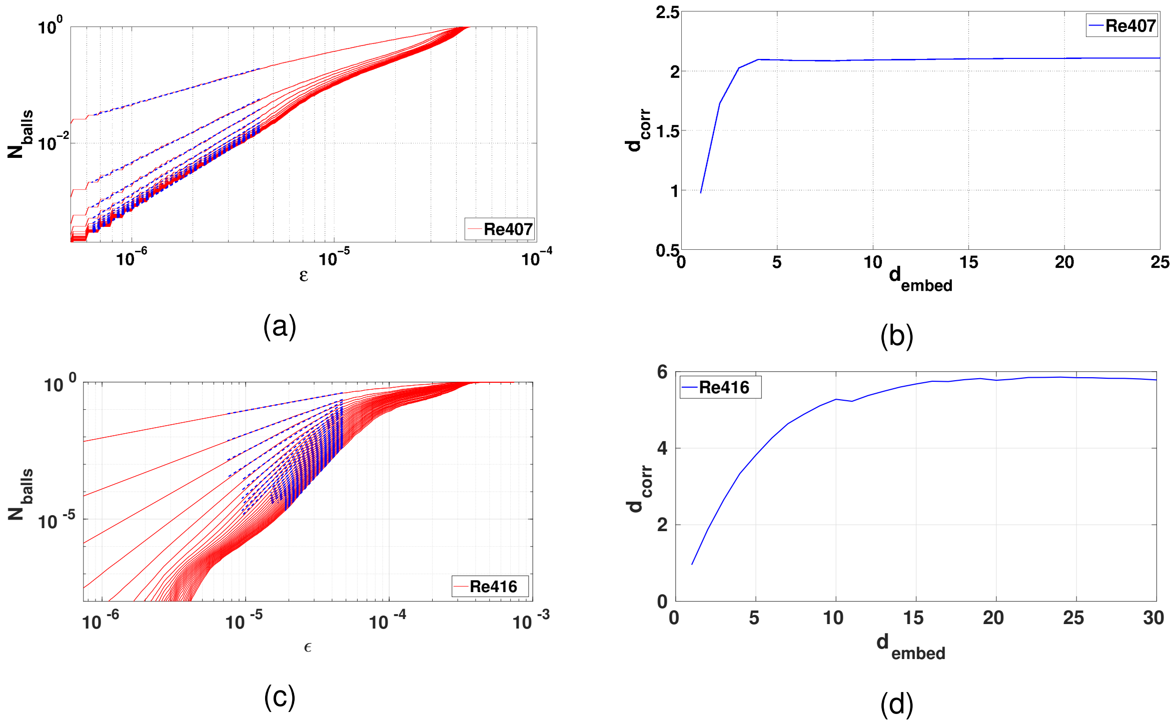

(a) (b) (c) (d)

Figure 5.11: Correlation dimension and embedding dimension of attractors. (a) and (c) The correlation sum $C(m,r)$ vs. the $\epsilon - ball$ of size r for the attractor at $Re = 407$ and $Re = 416$ respectively. The attractor in (a) is a 2-Torus and in (c) is chaotic. The different curves are for different values of embedding dimensions m. The slope of these curves on log-log plots (blue straight lines) represent D_2. (b) and (d) D_2 vs. embedding dimension m. The correlation dimension i.e. the slope of the curve $C(m,r)$ against the ball radius r on log log plot converges as m increases. The converged value of D_2 is the correlation dimension of the attractor. The correlation dimension for 2-Torus is $D_2 \sim 2$ and for chaotic attractor is $D_2 \sim 6$.

dimension is $D_2 \sim 2\log_{10} N$ [Eckmann and Ruelle, 1992] i.e. $N_{needed} > 10^{D_2/2}$. For example, the length of the time-series used to determine the correlation dimension of an attractor at $Re = 420$ is 92500 time units with the total number of sampling points 370000. The estimation of D_2 for the corresponding attractor is ~ 8. Therefore, the number of data points needed to estimate the dimension correctly is at least ~ 10000. However, as the complexity of the attractor increases, one needs longer and longer time-series for the correct estimation of the correlation dimension of the attractor.

We used the package ***TISEAN*** for the computation of the correlation dimension [Hegger *et al.*, 1999],[Hegger *et al.*, 2007].

5.4.3 Correlation dimension of attractors of stripes

We computed the correlation dimension of the attractors for $Re \in [395, 420]$. In this range, the attractor evolves from RPO to Torus and then to a chaotic attractor. The attractor is a relative periodic orbit for $Re \in [395, 403]$. The correlation dimension for the RPO is $D_2 \approx 1$. Then as stated in the previous sections, the attractor undergoes Neimark-Sacker bifurcation, and in the range, $Re \in [404, 412]$ the attractor is a 2-Torus with the correlation dimension $D_2 \approx 2$. At $Re_c = 413$, the attractor becomes chaotic, and this Re_c is marked as a Reynolds number at the onset of the chaos. For the attractor at $Re > RE_c$ the correlation dimension increases rapidly and at $Re = 420$, the dimension is $D_2 \approx 8$ (see the inset in Figure 5.12).

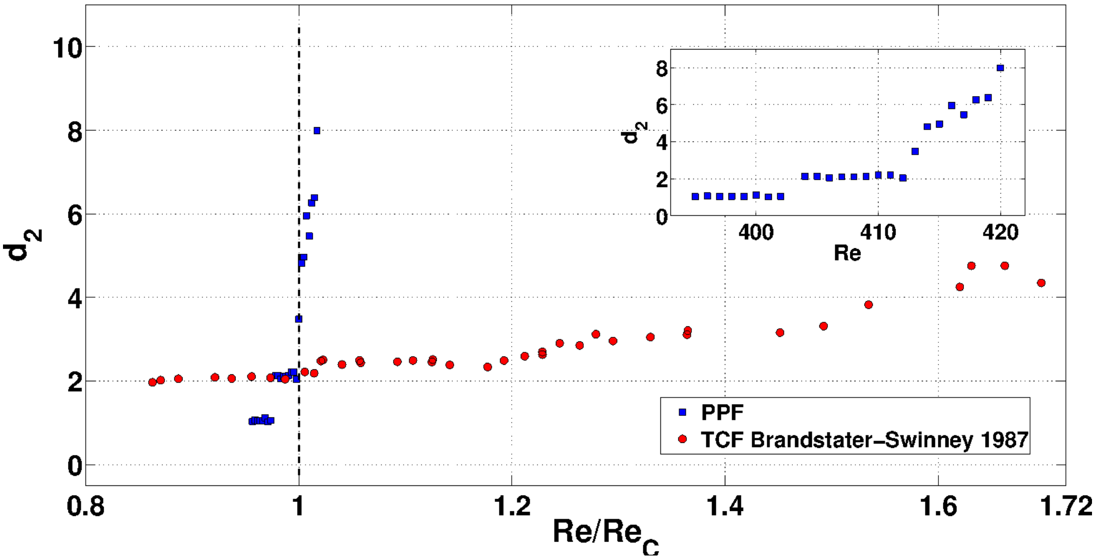

Figure 5.12: The correlation dimension is computed from the kinetic energy time series at the respective Reynolds numbers for channel flow (blue data set). Re_c denotes the critical point for the onset of chaos $Re = 413$. The dimension is one when the dynamics fall onto a limit cycle and two for the torus and ¿2 for chaos. For comparison, we show data for the transition to turbulence in Taylor Couette flow (Red). In the latter case (like in other linearly unstable flows) the complexity of the flow increases slowly as the Reynolds number is increased. After a Reynolds number increase by 60%, the dimension approaches a value of 4. In contrast, in channel flow, a Reynolds number increase by about 1% is sufficient to reach the same dimension.

5.5 Discussions

We compared the evolution of the correlation dimension in the PPf with the dynamics of the Taylor-Couette system with only the inner cylinder rotating. This data is from Brandstater and Swinney [Brandstater and Swinney, 1987]. This latter scenario is typical for flows where the route to chaos starts from a linear instability of the laminar base flow. We speculate that the difference between the two scenarios is rooted in the spatial complexity of the problems at hand. In Taylor-Couette flow, a global mode arises smoothly from the laminar state, and the resulting Taylor vortex flow is structurally far from turbulence. The development of turbulence is slow and only takes place over an extensive range of velocity. Consecutive instabilities gradually increase the spatial complexity as well as the temporal disorder - aspects that are consistent with Landau's view of a stepwise development towards turbulence.

In contrast, in channel flow, the starting point is a temporally laminar solution that has the structural complexity of a low Re turbulence inbuilt. The spatial localization and its nonlinear nature make this turbulent nucleus prone to instability and rationalize the rapid break down encountered for increasing Re. Being governed by the Navier-Stokes equations turbulence in principle is deterministic, yet in practice, the strong disorder in space and time necessitates a statistical treatment. The sharp increase in the attractor dimension identified here marks the border up to which a deterministic treatment is suitable whereas above statistical mechanics descriptions become more appropriate, setting the stage for the non-equilibrium phase transition [Avila *et al.*, 2011; Lemoult *et al.*, 2016] encountered at larger Re.

6 Summary

Like in many other wall-bounded shear flow, turbulence in plane Poiseuille flow (PPf) emerges despite the laminar base flow being linearly stable. Characteristic for these flows is that turbulence at onset is spatio-temporally intermittent. In planar flows like channel flow, turbulence appears in the form of localized stripes oblique to the mean flow direction. The understanding of the nature of subcritical turbulence is far from complete. The present work combines experiments, direct numerical simulations, and applies concepts from dynamical system theory to further elucidate this transition type for the case of channel flow.

6.1 Experiments in channel flow

In the experiments, we focused on determining the critical point where turbulence first becomes sustained. The experiments were carried out in a large aspect ratio channel. We found that at the onset, the natural angle of the stripe i.e., the angle made by the stripe with the mean flow direction is $45°$. As Re increases, this angle reduces. However, in the vicinity of the critical point, the natural angle remains $45°$.

The turbulent stripes multiply in numbers by two mechanisms: splitting and branching. In branching, a new stripe starts from a parent stripe which grows in the symmetrically opposite direction than the parent stripe. This mechanism is responsible for forming the characteristic criss-cross stripe patterns in transitional channel flow. In splitting, a new stripe is formed upstream of a parent stripe, and it maintains the same orientation as the parent stripe. The new stripe nucleates from the shed streaky patches from the tail of the parent stripe. At $Re > 950$, both branching and splitting mechanisms play an important role in the formation of new stripes. However, near onset, only the splitting is a relevant mechanism, and practically no branching event is observed.

To estimate the critical point, we first measured the mean growth rate of the turbulent fraction with Re. The growth rate first becomes positive at $Re \approx 670$. Apart from stripe splitting, that causes an increase in the stripe number, the growth of individual stripes is essential for turbulence to become sustained.

A single stripe shrinks or expands as a result of a competition between two key mechanisms: growth at the tip due to the continuous addition of new streaks and intermittent decay of streaky patches from the tail. In addition to the extension/shrinkage of the stripes, these mechanisms also result in spanwise advection of turbulent stripe as they travel downstream. The expansion of the stripe due to the tip growth and the tail decay balances at $Re \approx 660$ and individual stripes start expanding above this value. However, interestingly, at any particular Re the splitting and the decay probabilities depend on the length of the stripe. For larger stripe length, the probability of the collapse is smaller than that of the shorter stripe. However, the probability of the splitting increases with increasing stripe length. This dependence of the splitting and the decay probabilities on the stripe length shows that unlike puff splitting and the puff decay in pipe flow, these processes are not memoryless.

The critical point reported here is considerably lower than those reported in most earlier studies. However, we can not comment on any universality class of the transition as the study is inadequate in that respect.

6.2 Bifurcation of turbulent stripes in PPf

In the second part of the thesis, we carried out direct numerical simulations of Poiseuille flow and applied dynamical systems concepts. We identified spatially localized invariant solutions that can be regarded as the precursors of turbulent stripes. In experiments, it is observed that the turbulent stripes are tilted with respect to the mean flow direction. In our numerical study, the domain was tilted matching the angles that are typically observed in experiments. The invariant solutions at a particular tilt angle determined using a bisection method correspond to lower branch traveling wave solutions.

First, we report a family of these TWs at different tilt angles. The origins of the solution branches in the family in Re are studied by continuing LBTWs in parameter space parametrized by Re to their saddle-node bifurcation points. All the solutions are unstable, with multiple unstable eigenvalues near the saddle-node points. The value of Re for saddle-node bifurcations for different tilt angles are different with the minimum value of $Re_{SN} = 370$ at $\theta = 45°$. Starting from the saddle-node points, as Re increases, the LBTWs start losing unstable eigenvalues and finally become edge states with only one unstable eigenvalue. The UBTWs, on the other hand, become more and more unstable as Re increases. The change in the stability of LBTWs happens due to Hopf bifurcations. Again, for the solution branches at different values of the tilt angles, the Hopf bifurcation point Re_H is different. The RPOs which emerge through the Hopf bifurcations have distinct periods for distinct tilt angles. Unlike many other bifurcation studies, it is the instabilities of the lower branches from which routes to chaos start. Also, as these solutions are nonlinear, new solutions can not be created by just adding different solutions. Therefore it can be argued that different routes to chaos coexist for different values of the stripe tilt angle θ. One example of a route to chaos is reported for $\theta = 35°$.

In addition, we performed parametric studies on LBTWs with parameters θ and domain size L_x. Continuing LBTWs in θ gives a subset of tilt angle values for which these TW solutions can appear. At the lowest value of Re at which a TW solution in the computational domain exists, the tilt angle is $45°$. As Re increases, the subset of θ in which the solutions exist also increase and at $Re = 700$, the solutions can exist for $\theta \in (20°, 70°)$.

For studying the effects of varying domain size on the TWs, in a direction where the stripes are not localized direction, i.e., L_x, we chose $45°$ as the tilt angle, based on the fact that at this tilt angle, TW solution exists at the lowest value of Re. As L_x changes, so does the wavelength of the streaks. Continuing the solutions in other parameter i.e. Re, it is observed that a local minimum for Re_{SN} is found around 367 and occurs for $L_x = 3.2$.

6.3 Deterministic origin of turbulent stripes

At onset, turbulence appears on multiple scales in space and time. However, the transient nature of turbulence makes it difficult to track to lower Re. Here, we successfully showed that the turbulent stripes could be traced down to their dynamically simpler origins. Using a rectangular domain tilted at an angle 45° - which is a natural angle of the stripes at onset, we adiabatically reduce Re and trace the localized turbulent stripes beyond the relaminarization barrier. It is observed that the turbulent stripes, although transient, exhibit lifetimes large enough to allow a gradual reduction in Re. As Re reduces the mean fluctuation energy and the amplitude of the fluctuations also reduces. At $Re < 426$ the chaotic set becomes an attractor through a boundary crisis and simplifies to a 2-Torus in a range $Re \in (403.5, 412.9)$. Further reduction in Re simplifies the 2-torus into an RPO below $Re < 403.5$. This RPO emerges from a Hopf bifurcation of the lower branch of traveling wave solution at $Re = 387.6$. This TW itself emerges in the saddle-node bifurcation at $Re = 370.6$.

The chaotic sets were then characterized by computing correlation dimensions. We compared the evolution of the correlation dimension with Re with Taylor Couette flow (TCf) with only inner cylinder rotation [Brandstater and Swinney, 1987]. In that case, turbulence arises through the instabilities of the laminar base flow, unlike the subcritical turbulence in PPf. In TCf, turbulence develops slowly over an extensive range of Re as global mode instabilities gradually increase spatial complexity and temporal disorder. However, in PPf turbulence originates from a temporally laminar flow with the inbuilt structural complexity of a low Re turbulence. The nucleus of the turbulent stripes quickly becomes unstable wit increasing Re and attractor dimension increase sharply. The high dimensions suggest that the deterministic treatment to turbulence is of limited use at larger Re and the statistical mechanics approach is more appropriate than the deterministic approach.

6.4 Future work

The present experiments are inadequate in commenting on the universality class of the transition to turbulence [Pomeau, 1986]. Further work is necessary in order to study the transition in more detail at and around the critical point $Re = 670$. The effects of multiple interacting stripes on the critical point are also necessary to investigate. Such a study is experimentally challenging due to the long timescales involved, and the advection of stripes in the streamwise as well as in the spanwise direction limits the observation times. Computational studies, on the other hand, will require simulations in very large domains.

In the above, a phenomenological description of splitting and branching of the turbulent stripes and relation of splitting events with Re has been reported. However, the underlying mechanisms in detail are still not well-understood. As Re increases, first the stripe splitting kicks in and later, with further increase in the flow rate the branching also starts. It will be interesting to examine the role of the secondary flow in shaping these mechanisms.

The mechanism behind the angle selection of the stripes is also not well understood. In experiments, the natural angle of the stripes does not increase beyond $45°$. However, the underlying TW solutions exist at values of angle above that. The explanation behind the angle selection may lie in the secondary flow around the stripes.

The dynamically simple stripe solutions such as TWs and RPOs can be probed further to understand the localization of the stripes and to shed more light on how this localized turbulence sustains. In the above, we studied the invariant stripe solutions localized only in one direction. The next step will be to identify the doubly localized invariant stripe solutions. Such solutions will be more similar to the stripes observed in experiments and therefore may provide further vital insights into the genesis of the stripes.

Bibliography

[Aida *et al.*, 2011] Hiroshi Aida, Takahiro Tsukahara, and Yasuo Kawaguchi, "Development of a turbulent spot into a stripe pattern in plane Poiseuille flow," In *TSFP DIGITAL LIBRARY ONLINE*. Begel House Inc., 2011.

[Alavyoon *et al.*, 1986] Farid Alavyoon, Dan S Henningson, and P Henrik Alfredsson, "Turbulent spots in plane Poiseuille flow–flow visualization," *The Physics of fluids*, 29(4):1328–1331, 1986.

[Avila *et al.*, 2011] Kerstin Avila, David Moxey, Alberto de Lozar, Marc Avila, Dwight Barkley, and Björn Hof, "The onset of turbulence in pipe flow," *Science*, 333(6039):192–196, 2011.

[Avila *et al.*, 2013] Marc Avila, Fernando Mellibovsky, Nicolas Roland, and Bjoern Hof, "Streamwise-localized solutions at the onset of turbulence in pipe flow," *Physical review letters*, 110(22):224502, 2013.

[Avila *et al.*, 2010] Marc Avila, Ashley P Willis, and Björn Hof, "On the transient nature of localized pipe flow turbulence," *Journal of Fluid Mechanics*, 646:127–136, 2010.

[Barkley *et al.*, 2015] Dwight Barkley, Baofang Song, Vasudevan Mukund, Grégoire Lemoult, Marc Avila, and Björn Hof, "The rise of fully turbulent flow," *Nature*, 526(7574):550, 2015.

[Barkley and Tuckerman, 2005] Dwight Barkley and Laurette S Tuckerman, "Computational study of turbulent laminar patterns in Couette flow," *Physical review letters*, 94(1):014502, 2005.

[Barkley and Tuckerman, 2007] Dwight Barkley and Laurette S Tuckerman, "Mean flow of turbulent–laminar patterns in plane Couette flow," *Journal of Fluid Mechanics*, 576:109–137, 2007.

[Borrero-Echeverry *et al.*, 2010] Daniel Borrero-Echeverry, Michael F Schatz, and Randall Tagg, “Transient turbulence in Taylor-Couette flow,” *Physical Review E*, 81(2):025301, 2010.

[Bottin and Chaté, 1998] Sabine Bottin and Hugues Chaté, “Statistical analysis of the transition to turbulence in plane Couette flow,” *The European Physical Journal B-Condensed Matter and Complex Systems*, 6(1):143–155, 1998.

[Bottin *et al.*, 1998a] Sabine Bottin, Olivier Dauchot, Francois Daviaud, and Paul Manneville, “Experimental evidence of streamwise vortices as finite amplitude solutions in transitional plane Couette flow,” *Physics of Fluids*, 10(10):2597–2607, 1998.

[Bottin *et al.*, 1998b] Sabine Bottin, Francois Daviaud, Paul Manneville, and Olivier Dauchot, “Discontinuous transition to spatiotemporal intermittency in plane Couette flow,” *EPL (Europhysics Letters)*, 43(2):171, 1998.

[Brand and Gibson, 2014] Evan Brand and John F Gibson, “A doubly localized equilibrium solution of plane Couette flow,” *Journal of Fluid Mechanics*, 750, 2014.

[Brandstater and Swinney, 1987] Anke Brandstater and Harry L Swinney, “Strange attractors in weakly turbulent Couette-Taylor flow,” *Physical Review A*, 35(5):2207, 1987.

[Canuto, 1988] C. Canuto, *Spectral methods in fluid dynamics*, Springer series in computational physics. Springer-Verlag, 1988.

[Carlson *et al.*, 1982] Dale R Carlson, Sheila E Widnall, and Martin F Peeters, “A flow-visualization study of transition in plane Poiseuille flow,” *Journal of Fluid Mechanics*, 121:487–505, 1982.

[Chantry *et al.*, 2017] Matthew Chantry, Laurette S Tuckerman, and Dwight Barkley, “Universal continuous transition to turbulence in a planar shear flow,” *Journal of Fluid Mechanics*, 824, 2017.

[Cliffe *et al.*, 2012] KA Cliffe, T Mullin, and D Schaeffer, “The onset of steady vortices in Taylor-Couette flow: The role of approximate symmetry,” *Physics of Fluids*, 24(6):064102, 2012.

[Coles, 1965] Donald Coles, "Transition in circular Couette flow," *Journal of Fluid Mechanics*, 21(3):385–425, 1965.

[Cooper and Dooley, 2008] JR Cooper and RB Dooley, "Release of the IAPWS formulation 2008 for the viscosity of ordinary water substance," *The International Association for the Properties of Water and Steam*, 2008.

[Cros and Le Gal, 2002] A Cros and P Le Gal, "Spatiotemporal intermittency in the torsional Couette flow between a rotating and a stationary disk," *Physics of Fluids*, 14(11):3755–3765, 2002.

[Cvitanović, 1988] Predrag Cvitanović, "Invariant measurement of strange sets in terms of cycles," *Physical Review Letters*, 61(24):2729, 1988.

[Darbyshire and Mullin, 1995] AG Darbyshire and T Mullin, "Transition to turbulence in constant-mass-flux pipe flow," *Journal of Fluid Mechanics*, 289:83–114, 1995.

[Dauchot and Daviaud, 1995] Olivier Dauchot and Francois Daviaud, "Finite amplitude perturbation and spots growth mechanism in plane Couette flow," *Physics of Fluids*, 7(2):335–343, 1995.

[Davies *et al.*, 1928] SJ Davies, CM White, *et al.*, "An experimental study of the flow of water in pipes of rectangular section," *Proc. R. Soc. Lond. A*, 119(781):92–107, 1928.

[De Lozar *et al.*, 2012] Alberto De Lozar, F Mellibovsky, M Avila, and Björn Hof, "Edge state in pipe flow experiments," *Physical review letters*, 108(21):214502, 2012.

[Drazin and Reid, 2004] Philip G Drazin and William Hill Reid, *Hydrodynamic stability*, Cambridge university press, 2004.

[Duguet *et al.*, 2011] Yohann Duguet, Olivier Le Maitre, and Philipp Schlatter, "Stochastic and deterministic motion of a laminar-turbulent front in a spanwisely extended Couette flow," *Physical Review E*, 84(6):066315, 2011.

[Duguet *et al.*, 2008] Yohann Duguet, Chris CT Pringle, and Rich R Kerswell, "Relative periodic orbits in transitional pipe flow," *Physics of fluids*, 20(11):114102, 2008.

[Duguet and Schlatter, 2013] Yohann Duguet and Philipp Schlatter, “Oblique laminar-turbulent interfaces in plane shear flows,” *Physical review letters*, 110(3):034502, 2013.

[Duguet *et al.*, 2009] Yohann Duguet, Philipp Schlatter, and Dan S Henningson, “Localized edge states in plane Couette flow,” *Physics of fluids*, 21(11):111701, 2009.

[Duguet *et al.*, 2010a] Yohann Duguet, Philipp Schlatter, and Dan S Henningson, “Formation of turbulent patterns near the onset of transition in plane Couette flow,” *Journal of Fluid Mechanics*, 650:119–129, 2010.

[Duguet *et al.*, 2010b] Yohann Duguet, AP Willis, and RR Kerswell, “Slug genesis in cylindrical pipe flow,” *Journal of Fluid Mechanics*, 663:180–208, 2010.

[Eckert, 2007] Michael Eckert, *The dawn of fluid dynamics: a discipline between science and technology*, John Wiley & Sons, 2007.

[Eckhardt *et al.*, 2007] Bruno Eckhardt, Tobias M Schneider, Bjorn Hof, and Jerry Westerweel, “Turbulence transition in pipe flow,” *Annu. Rev. Fluid Mech.*, 39:447–468, 2007.

[Eckmann and Ruelle, 1992] J-P Eckmann and David Ruelle, “Fundamental limitations for estimating dimensions and Lyapunov exponents in dynamical systems,” *Physica D: Nonlinear Phenomena*, 56(2-3):185–187, 1992.

[Ehrenstein and Koch, 1991] U Ehrenstein and W Koch, “Three-dimensional wavelike equilibrium states in plane Poiseuille flow,” *Journal of fluid mechanics*, 228:111–148, 1991.

[Faisst and Eckhardt, 2003] Holger Faisst and Bruno Eckhardt, “Traveling waves in pipe flow,” *Physical Review Letters*, 91(22):224502, 2003.

[Faisst and Eckhardt, 2004] Holger Faisst and Bruno Eckhardt, “Sensitive dependence on initial conditions in transition to turbulence in pipe flow,” *Journal of Fluid Mechanics*, 504:343–352, 2004.

[Feigenbaum, 1979] Mitchell J Feigenbaum, “The onset spectrum of turbulence,” *Physics Letters A*, 74(6):375–378, 1979.

[Gibson, 2014] J. F. Gibson, “Channelflow: A spectral Navier-Stokes simulator in C++,” Technical report, U. New Hampshire, 2014, `Channelflow.org`.

[Gibson and Brand, 2014] John F Gibson and Evan Brand, “Spanwise-localized solutions of planar shear flows,” *Journal of Fluid Mechanics*, 745:25–61, 2014.

[Gibson *et al.*, 2008] John F Gibson, Jonathan Halcrow, and Predrag Cvitanović, “Visualizing the geometry of state space in plane Couette flow,” *Journal of Fluid Mechanics*, 611:107–130, 2008.

[Gibson *et al.*, 2009] John F Gibson, Jonathan Halcrow, and Predrag Cvitanović, “Equilibrium and travelling-wave solutions of plane Couette flow,” *Journal of Fluid Mechanics*, 638:243–266, 2009.

[Gollub and Swinney, 1975] Jerry P Gollub and Harry L Swinney, “Onset of turbulence in a rotating fluid,” *Physical Review Letters*, 35(14):927, 1975.

[Grassberger, 1982] Peter Grassberger, “On phase transitions in Schlögl’s second model,” *Zeitschrift für Physik B Condensed Matter*, 47(4):365–374, 1982.

[Grassberger and Procaccia, 1983a] Peter Grassberger and Itamar Procaccia, “Characterization of strange attractors,” *Physical review letters*, 50(5):346, 1983.

[Grassberger and Procaccia, 1983b] Peter Grassberger and Itamar Procaccia, “Measuring the strangeness of strange attractors,” *Physica D: Nonlinear Phenomena*, 9(1-2):189–208, 1983.

[Grossmann, 2000] Siegfried Grossmann, “The onset of shear flow turbulence,” *Reviews of modern physics*, 72(2):603, 2000.

[Halcrow *et al.*, 2009] Jonathan Halcrow, John F Gibson, Predrag Cvitanović, and Divakar Viswanath, “Heteroclinic connections in plane Couette flow,” *Journal of Fluid Mechanics*, 621:365–376, 2009.

[Hamilton *et al.*, 1995] James M Hamilton, John Kim, and Fabian Waleffe, “Regeneration mechanisms of near-wall turbulence structures,” *Journal of Fluid Mechanics*, 287:317–348, 1995.

[Hashimoto *et al.*, 2009] S Hashimoto, A Hasobe, Takahiro Tsukahara, Yasuo Kawaguchi, and Hiroshi Kawamura, "An experimental study on turbulent-stripe structure in transitional channel flow," In *ICHMT DIGITAL LIBRARY ONLINE*. Begel House Inc., 2009.

[Hegger *et al.*, 1999] Rainer Hegger, Holger Kantz, and Thomas Schreiber, "Practical implementation of nonlinear time series methods: The TISEAN package," *Chaos: An Interdisciplinary Journal of Nonlinear Science*, 9(2):413–435, 1999.

[Hegger *et al.*, 2007] Rainer Hegger, Holger Kantz, and Thomas Schreiber, "Tisean: Nonlinear time series analysis," 2007.

[Heisenberg, 1924] Werner Heisenberg, "Über Stabilität und Turbulenz von Flüssigkeitsströmen," *Annalen der Physik*, 379(15):577–627, 1924.

[Henningson and Alfredsson, 1987] Dan S Henningson and P Henrik Alfredsson, "The wave structure of turbulent spots in plane Poiseuille flow," *Journal of Fluid Mechanics*, 178:405–421, 1987.

[Hof *et al.*, 2008] Björn Hof, Alberto de Lozar, Dirk Jan Kuik, and Jerry Westerweel, "Repeller or attractor? Selecting the dynamical model for the onset of turbulence in pipe flow," *Physical review letters*, 101(21):214501, 2008.

[Hof *et al.*, 2004] Björn Hof, Casimir WH van Doorne, Jerry Westerweel, Frans TM Nieuwstadt, Holger Faisst, Bruno Eckhardt, Hakan Wedin, Richard R Kerswell, and Fabian Waleffe, "Experimental observation of nonlinear traveling waves in turbulent pipe flow," *Science*, 305(5690):1594–1598, 2004.

[Hof *et al.*, 2006] Björn Hof, Jerry Westerweel, Tobias M Schneider, and Bruno Eckhardt, "Finite lifetime of turbulence in shear flows," *Nature*, 443(7107):59, 2006.

[Hopf, 1948] Eberhard Hopf, "A mathematical example displaying features of turbulence," *Communications on Pure and Applied Mathematics*, 1(4):303–322, 1948.

[Ishida *et al.*, 2016] Takahiro Ishida, Yohann Duguet, and Takahiro Tsukahara, "Transitional structures in annular Poiseuille flow depending on radius ratio," *Journal of Fluid Mechanics*, 794, 2016.

[Itano and Toh, 2001] Tomoaki Itano and Sadayoshi Toh, "The dynamics of bursting process in wall turbulence," *Journal of the Physical Society of Japan*, 70(3):703–716, 2001.

[Janssen, 1981] Hans-Karl Janssen, "On the nonequilibrium phase transition in reaction-diffusion systems with an absorbing stationary state," *Zeitschrift für Physik B Condensed Matter*, 42(2):151–154, 1981.

[Jiménez and Moin, 1991] Javier Jiménez and Parviz Moin, "The minimal flow unit in near-wall turbulence," *Journal of Fluid Mechanics*, 225:213–240, 1991.

[Kawahara and Kida, 2001] Genta Kawahara and Shigeo Kida, "Periodic motion embedded in plane Couette turbulence: regeneration cycle and burst," *Journal of Fluid Mechanics*, 449:291–300, 2001.

[Kawahara *et al.*, 2012] Genta Kawahara, Markus Uhlmann, and Lennaert Van Veen, "The significance of simple invariant solutions in turbulent flows," *Annual Review of Fluid Mechanics*, 44:203–225, 2012.

[Kerswell, 2005] RR Kerswell, "Recent progress in understanding the transition to turbulence in a pipe," *Nonlinearity*, 18(6):R17, 2005.

[Knoll and Keyes, 2004] Dana A Knoll and David E Keyes, "Jacobian-free Newton–Krylov methods: a survey of approaches and applications," *Journal of Computational Physics*, 193(2):357–397, 2004.

[Kreilos, 2014] Tobias Kreilos, "Turbulence Transition in Shear Flows and Dynamical Systems Theory," Technical report, Philipps-Universität Marburg, 2014.

[Kreilos and Eckhardt, 2012] Tobias Kreilos and Bruno Eckhardt, "Periodic orbits near onset of chaos in plane Couette flow," *Chaos: An Interdisciplinary Journal of Nonlinear Science*, 22(4):047505, 2012.

[Lai and Tél, 2011] Ying-Cheng Lai and Tamás Tél, *Transient chaos: complex dynamics on finite time scales*, volume 173, Springer Science & Business Media, 2011.

[Landau, 1944] Lev D Landau, "On the problem of turbulence," In *Dokl. Akad. Nauk SSSR*, volume 44, pages 339–349, 1944.

[Lemoult *et al.*, 2012] Grégoire Lemoult, Jean-Luc Aider, and José Eduardo Wesfreid, "Experimental scaling law for the subcritical transition to turbulence in plane Poiseuille flow," *Physical Review E*, 85(2):025303, 2012.

[Lemoult *et al.*, 2013] Grégoire Lemoult, Jean-Luc Aider, and José Eduardo Wesfreid, "Turbulent spots in a channel: large-scale flow and self-sustainability," *Journal of Fluid Mechanics*, 731, 2013.

[Lemoult *et al.*, 2014] Grégoire Lemoult, Konrad Gumowski, Jean-Luc Aider, and José Eduardo Wesfreid, "Turbulent spots in channel flow: an experimental study," *The European Physical Journal E*, 37(4):25, 2014.

[Lemoult *et al.*, 2016] Grégoire Lemoult, Liang Shi, Kerstin Avila, Shreyas V Jalikop, Marc Avila, and Björn Hof, "Directed percolation phase transition to sustained turbulence in Couette flow," *Nature Physics*, 12(3):254–258, 2016.

[Lin, 1945a] CC Lin, "On the stability of two-dimensional parallel flows. II. Stability in an inviscid fluid," *Quarterly of Applied Mathematics*, 3(3):218–234, 1945.

[Lin, 1945b] Chia-Chiao Lin, "On the stability of two-dimensional parallel flows. I. General theory," *Quarterly of Applied Mathematics*, 3(2):117–142, 1945.

[Lumley and Yaglom, 2001] John L Lumley and Akiva M Yaglom, "A century of turbulence," *Flow, Turbulence and Combustion*, 66(3):241–286, 2001.

[Manneville, 2011] Paul Manneville, "On the decay of turbulence in plane Couette flow," *Fluid Dynamics Research*, 43(6):065501, 2011.

[Maurer and Libchaber, 1979] J Maurer and A Libchaber, "Rayleigh-Bénard experiment in liquid helium; frequency locking and the onset of turbulence," *Journal de Physique Lettres*, 40(16):419–423, 1979.

[Mellibovsky *et al.*, 2009] Fernando Mellibovsky, Alvaro Meseguer, Tobias M Schneider, and Bruno Eckhardt, "Transition in localized pipe flow turbulence," *Physical review letters*, 103(5):054502, 2009.

[Meseguer and Trefethen, 2003] A Meseguer and Lloyd N Trefethen, "Linearized pipe flow to Reynolds number 107," *Journal of Computational Physics*, 186(1):178–197, 2003.

[Mullin, 2011] Thomas Mullin, "Experimental studies of transition to turbulence in a pipe," *Annual Review of Fluid Mechanics*, 43:1–24, 2011.

[Nagata, 1990] Masato Nagata, "Three-dimensional finite-amplitude solutions in plane Couette flow: bifurcation from infinity," *Journal of Fluid Mechanics*, 217:519–527, 1990.

[Nagata and Deguchi, 2013] Masato Nagata and K Deguchi, "Mirror-symmetric exact coherent states in plane Poiseuille flow," *Journal of Fluid Mechanics*, 735, 2013.

[Narayanan, 1968] MA Badri Narayanan, "An experimental study of reverse transition in two-dimensional channel flow," *Journal of Fluid Mechanics*, 31(3):609–623, 1968.

[Narayanan and Ramjee, 1969] MA Badri Narayanan and V Ramjee, "On the criteria for reverse transition in a two-dimensional boundary layer flow," *Journal of Fluid Mechanics*, 35(2):225–241, 1969.

[Narayanan and Narayana, 1967] Musiri Anantha Badri Narayanan and Thalakaveri Narayana, "Some studies on transition from laminar to turbulent flow in a two-dimensional channel," *Zeitschrift für angewandte Mathematik und Physik ZAMP*, 18(5):642–650, 1967.

[Neelavara *et al.*, 2017] Shreyas Acharya Neelavara, Yohann Duguet, and François Lusseyran, "State space analysis of minimal channel flow," *Fluid Dynamics Research*, 49(3):035511, 2017.

[Nishioka *et al.*, 1975] M Nishioka, Y Ichikawa, *et al.*, "An experimental investigation of the stability of plane Poiseuille flow," *Journal of Fluid Mechanics*, 72(4):731–751, 1975.

[Nishioka and Asai, 1985] Michio Nishioka and Masahito Asai, "Some observations of the subcritical transition in plane Poiseuille flow," *Journal of Fluid Mechanics*, 150:441–450, 1985.

[Orr, 1907] William M'F Orr, "The stability or instability of the steady motions of a perfect liquid and of a viscous liquid. Part II: A viscous liquid," In *Proceedings of the Royal Irish Academy. Section A: Mathematical and Physical Sciences*, pages 69–138. JSTOR, 1907.

[Orszag, 1971] Steven A Orszag, “Accurate solution of the Orr–Sommerfeld stability equation,” *Journal of Fluid Mechanics*, 50(4):689–703, 1971.

[Orszag and Patera, 1980] Steven A Orszag and Anthony T Patera, “Subcritical transition to turbulence in plane channel flows,” *Physical review letters*, 45(12):989, 1980.

[Park and Graham, 2015] Jae Sung Park and Michael D Graham, “Exact coherent states and connections to turbulent dynamics in minimal channel flow,” *Journal of Fluid Mechanics*, 782:430–454, 2015.

[Patel and Head, 1969] VC Patel and MR Head, “Some observations on skin friction and velocity profiles in fully developed pipe and channel flows,” *Journal of Fluid Mechanics*, 38(1):181–201, 1969.

[Peixinho and Mullin, 2006] J Peixinho and T Mullin, “Decay of turbulence in pipe flow,” *Physical review letters*, 96(9):094501, 2006.

[Peyret, 2010] R. Peyret, *Spectral Methods for Incompressible Viscous Flow*, Applied Mathematical Sciences. Springer New York, 2010.

[Pomeau, 1986] Yves Pomeau, “Front motion, metastability and subcritical bifurcations in hydrodynamics,” *Physica D: Nonlinear Phenomena*, 23(1-3):3–11, 1986.

[Prigent, 2001] Arnaud Prigent, *La spirale turbulente: motif de grande longueur d’onde dans les écoulements cisaillés turbulents*, PhD thesis, Université Paris Sud-Paris XI, 2001.

[Prigent *et al.*, 2003] Arnaud Prigent, Guillaume Grégoire, Hugues Chaté, and Olivier Dauchot, “Long-wavelength modulation of turbulent shear flows,” *Physica D: Nonlinear Phenomena*, 174(1-4):100–113, 2003.

[Prigent *et al.*, 2002] Arnaud Prigent, Guillaume Grégoire, Hugues Chaté, Olivier Dauchot, and Wim van Saarloos, “Large-scale finite-wavelength modulation within turbulent shear flows,” *Physical review letters*, 89(1):014501, 2002.

[Pringle *et al.*, 2008] Chris CT Pringle, Yohann Duguet, and Rich R Kerswell, “Highly symmetric travelling waves in pipe flow,” *Philosophical Transactions of the Royal*

Society A: Mathematical, Physical and Engineering Sciences, 367(1888):457–472, 2008.

[Reddy and Henningson, 1993] Satish C Reddy and Dan S Henningson, "Energy growth in viscous channel flows," *Journal of Fluid Mechanics*, 252:209–238, 1993.

[Reynolds, 1883a] Osborne Reynolds, "III. An experimental investigation of the circumstances which determine whether the motion of water shall be direct or sinuous, and of the law of resistance in parallel channels," *Proceedings of the royal society of London*, 35(224-226):84–99, 1883.

[Reynolds, 1883b] Osborne Reynolds, "XXIX. An experimental investigation of the circumstances which determine whether the motion of water shall be direct or sinuous, and of the law of resistance in parallel channels," *Philosophical Transactions of the Royal society of London*, (174):935–982, 1883.

[Ritter *et al.*, 2016] Paul Ritter, Fernando Mellibovsky, and Marc Avila, "Emergence of spatio-temporal dynamics from exact coherent solutions in pipe flow," *New Journal of Physics*, 18(8):083031, 2016.

[Ruelle and Takens, 1971] David Ruelle and Floris Takens, "On the nature of turbulence," *Communications in mathematical physics*, 20(3):167–192, 1971.

[Saad and Schultz, 1986] Youcef Saad and Martin H Schultz, "GMRES: A generalized minimal residual algorithm for solving nonsymmetric linear systems," *SIAM Journal on scientific and statistical computing*, 7(3):856–869, 1986.

[Sano and Tamai, 2016] Masaki Sano and Keiichi Tamai, "A universal transition to turbulence in channel flow," *Nature Physics*, 12(3):249, 2016.

[Schmid, 2007] Peter J Schmid, "Nonmodal stability theory," *Annu. Rev. Fluid Mech.*, 39:129–162, 2007.

[Schmid and Henningson, 2012] Peter J Schmid and Dan S Henningson, *Stability and transition in shear flows*, volume 142, Springer Science & Business Media, 2012.

[Schneider *et al.*, 2010a] Tobias M Schneider, Filippo De Lillo, Juergen Buehrle, Bruno Eckhardt, Tim Dörnemann, Kay Dörnemann, and Bernd Freisleben, "Transient turbulence in plane Couette flow," *Physical review E*, 81(1):015301, 2010.

[Schneider and Eckhardt, 2009] Tobias M Schneider and Bruno Eckhardt, "Edge states intermediate between laminar and turbulent dynamics in pipe flow," *Philosophical Transactions of the Royal Society of London A: Mathematical, Physical and Engineering Sciences*, 367(1888):577–587, 2009.

[Schneider *et al.*, 2008] Tobias M Schneider, John F Gibson, Maher Lagha, Filippo De Lillo, and Bruno Eckhardt, "Laminar-turbulent boundary in plane Couette flow," *Physical Review E*, 78(3):037301, 2008.

[Schneider *et al.*, 2010b] Tobias M Schneider, Daniel Marinc, and Bruno Eckhardt, "Localized edge states nucleate turbulence in extended plane Couette cells," *Journal of Fluid Mechanics*, 646:441–451, 2010.

[Sengupta and Poinsot, 2010] Tapan Sengupta and Thierry Poinsot, *Instabilities of flows: With and without heat transfer and chemical reaction*, volume 517, Springer Science & Business Media, 2010.

[Shi *et al.*, 2013] Liang Shi, Marc Avila, and Björn Hof, "Scale invariance at the onset of turbulence in Couette flow," *Physical review letters*, 110(20):204502, 2013.

[Shimizu and Manneville, 2018] Masaki Shimizu and Paul Manneville, "Bifurcations to turbulence in transitional channel flow," *arXiv preprint arXiv:1808.06479*, 2018.

[Skufca *et al.*, 2006] Joseph D Skufca, James A Yorke, and Bruno Eckhardt, "Edge of chaos in a parallel shear flow," *Physical review letters*, 96(17):174101, 2006.

[Sommerfeld, 1908] Arnold Sommerfeld, "Ein beitrag zur hydrodynamischen erklaerung der turbulenten fluessigkeitsbewegungen," *Atti del*, 4:116–124, 1908.

[Song, 2014] Baofang Song, "Direct numerical simulation of transition to turbulence and turbulence control in pipe flow," 2014.

[Stuart, 1960] JT Stuart, "On the non-linear mechanics of wave disturbances in stable and unstable parallel flows Part 1. The basic behaviour in plane Poiseuille flow," *Journal of Fluid Mechanics*, 9(3):353–370, 1960.

[Takens, 1981] Floris Takens, "Detecting strange attractors in turbulence," In *Dynamical systems and turbulence, Warwick 1980*, pages 366–381. Springer, 1981.

[Tao *et al.*, 2018] JJ Tao, Bruno Eckhardt, and XM Xiong, "Extended localized structures and the onset of turbulence in channel flow," *Physical Review Fluids*, 3(1):011902, 2018.

[Theiler, 1990] James Theiler, "Estimating fractal dimension," *JOSA A*, 7(6):1055–1073, 1990.

[Toh and Itano, 2003] Sadayoshi Toh and Tomoaki Itano, "A periodic-like solution in channel flow," *Journal of Fluid Mechanics*, 481:67–76, 2003.

[Trefethen *et al.*, 1993] Lloyd N Trefethen, Anne E Trefethen, Satish C Reddy, and Tobin A Driscoll, "Hydrodynamic stability without eigenvalues," *Science*, 261(5121):578–584, 1993.

[Tsukahara *et al.*, 2010] Takahiro Tsukahara, Yasuo Kawaguchi, Hiroshi Kawamura, Nils Tillmark, and P Henrik Alfredsson, "Turbulence stripe in transitional channel flow with/without system rotation," In *Seventh IUTAM Symposium on Laminar-Turbulent Transition*, pages 421–426. Springer, 2010.

[Tsukahara *et al.*, 2005] Takahiro Tsukahara, Yohji Seki, Hiroshi Kawamura, and Daisuke Tochio, "DNS of turbulent channel flow at very low Reynolds numbers," In *TSFP Digital Library Online*. Begel House Inc., 2005.

[Tuckerman *et al.*, 2014] Laurette S Tuckerman, Tobias Kreilos, Hecke Schrobsdorff, Tobias M Schneider, and John F Gibson, "Turbulent-laminar patterns in plane Poiseuille flow," *Physics of Fluids*, 26(11):114103, 2014.

[Viswanath, 2007] Divakar Viswanath, "Recurrent motions within plane Couette turbulence," *Journal of Fluid Mechanics*, 580:339–358, 2007.

[Waleffe, 1998] Fabian Waleffe, "Three-dimensional coherent states in plane shear flows," *Physical Review Letters*, 81(19):4140, 1998.

[Waleffe, 2001] Fabian Waleffe, "Exact coherent structures in channel flow," *Journal of Fluid Mechanics*, 435:93–102, 2001.

[Waleffe, 2003] Fabian Waleffe, "Homotopy of exact coherent structures in plane shear flows," *Physics of Fluids*, 15(6):1517–1534, 2003.

[Wall and Nagata, 2016] DP Wall and M Nagata, “Exact coherent states in channel flow,” *Journal of Fluid Mechanics*, 788:444–468, 2016.

[Wedin and Kerswell, 2004] Hakan Wedin and Rich R Kerswell, “Exact coherent structures in pipe flow: travelling wave solutions,” *Journal of Fluid Mechanics*, 508:333–371, 2004.

[Willis, 2017] Ashley P Willis, “The Openpipeflow Navier–Stokes Solver,” *SoftwareX*, 6:124–127, 2017.

[Willis and Kerswell, 2009] Ashley P Willis and Rich R Kerswell, “Turbulent dynamics of pipe flow captured in a reduced model: puff relaminarization and localized ‘edge’states,” *Journal of Fluid Mechanics*, 619:213–233, 2009.

[Wygnanski and Champagne, 1973] Israel J Wygnanski and FH Champagne, “On transition in a pipe. Part 1. The origin of puffs and slugs and the flow in a turbulent slug,” *Journal of Fluid Mechanics*, 59(2):281–335, 1973.

[Xiong *et al.*, 2015] Xiangming Xiong, Jianjun Tao, Shiyi Chen, and Luca Brandt, “Turbulent bands in plane-Poiseuille flow at moderate Reynolds numbers,” *Physics of Fluids*, 27(4):041702, 2015.

[Zammert and Eckhardt, 2014a] Stefan Zammert and Bruno Eckhardt, “Periodically bursting edge states in plane Poiseuille flow,” *Fluid Dynamics Research*, 46(4):041419, 2014.

[Zammert and Eckhardt, 2014b] Stefan Zammert and Bruno Eckhardt, “Streamwise and doubly-localised periodic orbits in plane Poiseuille flow,” *Journal of Fluid Mechanics*, 761:348–359, 2014.

[Zammert and Eckhardt, 2015] Stefan Zammert and Bruno Eckhardt, “Crisis bifurcations in plane Poiseuille flow,” *Physical Review E*, 91(4):041003, 2015.